Università degli Studi della Tuscia di Viterbo

Dipartimento di Economia, Ingegneria, Società e Impresa

Ph.D. Program
Engineering for Energy and Environment – XXXIV Cycle

MULTIPHYSICS APPROACH FOR THE EVALUATION OF ELECTROMAGNETIC BEHAVIOUR OF TOKAMAK 3D STRUCTURES DURING PLASMA DISRUPTIONS AND APPLICATION TO EU DEMO, DTT AND ST40 PROJECTS

S.S.D. ING-IND/31

Ph.D. Candidate:
Dott. Lombroni Riccardo

Ph.D. Coordinator
Prof. Ing. Andrea Luigi Facci

Supervisor
Prof. Ing. Giuseppe Calabrò

Co-supervisor
Prof. Ing. Pierluigi Fanelli

A.Y. 2021/22

A Lavinia,

ingiustamente strappata da questo mondo,

sarai sempre qui,

ad accompagnare il nostro viaggio,

in tutti i traguardi come questo

Abstract

Ever since its conception in the 1950s, the tokamak has arguably been considered the most promising approach to harness the energy of fusion in a controlled way. In tokamaks, the thermal and electro-magnetic loads emerging during so-called normal and off-normal operations represent important input for the structural assessment of the components. In particular, among all these events, the so-called plasma disruptions are one of the major concerns. A plasma disruption is a complex phenomenon involving plasma instabilities which results in a abruptly termination of the plasma and the complete transfer of the plasma thermal and magnetic energy to the surrounding structures on very short timescales. The uncontrolled release of this energy has the potential to inflict severe damages to components, especially in the future reactor-scale tokamaks, such as ITER and DEMO, where the energy stored during a burning plasma pulse will significantly exceed that in present devices. Modern tokamaks, even the largest operating devices such as JET and JT-60U, have generally been able to manage the consequences of disruptions with only limited impact on operational schedules. This is also the case of ST40 and the DTT project, in which a certain disruptions rate is expected and tolerated without compromise their overall scientific mission. Anyway, disruptions have the capability to cause considerable damages also in these devices. Therefore, even if disruptions implications differ between ITER, DEMO and present tokamaks in terms of intensity of the loads, prevention and mitigation requirements, systems and strategies, the evaluation of the related effects always represent one of the main driver of the design of their components, to ensure they reach the projected lifetime and fulfil their function even in the worst scenario. In this context, reliable modelling tools able to predict these loads in details are strongly desired.

This Thesis deals with the EM aspects of plasma disruptions. The evaluation of the EM loads in tokamak reactors is not straightforward and must cope with different problems, such as the implementation of all sources of magnetic field (in particular the plasma during its evolution) and the identification of conductive structures that contribute to the behaviour of the induced currents inside the region of interest. In this Thesis, a novel multiphysics and multicode approach aimed at 3D detailed evaluation of the electro-magnetic loads experienced by the tokamak structures both in normal and off-normal conditions is proposed. Based on the use of MAXFEA code in combination with ANSYS, this new engineering tool was developed and successfully applied in the context of DEMO, DTT and ST40. In particular, the EM response of the main components of these devices, such as the Vacuum Vessel (VV) and the In-Vessel Components (IVCs), were investigated during plasma disruptions. The methodology proposed in this Thesis demonstrated to be a reliable tool to support the design of such components both in conceptual (DEMO) and in detailed phase of the design (DTT, ST40), proving at the same time to have a wide range of applications: from present experimental devices to DEMO, from conventional to non-conventional aspect ratio tokamaks, from standard to advanced plasma configurations.

Index

1 Introduction

Throughout human history, the sun has always inspired the humans, believing it to have divine powers, the ability to overcome darkness forces and provide prosperity and wealth to mankind. Ra for the ancient Egyptians, Elio and Apollo for the Greeks, Sol for the Romans, Huitzilopochtli for the Aztecs, the sun has always been worshiped as a God, venerated as source of light and life. And in ultimate this is what the sun is: the source of energy which makes it possible for life to exist on Earth. What an amazing finale would it be for our species if we could harness the power of the sun, if we could have access to the power of the Gods?

The energy demand has been increasing constantly in the last decades due to the industrial activity and advanced in both developing and developed countries and a further acceleration in this growth is expected in the next decades under the combined pressure of population growth, increased urbanization and expanding access to electricity in developing countries. Nowadays, approximately 70% of it is covered by fossil fuels, which produce CO_2 and other so-called "greenhouse gases" contributing to the alarming global climate change and, in particular, the world energy consumption is expected to increase by 38% by 2050 [1]. Therefore, one of the greatest challenges of our time consists in finding novel, clean and sustainable energy sources both environmental-friendly and able to sustain the energy demand growth. Among others, nuclear fusion would represent a promising option to tackle the global energy challenge.

Inside the stars, fusion reactions take place at high temperatures under the huge gravitational pressure. Since it is not obviously possible to reproduce the same conditions on Earth, in a reactor the fuel, in plasma state, needs to be confined and heated to extremely high temperatures, roughly twenty times more than in the sun core. The more convenient way to achieve nuclear fusion in laboratory is to use the reaction between two hydrogen isotopes: deuterium and tritium. When deuterium and tritium nuclei fuse, the process liberates a huge amount of energy, available as kinetic energy carried by the reaction products: helium α-particles (3.52 MeV) and fast neutrons (14.06 MeV). Fusing deuterium and tritium together releases nearly 4 million times more energy than a chemical reaction (the typical molecular bound energy is in the order of $1 \div 10$eV) such as the burning of coal, oil or gas and 4 times as much as nuclear fission reactions (at equal mass), without emitting any greenhouse gases into the atmosphere, being the helium the major reaction product (inert and no-toxic) [2]. Furthermore, fusion has advantages that ensure sustainability and security of supply: fuels are widely available and virtually unlimited; intrinsically safe, as no chain-reaction can occur; environmentally responsible, since reactors would produce no high activity long-lived nuclear waste. Ever since the process that powers the stars was harnessed in the 1950s for hydrogen bombs, generations of scientists have dreamt of unlocking it in a controlled way for peaceful applications like energy production, exploring different approaches and concepts. Among others, the most common and advanced approach consists in confining the plasma by means of magnetic field cage in devices called tokamaks [3]. Still, the realization of fusion has to face a number of astonishingly ambitious scientific and technological challenges.

In 2012, the European Fusion Development Agreement (EFDA), now evolved into the EUROfusion organization [4], created an ambitious plan providing fusion electricity to the grid by the middle of the 21st century, via a comprehensive integrated science, technology and engineering programme: Fusion Electricity –

A roadmap to the realisation of fusion energy [5]. Since its conception, the Fusion Roadmap has been a fundamental reference to guide the European fusion community in the establishment of the priorities in fusion research towards the ultimate goal of achieving electricity from Fusion energy. The strategy of the roadmap is built on three main pillars: the international ITER tokamak that will demonstrate the scientific and technological feasibility of fusion as an energy source, a fusion neutron source facility for material development and qualification, and a demonstration power plant (DEMO), which will deliver hundreds of megawatts of electricity to the grid and operate with a closed fuel-cycle [6]. The roadmap addresses three separate periods with distinct main objectives. The first period (< 2030) foresees the start of the ITER operation and the completion of the DEMO conceptual design(s). In the second period (2030-2040), the exploitation of ITER up to its maximum performance is expected in parallel with DEMO engineering design. Finally, the third period (> 2040) will be the phase of the ITER plasma and technology optimisation and of the DEMO construction. ITER project is the key facility of the roadmap and reflects the scale of the enterprise: currently under construction in southern France, ITER is the world's biggest fusion reactor born from the collaboration of 35 nations, including China, European Union member states, the United States, Russia, South Korea and Japan, with a price tag of at least $22 billion. ITER is expected to achieve most of the important milestones needed on the path to fusion energy demonstrating that a burning plasma can be created and sustained, generating hundreds of megawatts of fusion power. The project is ultimately aimed at the development of the scientific know-how for the plasma and some of the technology [6]. In the European strategy, DEMO is the machine that should bridge the gap between ITER and the first commercial fusion power plant, taking fusion to the next level: a fully-integrated science and technology demonstration of fusion energy production. DEMO design/R&D activity is expected to benefit largely from the experience gained with the design, construction and operation of ITER. Nevertheless, since DEMO will operate in different plasma parameters regime than ITER, extrapolation is not always straightforward and there are outstanding physics, material and engineering challenges that must be resolved in view of DEMO. At the present, DEMO is in a pre-conceptual design phase and a number of studies that have strong implications on machine parameters and architectural layout have been initiated [7]. In [8], the progress in the DEMO pre-conceptual design activities carried out by the EUROfusion Consortium is exposed.

Among all the different physics and technological areas where DEMO requires significant progress compared to ITER [9], the management of the energy extracted from plasma is one of the major concerns. In ITER, a specific activity is in progress to optimize a conventional divertor based on detached conditions [10]. However, since it is conceivable that the baseline strategy can not be extrapolated to DEMO and commercial fusion power plants, the possibility to design a dedicated Divertor Tokamak Test facility (DTT) has been proposed within the EUROfusion road map. Aim of DTT is to access a set of possible alternative solutions for DEMO, including the test of advanced magnetic configurations and liquid metal divertors. In 2015, a team of international experts demonstrated the possibility to realize a flexible and effective facility able to bridge the power exhausts gaps between ITER and DEMO (The DTT proposal [11]). Since then, the DTT project has moved on. Presently, the conceptual design phase approaches its conclusion (DTT Interim Design Report [12]) and the engineering phase has started. Different overview paper have been published in the last few years to describe the status of the DTT project [13]–[15], with the more recent update given in [16]. Nowadays, the project is managed by a DTT legal entity mainly composed by ENEA and ENI and with the participation of important Italian research centres and universities, including Tuscia University [17].

Nuclear fusion has historically been the preserve of publicly funded national and international projects. Although the largest slice of fusion research is still connected with public organization, with ITER being so far the biggest international effort in Fusion research, since the last decade private-sector investments has emerged showing a rapid expansion and growth. Increasing numbers of private companies are aiming to deliver commercial fusion and producing significant breakthroughs in the science and technology that will lead to a commercial power plant. According to a recent survey by the Fusion Industry Association (FIA), there are now more than 30 private fusion firms globally [18]. The 18 firms that have declared their funding claim that they have attracted more than $2.4 billion in total, almost entirely from private investments. There is currently a global race to commercialise fusion. Key to these efforts are advances in material research and computing that are opening new routes that differ from the mainstream ITER-DEMO path of using larger and larger big size tokamaks and could potentially speed up the process. Whitin this framework, Tokamak Energy, founded in 2009, is one of the leading private fusion energy companies. Located in Oxfordshire, UK, the company is developing compact fusion power plants based on two promising technologies: Spherical Tokamaks (STs) and High Temperature Superconductors (HTS) [19]–[21]. The ST route to fusion has generated considerable interest since the mid-1980s [22]–[24]. This concept demonstrates all the main feature of conventional tokamaks having at the same time the real potential to significatively reduce costs and timescales on the path to fusion power. In the past, the first attempts to design ST based devices did not produce convincing design and until recently STs have remained on the margins of fusion research. However, recent advances in both tokamak physics and superconductor technology have a made a ST fusion reactor a possibility. The key technological advance is the advent of rare-earth HTS. The mission of Tokamak Energy is to exploit the combination of the efficiency of STs and the benefits of the HTS with the aim to build a lower-volume fusion power plant by the 2030's (a factor of 30 smaller than ITER in volume). On its path to Fusion Power, Tokamak Energy is presently operating ST40 [25]-[26], a new generation ST that is currently the highest field device of its kind.

In this Thesis, a novel engineering tool aimed at evaluation of the Electro-Magnetic (EM) loads experienced by the tokamak structures both in normal and off-normal conditions has been developed and successfully applied in the context of DEMO, DTT and ST40 projects. In particular, the EM response of the main components of these devices, such as the Vacuum Vessel (VV) and the In-Vessel Components (IVCs), has been investigated during the so-called plasma disruptions.

A plasma disruption is a complex phenomenon involving plasma instabilities which results in a abruptly termination of the plasma and the complete transfer of the plasma thermal and magnetic energy to the surrounding structures on very short timescales, with the potential to inflict severe damages to components. In ITER, the energy stored during a burning plasma pulse will significantly exceed that in present devices. The rapid release of this energy during a disruption has the potential to cause surface melting of the Plasma Facing Components (PFCs) and produce high EM loads close to the design limits. The successful exploitation of ITER will overwhelmingly depend on the development and implementation of effective disruption prevention and mitigation strategies [27]. Despite the disruption handling requirements are very stringent in ITER, the challenge is even bigger in DEMO. Unlike research devices, an economically viable fusion reactor must provide high reliability and availability, and long service lifetime (several decades) in order to recoup the initial investment [28]. Therefore, any unexpected termination must be avoided and mitigation strategies must be considered as last resort to reduce damaging concentration of thermal and mechanical loads. Not surprisingly, in [9] the disruptions are individuated as one of the main areas in which a significant progress is required in view of DEMO. According with the roadmap, most of the advance in this area will be accomplished by the end of the first period (< 2030). The strategy proposed is based on a coordinated multi-machine experimental effort, involving JET, the Medium-Size Tokamaks (MSTs) and JT-60SA, complemented by theory and model validation for extrapolation towards ITER and DEMO.

Disruptions have the capability to cause considerable damages also in present generation devices, such as DTT and ST40. However, the disruption handling requirements are not so stringent for these projects and, in fact, a certain disruption rate is expected during the normal operation. Being DTT and ST40 pulsed experimental devices, even though the disruptions require careful attention, their presence does not compromise the overall scientific mission of these projects.

Anyway, although the disruptions implications differ between ITER, DEMO and present tokamaks in terms of prevention and mitigation requirements, systems and strategies, the related EM and thermal loads always represent one of the main driver of the design of the VV and the IVCs, to ensure they reach the projected lifetime and fulfil their function even in the worst unlike scenario. In this context, reliable modelling tools able to predict these loads in details are strongly desired.

This Thesis deals with the EM aspects of the plasma disruptions. A novel procedure based on the use of the MAXFEA code in combination with ANSYS APDL for a detailed 3D evaluation of the EM loads coming from different EM transients, such as plasma disruptions, has been developed. Then, this procedure has been successfully applied in DEMO, DTT and ST40 projects, showing its reliability as design supporting tool in wide different contexts and in both conceptual (DEMO) and detailed phase of the design (DTT, ST40).

The main outcomes of these studies were presented at international conferences. Among all:

- 31st Symposium on Fusion Technology (SOFT2020):
  R. Lombroni, et al., *Preliminary 3D EM loads on DEMO SN configuration calculated by MAXFEA coupled to ANSYS EMAG code*
- 31st Symposium on Fusion Technology (SOFT2020):
  F. Maviglia, et al., *Integrated strategy of limiter design for EU-DEMO first wall protection from plasma transients*
- 31st Symposium on Fusion Technology (SOFT2020):
  E. Martelli, et al., *Design status of the Vacuum Vessel of DTT facility*

- 47th EPS Conference of Plasma Physics in collaboration with ST40 Team, Princeton University, Oxford University, Consorzio RFX:

  M. Romanelli, et al., *Preparing for First Diverted Plasma Operation in the ST40 High-Field Spherical Tokamak*
- 63rd Annual Meeting of the APS Division of Plasma Physics in collaboration with ST40 Team, Princeton University, Oxford University:

  M. Romanelli, et al., *Integrated Modelling of Plasmas in the ST40 High-Field Spherical Tokamak*

Moreover, these studies led to the following journal publications:

- **R. Lombroni**, F. Giorgetti, G. Calabrò, P. Fanelli, and G. Ramogida, "Using MAXFEA code in combination with ANSYS APDL for the simulation of plasma disruption events on EU DEMO," *Fusion Eng. Des.*, vol. 170, no. May, p. 112697, Sep. 2021.
- F. Maviglia *et al.*, "Integrated design strategy for EU-DEMO first wall protection from plasma transients," *Fusion Eng. Des.*, vol. 177, no. February, p. 113067, Apr. 2022.
- E. Martelli, G. Barone, F. Giorgetti, **R. Lombroni**, G. Ramogida, and S. Roccella, "Design status of the Vacuum Vessel of DTT facility," *Fusion Eng. Des.*, vol. 172, no. November 2020, p. 112760, 2021
- V. G. Belardi, G Calabrò, P Fanelli, F Giorgetti, **R. Lombroni**, G Ramogida, S Trupiano and F Vivio, "Preliminary design and structural assessment of DTT in-vessel coil supports," *IOP Conf. Ser. Mater. Sci. Eng.*, vol. 1038, no. 1, p. 012075, 2021
- Contributor of: R. Albanese, F. Crisanti, P. Martin, R. Martone, and A. Pizzuto, "DTT - Divertor Tokamak Test Facility – Interim Design Report." 2019
- B. J. Xiao, *et al.*, "Progress on in-vessel poloidal field coils optimization design for alternative divertor configuration studies on the EAST tokamak," *Fusion Eng. Des.*, vol. 146, no. March, pp. 2149–2152, Sep. 2019
- P. Agostinetti *et al.*, "Improved Conceptual Design of the Beamline for the DTT Neutral Beam Injector," *IEEE Trans. Plasma Sci.*, pp. 1–6, 2022.

Some of which are in the final stage of review process or in press:

- **R. Lombroni**, et al., "Use of MAXFEA code in combination with ANSYS APDL to study the Electro-Magnetic behaviour of the new ST40 Inner Vacuum Chamber (IVC2) proposal during a plasma VDE," submitted to *Fusion Eng. Des.*
- F. Giorgetti, et al., "Vertical Displacement Events analysis using MAXFEA code in combination with ANSYS APDL in the final design stage of the DTT Vacuum Vessel," submitted to *Fusion Eng. Des.*
- G. Sias *et al.*, "Inter-machine plasma perturbation studies in EU-DEMO relevant scenarios: lessons learnt for EM forces prediction during VDEs," *Nucl. Fusion*, Feb. 2022 accepted manuscript.

This Thesis is articulated as follow. Section 2, provides an overview of the Disruptions. In Section 3 the developed methodology is exposed. Section 4-6 will present the application of this methodology in the context of DEMO, DTT and ST40 projects, respectively. Finally, conclusions and main outlooks are summarized in Section 7.

2 Disruptions

Plasma disruptions are one of the major concerns in the design phase of fusion devices. The uncontrolled release of plasma EM and thermal energy in very short timescales has the potential to inflict severe damages on the components, especially in reactor-scale tokamaks, such as ITER and DEMO, where the energy stored during a burning plasma pulse will significantly exceed that in present devices [29][30]. Modern tokamaks, even the largest operating devices such as JET and JT-60U, have generally been able to manage the consequences of disruptions with only limited impact on operational schedules. This is also the case of ST40 and DTT, in which a certain disruptions rate is expected and tolerated without compromising their overall scientific mission. Anyway, disruptions have the capability to cause considerable damage also in these devices. Therefore, even if disruptions implications differ between ITER, DEMO and present tokamaks in terms of intensity of the loads, prevention and mitigation requirements, systems and strategies, the evaluation of the related effects always represent one of the main driver of the design of their components, to ensure they reach the projected lifetime and fulfil their function even in the worst scenario.

Plasma disruptions typically proceed in two steps. Firstly, a sudden loss of the plasma confinement occurs determining the generation of high thermal loads on the PFCs. This phase is called Thermal Quench (TQ) phase. During the TQ, the plasma is cooled to sub-keV temperatures in very short time scale and a global contamination of the plasma ensues as consequence of Plasma-Wall Interaction (PWI). Then, as the result of the combination of these factors, the plasma resistivity dramatically increases producing a rapid decay of the plasma current, known as Current Quench (CQ) phase. During this phase, the sudden drop of the plasma current generates high induced currents in the nearby conducting structures and, consequently, huge EM forces on the components. In JET a plasma current of several megaamperes typically decades on a time scale of ~5-50ms, resulting in forces of several MN on the tokamak VV [31]. According to [32], in ITER a maximum vertical force of about 80-85 MN is expected during a Vertical Displacement Event (VDE).

Through the years, disruption physics has been the subject of intense investigations aimed to deepen the knowledge of the causes and consequences of these events. Several precursors, in many case related to operations close to the ‘operational limits’ [30], have been individuated. Magneto-hydrodynamic (MHD) instabilities are typically observed to determine the onset of a disruption. Often the events that lead to a disruption are a complex combination of several destabilizing precursors. Therefore, it is not always easy to determine a clear cause or to classify disruption types [31]. Furthermore, even if disruptions can be related to plasma stability physics, it is not rare that technical problems are found to be the main cause. Premature turn-off of the Ohmic drive power supply, excessive gas fuelling input rates, poor wall conditions, release of impurities into the plasma, plasma control failure, human errors in pulse programming are only few of the possible causes that have been identified through the years. Because of the complexity of the physics that underlies disruptions and its causes, disruptions are not easy to predict, and huge efforts are presently made in developing strategies for their control and mitigation in view of ITER [27], whose successful exploitation will strongly depend on the effectiveness of these systems. Despite these research efforts, the understanding of disruption physics is still ongoing and many open issues remain. In [33], a survey of the basic physical phenomena underlying plasma disruptions was given with the aim to guide the establishment of future research plan for the development of appropriate theoretical methods for simulating, avoiding and mitigating disruptions.

Understanding both how the effects of disruptions and the effectiveness of their mitigation will scale from present devices to a burning plasma device (e.g. ITER and DEMO) will be critical for their design. Unfortunately, the present physics understanding of the disruption make integrated and comprehensive quantitative numerical predictions of these phenomena difficult. The combination of rapid time scales, highly nonlinear processes, intense PWI, large-scale impurity transport, MHD instability, etc. seems to make disruptions phenomenology presently too complex to be fully understood. However, comprehensive empirical knowledge of disruptions can provide the information on engineering limits when exhaustive theoretical understanding is incomplete. Since 1994, within the International Tokamak Physics Activity (ITPA) MHD, Disruptions and Control Topical Group [34], a strong effort has been made to establish a multi-machine database, the ITER disruption database (IDDB), that can be used for characterization of disruptions and disruption related effects [29][30][35]. Such empirical database of disruption parameters provide empirical scalings where no viable model exists and support the modelling efforts. Contributing devices include the conventional aspect ratio tokamaks ADITYA [36], Alcator C-Mod [37], ASDEX Upgrade [38], DIII-D [39], JET [40], JT-60U [41] and TCV [42] as well as the spherical tokamaks MAST [43] and NSTX [44].

Even though fully integrated numerical models are presently lacking, individual aspects of the disruptions have been modelled through the years. Since these simulations often require significant assumptions regarding the plasma state during the disruption, the importance of the ITPA IDDB lies in providing robust assumptions based on empirical observations. This happens when one is investigating the EM effects of plasma disruptions. In these kind of simulations, parameters such as the total duration of the TQ and CQ phase or the evolution of the plasma internal parameters are fundamental assumption for the plasma evolution and, therefore, the evaluation of the EM loads induced in the components.

This Section aimed to present the characteristics of the disruptions. Section 2.1 introduces the plasma vertical instability and the disruption scenarios, while Section 2.2 focuses on the halo current. TQ and CQ phases and their EM implications, especially under the modelling point of view, are presented in Sections 2.3-2.4.

2.1 Vertical Instability and disruption scenarios

Plasma vertical stability plays an important role in the phenomenology of a disruption. Since elongated plasmas are naturally vertically unstable, a sufficiently large and fast change in plasma parameters (e.g. Ip, β_p, li, etc.)[1] can cause a loss of vertical position control, leading to an uncontrolled upward or downward displacement of the plasma column that could eventually come in contact with the IVCs. A vertical plasma displacement can trigger, ultimately, the onset of a disruption or can even be induced by a disruption itself. According to [30], plasma disruptions are usually classified depending on the position of the plasma column at the TQ, as Major Disruptions (MDs) and Vertical Displacement Events (VDEs).

[1] Plasma parameters β_p and li will be presented in detail in Section 3

In MDs the disruption process begins with the TQ that occurs when the plasma is close to its central position. During the TQ most of the plasma thermal energy is rapidly lost through radiation and/or conduction to the divertor. The fast changes in the plasma parameters which accompany the TQ, often lead to a loss of vertical position control. During the subsequent CQ phase, the plasma current usually decays on a slower time-scale than that of the vertical motion. Therefore, the plasma magnetic energy is often not dissipated until the plasma comes in contact with the IVCs, terminating at the top or the bottom of the chamber depending on the initial direction of the vertical displacement. MDs are often referred to as ‘central disruption’ and/or ‘cold VDEs’.
Instead, VDEs begin with a loss of position control that develops before any appreciable cooling of the plasma core. Faults in the vertical position feedback control system (e.g. power supply failures, sensor failures, power supply voltage/current limitations, etc.), running plasmas with excessive elongations and plasma perturbations are among the possible causes of the development of such instability. In particular, the occurrence of undesired plasma perturbations such as Edge Localized Modes (ELMs), unforeseen H-L and L-H transitions, minor disruptions (mDs), etc., is strongly connected to variations of plasma internal parameters and, consequently, to plasma displacements. During a VDE, in an initial phase, the plasma moves vertically away from its equilibrium position and starts to induce current in the passive structure mainly by its movement. In this phase, the plasma moves towards the wall, reducing progressively its area, typically with a little change in the total plasma current, since the plasma thermal energy is still present. Then, when the plasma starts to significatively interact with the structures or when plasma reaches a critical value of the safety factor, conditions for a rapid growth of MHD activity inevitably arise and the TQ occurs. As a consequence of the TQ, the ensuing increase in plasma resistivity produces the CQ phase. These kind of events are also known as ‘hot VDE’.
If not otherwise stated, in the remainder of this Thesis the meaning of ‘MD’ and ‘VDE’ refers to this classification.

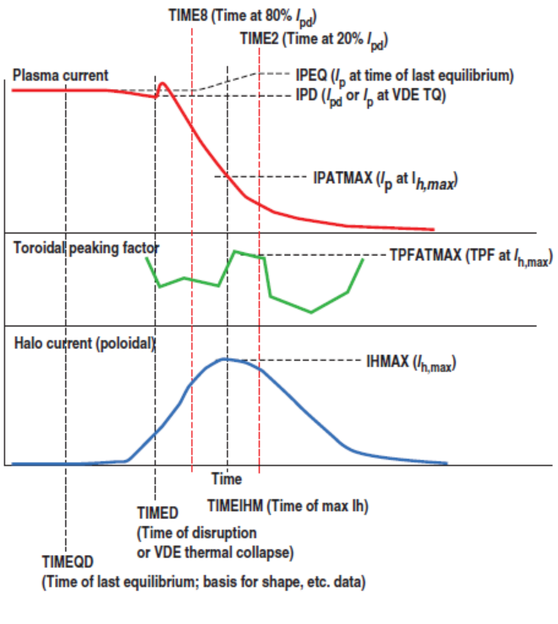

Figure 2.1: Illustration of key times within description of pre-disruptive plasma, CQ and halo current evolution. Reprinted from [35]

2.2 Halo current

During 'cold VDEs' and 'hot VDEs', the decay of the plasma current in the CQ phase together with the progressive plasma cross-section shrinking generate an electric field that drive helical current flow in the so-called 'ex-plasma halo region', that lies beyond the Last Closed Flux Surface (LCFS). As this ex-plasma halo region is in contact with the PFCs, this so-called halo current reconnect through the structures, since the resistivity of the ex-plasma halo region is of the same magnitude of the metal walls. The resulting currents in the IVCs flow mostly in poloidal direction and interact with the Toroidal Field generating intense forces on the structures. Together with eddy currents induced as consequence of the plasma Poloidal Field Variation (PFV) and Toroidal Field Variation (TFV), especially during TQ and CQ phases, halo currents represent the main EM load experienced by the components during disruptions.

In the remainder of this paragraph, a survey of the ITPA IDDB study on the halo phenomenology is presented with reference to [29][30][35]. Two important parameters used in the IDDB are:

- Halo fraction f_H:
  With reference to Figure 2.1, f_H is the ratio of the maximum axisymmetric halo current $I_{h,max}$ to the pre-disruption plasma current I_{p0}:

$$f_H = \frac{I_{h,max}}{I_{p0}} \tag{2.1}$$

- Toroidal Peaking Factor TPF:
  Halo current often exhibits a non-axisymmetric distribution. This behaviour is captured in the TPF, which is recorded at the time of maximum halo current $I_{h,max}$

The measurements of I_h and TPF are dependent upon both the structure of the halo current and the toroidal resolution of the halo current sensors in a given device and their ability to resolve the possible halo current asymmetries. For a system of N toroidally distributed poloidal halo current sensors, each measuring a poloidal current density $j_{halo,n}$ (A/rad), the standard definitions of I_h and TPF are:

$$I_h = 2\pi \frac{\sum_1^N j_{halo,n}}{N} \tag{2.2}$$

$$TPF = \frac{max\left(j_{halo,n}\right)}{I_h/2\pi} \tag{2.3}$$

Where the maximum function represents the largest poloidal halo current density measured at a discrete toroidal location. Clearly, equations (2.2) and (2.3) are accurate as long as the spatial resolution of the halo current sensors is sufficient to avoid aliasing the actual halo current structure and resolve its phase [35].

In Figure 2.2, TPF is plotted versus f_H showing that the higher peaking factors tend to be seen only at lower normalized halo currents. A hyperbolic relationship can be used to define a bounding curve, which can be used for engineering design guidance. In particular, the bounding maximum value is $f_H \cdot$ TPF = 0.75. This bounding value ignores two outlier points from Alcator C-Mod (dashed circle in Figure 2.2), that were found to occur late during an Ip and B_T ramp-down, inflating the halo current and for that reason not included. In addition, there are also two JET point that exceed the limit value considered in ITER of $f_H < 0.52$ (black circle). This new bound may have important engineering implications in ITER, since the maximum f_H is a critical design point in determining the operational limits. However, upon closer examination, both of these point were found to be measured by only a single sensor and, thus, they are likely connected to a possible aliasing.

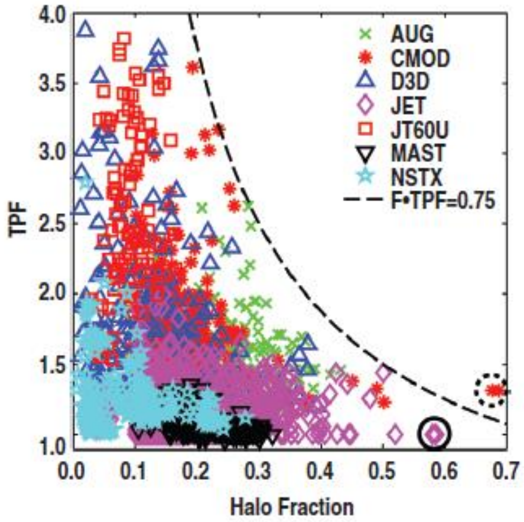

Figure 2.2: Toroidal peaking factor versus halo fraction (f_H), separated by device. The dashed line indicates constant f_H · TPF = 0.75 boundary. The two cases exceeding f_H · TPF > 0.75 (dashed circle) occurred late in an Ip and BT rampdown. The solid circled points represent an extension of the halo fraction boundary rom previous data. Reprinted from [35].

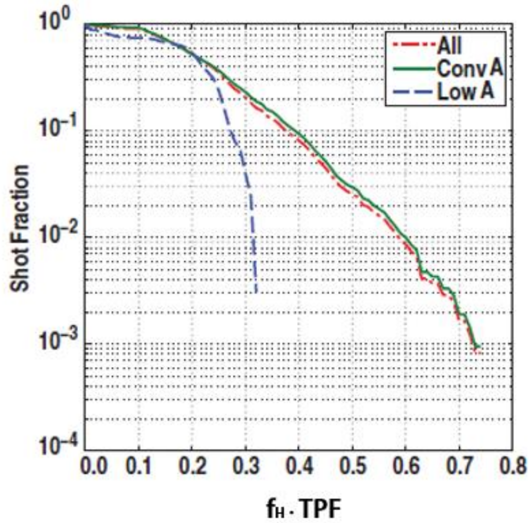

Figure 2.3: Cumulative probability of f_H · TPF exceeding a given value. Shot populations are divided into all, low-A (MAST and NSTX), and conventional-A devices. Reprinted from [35].

In terms of cumulative probability of f_H · TPF exceeding a given value, it was found that the population of discharges falls off rapidly as f_H · TPF increase, as shown in Figure 2.3. Globally, only ~ 1% of the events exceeds f_H · TPF = 0.6 and it is also worth to say that the IDDB distribution is almost certainly an overestimate of the actual unfiltered distributions, since each participants established a minimum threshold for halo current when choosing the events to submit to the database.

A characteristic behaviour emerging from the database is that f_H · TPF decreases with an increasing value of the pre-disruptive edge safety factor (q_{95}) as shown in Figure 2.4. Indeed, this result is consistent with the axisymmetric halo model presented in [45], in which it is stated that the poloidal halo current is strongly dependent upon the edge safety factor, with higher safety factor producing a smaller fraction of poloidal halo current.

Moreover, previous study in JET [46] seemed to highlight that f_H · TPF decreases with increasing current decay rate. Instead, this trend does not appear to be well supported within IDDB, as shown in Figure 2.5. In fact, JET shows a non-monotonic behaviour, peaking at around 50s^{-1} and falling off to either sides, NSTX exhibits a monotonic increase in f_H · TPF with the current decay, MAST maintains fairly consistent values over a wide range, while the other devices seems to not show any identifiable structure. Anyway, a significant hidden variable could be the vertical growth rate of the plasmas, which is not recorded in IDDB, as f_H is strongly determined by the ratio of the current decay to the vertical displacement growth rate [45]. In fact, in JET [46] the largest halo current fractions are found for the most vertically unstable configurations (i.e. low ratio of resistive vessel time to vertical displacement growth time).

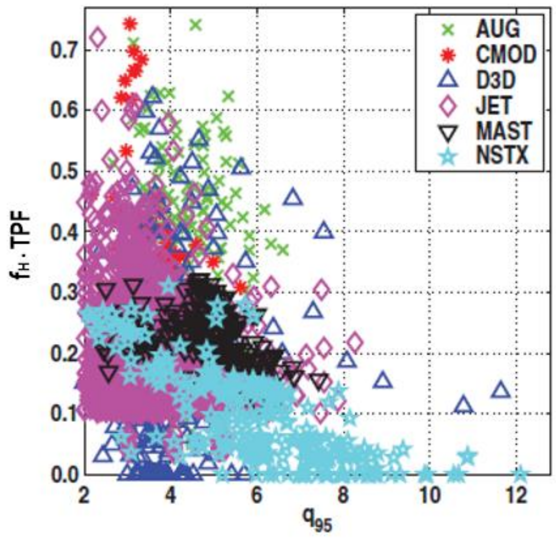

Figure 2.4: TPF versus q95 (f_H), separated by device. Reprinted from [35]

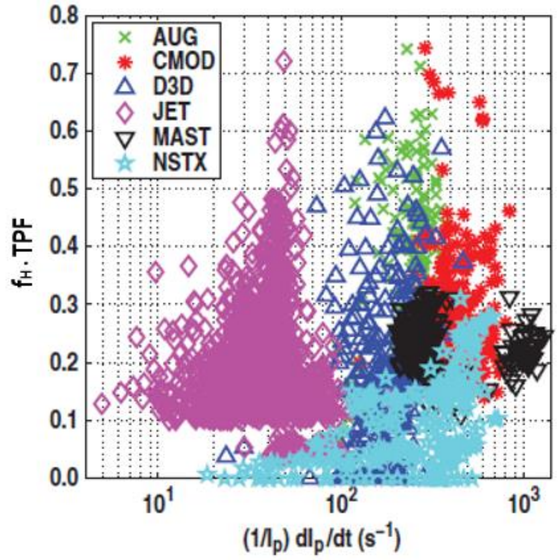

Figure 2.5: TPF versus normalized current decay rate. Reprinted from [35]

Previous studies in NSTX [47] and JT-60U [48] suggested a reduction in halo fraction as the plasma pre-disruptive thermal energy W_{th} increases. This behaviour is attributed to an increase in impurity density due to increased conducted heat flux to the divertor, which in turn cools the halo region making it more resistive and, therefore, reducing total halo current. However, this conjecture is not globally supported by the IDDB data. In fact, although NSTX exhibits this behaviour, and also DIII-D albeit in a weaker manner (JT-60U W_{th} is not available in IDDB), the trend is not consistent in other devices, as shown in Figure 2.6. There could be several factors concurring at this discrepancy. Among others, the material of the PFCs, in particular the divertor, could play an important role. In fact, DIII-D and NSTX are both all-carbon devices. In contrast, Alcator C-Mod (molybdenum) and ASDEX-Upgrade (tungsten) show no noticeable trend. This may indicate a much higher heat flux threshold for the high-Z metal wall material to pollute and cool the halo region as compared to carbon, making W_{th} unimportant for determining the halo fraction until that threshold might be reached [35]. However, the carbon wall data from MAST and JET also fail to exhibit this trend, suggesting that other factors could play a role. For example, the distribution of the heat flux during a VDE, which is function of the plasma and device geometry, could explain the different trend between the two STs, as NSTX has a simple open divertors, whereas MAST possesses a more complex structure that provides multiple points of contact.

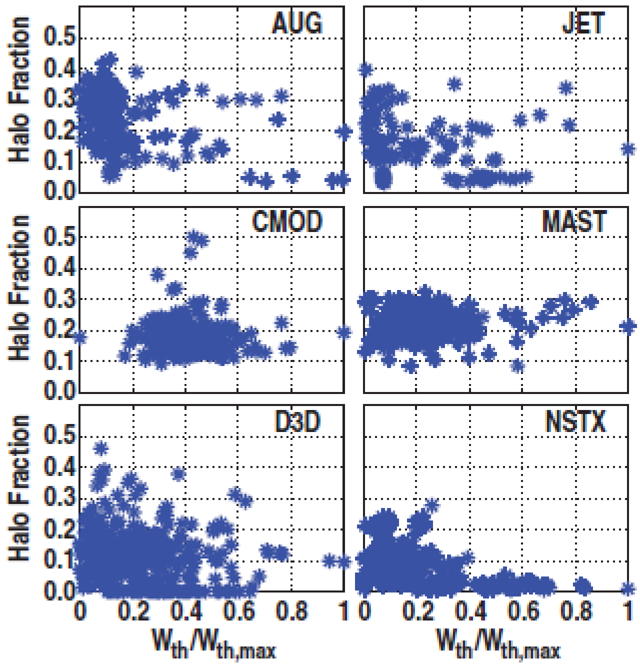

Figure 2.6: Comparison of Halo Fraction (f_H) versus $W_{th}/W_{th,max}$, organized by device. $W_{th,max}$ is the maximum W_{th} reported by each device for the halo current data plotted. Reprinted from [35]

2.3 TQ characteristics

The TQ is the phase of a disruption in which most of the plasma thermal energy is lost by the plasma and subsequently deposited on the IVCs, especially on the divertor surfaces, by conduction, convection and radiation. Its duration depends on the machine size and it is of the order of tens of microseconds in small tokamaks and hundreds of microseconds in medium-sized tokamaks. However, the duration is observed to vary significantly within a given machine (in JET TQs of few ms have been observed), apparently depending on the 'type' of disruption and/or the nature and growth rate of the triggering MHD instability [30].

The PFCs energy deposition phase of the TQ is typically preceded by one or more energy redistribution phases inside the plasma, with known cases showing one, two, three or more sequential redistributions. In [29], the phenomenology of a typical two-staged TQ is described. In the first phase, the thermal energy is redistributed within the plasma inside the $q = 2$ surface, causing the flattening of the temperature profile, with the $q = 2$ surface acting as a sort of thermal barrier, although a fraction of ~10-30% of the total thermal energy could be spilled out to the wall. In second stage, after a delay of $\tau_{1\text{-}2}$, the energy barrier breaks down completely and the energy is rapidly lost to the open flux surface region within a time τ_2. However, sometimes the second stage exhibits further staging of energy loss, resulting in a multi-step thermal energy decay form, while in other cases the two stage can effectively merge and during the initial redistribution of thermal energy there can be significant power outflux from the confined plasma [30].

In the time interval τ_2, the energy starts being lost to the divertor. The time τ_2 represents a lower bound for the PFCs deposition. However, cases in which the energy deposition time > τ_2 are observed in ASDEX Upgrade, suggesting that other factors, such as the SOL turbulence, contribute at determining the time scale of the heat pulse duration, as detailed exposed in [30]. Such 'time-stretching' is clearly a positive effect, as it attenuates the potentially damaging effect of such very fast thermal transients, although a better understanding of all of the physics lying under transport of thermal energy from the plasma to the PFCs is still needed. Furthermore, in the ITER design, according with guidelines in [29], the conservative assumption that the plasma thermal energy at the time of disruption is equal to the thermal energy of the 'maximum performance' 'parent' plasma has been made. However, in MDs up to 90% of thermal energy is radiated in $\tau_{1\text{-}2}$, while in hot VDEs less than 10% is dissipated in this stage, leading to higher heat loads. Figure 2.7 shows the distribution of before-disruption energy loss observed in a representative samples of 129 shots occurring in JET 'high energy' ($W_{th,max} \geq 4.5\ MJ$) discharges [49]. Approximately 80% of the total have $W_{th,dis}/W_{th,max} \leq 0.5$ and only 13% (almost hot VDEs) presents $0.9 \leq W_{th,dis}/W_{th,max} \leq 1$.

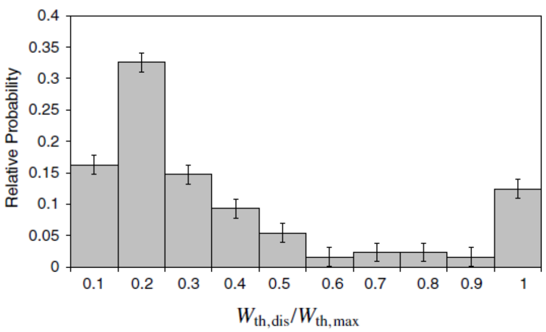

Figure 2.7: Distribution of pre-disruption thermal energy loss in a 129-example sample of disruptions of JET 'high-energy' plasmas. The ratio of thermal energy at the start of the disruption Wth,dis to maximum energy in the discharge Wth,max is plotted. Reprinted from [49].

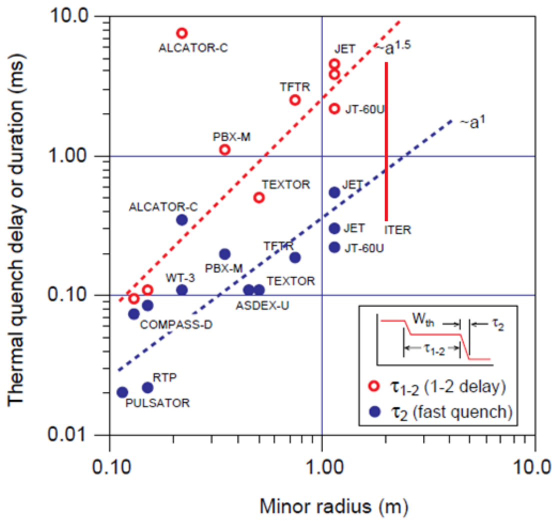

Figure 2.8: Thermal quench times τ1-2 (delay between initial and final quench) and τ2 (fast quench) for various tokamaks, plotted as a function of plasma minor radius. Extrapolation to ITER (a = 2 m) yields τ1-2 ~ 19.9 ms and τ2 ~ 0.7 ms. Riprinted from [29].

Experimental data in the IDDB suggest that the initial delay time, $\tau_{1\text{-}2} \propto a^{1.5}$, and the final fast quench time, $\tau_2 \propto a$, as shown in Figure 2.8. However, the large scatter of experimental data recommends an uncertainty factor from 1/3 to 3 (i.e. for DEMO $\tau_{1\text{-}2}$ ~ 10-100ms and τ_2 ~ 0.3-3ms with a = 2.9m).

The actual value of the TQ duration τ_2 has a slight effect on the EM simulations, because it is shorter than the vessel resistive times and of the same order of the usual cycle time step. As shown in the next Sections, in all the simulations reported in this Thesis it has been assumed that all the plasma energy is dissipated during τ_2 (i.e. $W_{th,dis}/W_{th,max} = 1$), whose duration has been conveniently chosen in relation with the time step assumed for the simulations.

2.4 CQ characterization

The rapid loss of the plasma toroidal current during the CQ can induce significant eddy current that can threaten the mechanical integrity of in-vessel components. Within IDDB, an intense effort was made to place a lower bound on the expected CQ time Δt_{cq}, as necessary in ITER to robustly design in-vessel components. The more recent CQ IDDB data in [35] are shown in Figure 2.9. The CQ rate is usually normalized by the plasma cross-sectional area S in order to better compare CQ rates of different devices (Δt_{cqS}) and typically the time $\Delta t_{80\text{-}20}$ = t_{80} - t_{20} is used to derive the linear CQ rate, where t_{80} and t_{20} are the times where the plasma current reaches 80% and 20% of its pre-disruptive value, respectively (see Figure 2.1). In ITER design the limit was defined equal to 1.67 ms m^{-2} [50]. Plotted versus toroidal current density j_p in Figure 2.9a, the minimum Δt_{cqS} is found to fall under 0.6 ms m^{-2}, far below the ITER minimum (indicated by the horizontal dashed line). However, by plotting Δt_{cqS} versus aspect ratio (Figure 2.9b), it emerges that the distinct shorter Δt_{cqS} are related to the low-A devices (MAST and NSTX). The low-A and conventional distributions can be better equalized if it is introduced an additional normalization in the area-normalized CQ time by the plasma self-inductance L^* = ln (8R/a) - 1.75, yielding to the normalized time Δt_{cqSL} = $\Delta t_{80\text{-}20}$/(SL*). As shown in Figure 2.9c, this normalization significantly increases the overlap of the two populations, resulting in an almost identical lower bound. However, this lower bound falls below the specified ITER minimum. Figure 2.9d shows a magnification of the area below the ITER minimum, populated only by MAST, NSTX and DIII-D. Anyway, as detailed exposed in [50], the shots falling in this region have not been considered in ITER, with the lower bound assumed for IVCs design remaining 1.67 ms m^{-2}.

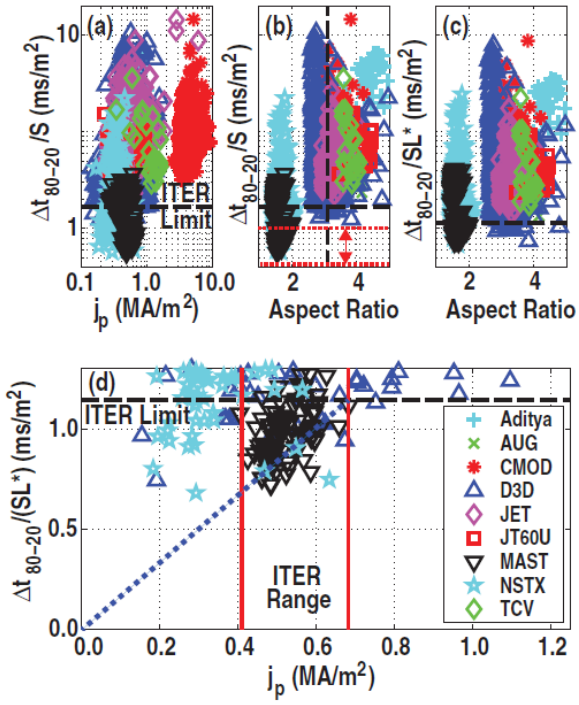

Figure 2.9: (a) Area normalized CQ duration versus toroidal current density (j_p), separated by device. (b) Area normalized CQ duration versus aspect ratio. Red arrow and dotted lines indicates difference between low-A and conventional-A distributions. (c) Additional normalization by the dimensionless self-inductance L^* versus aspect ratio. (d) Magnification of area below ITER limit for area and L^* normalized CQ duration versus j_p. The ITER flattop range of j_p is indicated by the vertical red lines. The black dashed line indicates the ITER minimum. The dotted blue line is an extrapolation to the ITER limit at the maximum ITER j_p. Reprinted from [35].

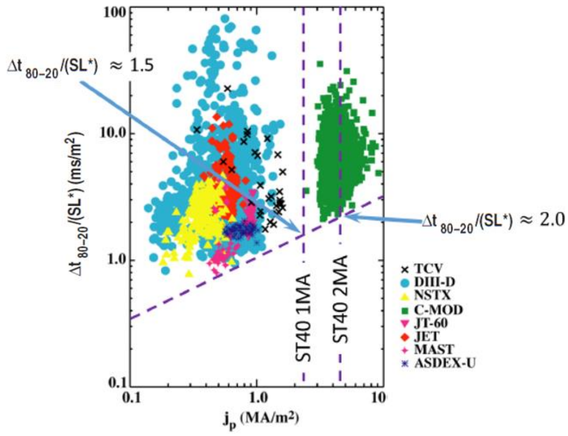

Figure 2.10: $\Delta t_{80\text{-}20}/(SL^*)$ versus j_p with lower limit assumed for ST40 simulations represented by the dashed line. Riprinted from [50].

Since this assumption is connected with the ITER operational space, it can not be extended to DEMO, DTT and ST40. For DEMO, in [51], a lower limit for the area-normalized current decay $\Delta t_{100\text{-}0}$/S = 1.8 ms m^{-2} is chosen. This assumption is reproposed in this Thesis for DEMO and DTT, yielding to the values reported in Table 2-1 (min CQ dur ($\Delta t_{100\text{-}0}$)). In DEMO, since a so-called fast event is considered, the CQ duration assumed in the simulations (CQ dur ass. ($\Delta t_{100\text{-}0}$)) is just that related to this lower bound. Instead, as presented in the related Section, a so-called slow event has been analysed for DTT, considering a total CQ duration of 40ms, a factor 10 greater with respect to the minimum $\Delta t_{100\text{-}0}$ = 4ms shown in table Table 2-1. Regarding ST40, since it operates in range of high j_p, $\Delta t_{80\text{-}20}$ has been calculated according to what shows in Figure 2.10 and Table 2-1, yielding to $\Delta t_{80\text{-}20}$ = 0.9ms.

Table 2-1: CQ duration assumptions for the simulations

DEMO	
Assumption	$\Delta t_{100\text{-}0}$/S = 1.8 ms m^{-2}
S [m^2]	43.37
min CQ dur ($\Delta t_{100\text{-}0}$)	78ms
CQ dur ass. ($\Delta t_{100\text{-}0}$)	78ms
DTT	
Assumption	$\Delta t_{100\text{-}0}$/S = 1.8 ms m^{-2}
S [m^2]	2.20
min CQ dur ($\Delta t_{100\text{-}0}$)	4ms
CQ dur ass. ($\Delta t_{100\text{-}0}$)	10·4ms = 40ms
ST40	
Assumption	$\Delta t_{80\text{-}20}$/(SL*) = 2.0 ms m^{-2}
S [m^2]	0.47
L*	0.999
min CQ dur ($\Delta t_{80\text{-}20}$)	0.9ms
CQ dur ass. ($\Delta t_{80\text{-}20}$)	0.9ms

3 Using MAXFEA code in combination with ANSYS APDL for the simulation of plasma disruption events

In this Section the developed methodology is presented. This novel procedure allows to evaluate the EM loads coming from plasma transients in normal and off-normal (e.g. plasma disruptions) conditions in a 3D detailed way. It is based on the use of MAXFEA code in combination with ANSYS APDL. A schematic representation of the procedure workflow is reported in Figure 3.1.

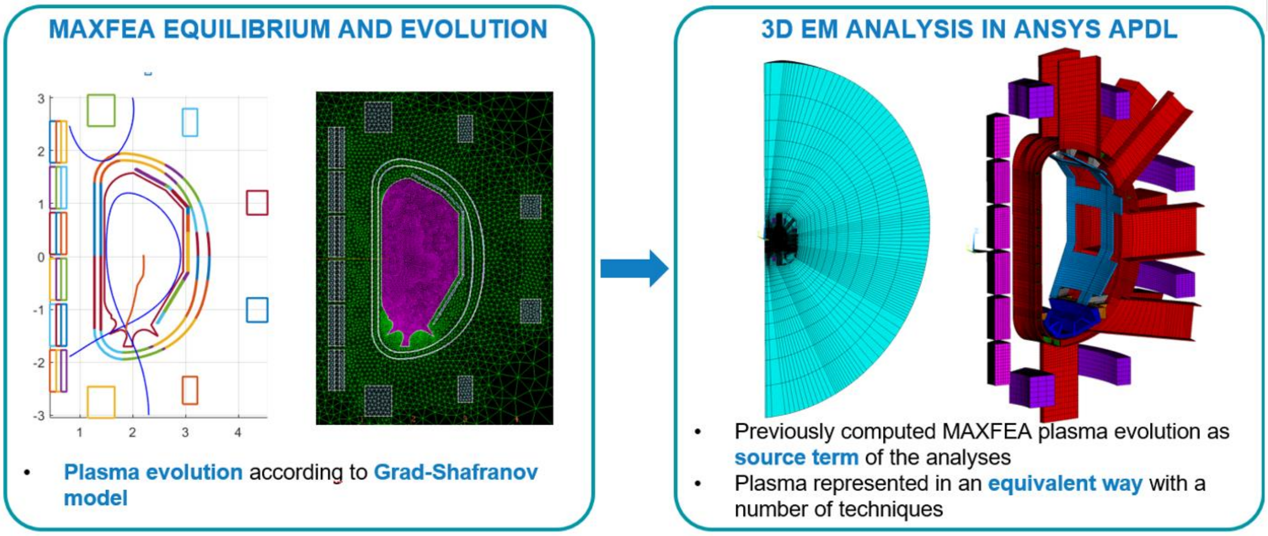

Figure 3.1: MAXFEA-APDL procedure workflow

3.1 Plasma equilibrium and evolution: Grad-Shafranov Equation and MAXFEA code

3.1.1 The Grad-Shafranov Model

In tokamaks the plasma is confined inside a doughnut-shaped (torus) metallic chamber by using a magnetic cage. The principle underpinning the design of the tokamak is that it is possible to induce a toroidal current inside the gas by using the plasma ring as the secondary winding of a transformer. The consequent creation of a poloidal magnetic field acting together with externally imposed toroidal and poloidal fields produces a magnetic cage that traps the ionized particles. The toroidal field B_φ is nearly an order of magnitude more intense than the poloidal component B_θ (B_φ is typically in order of few T). Consequently, the magnetic lines that guide the particles around the major axis of the torus are helices, which rotate slowly in the poloidal direction. Once known the magnetic field configuration, the plasma position is determined.

The temporal evolution of a plasma in a magnetic confinement system such as a tokamak is, in principle, a very complex problem since it is necessary to consider the diffusive processes in the plasma together with electromagnetic phenomena involving the coils, the metallic structures and the plasma itself. The most straightforward model used to describe plasma evolutions is the so-called ideal axisymmetric Magneto-Hydro-Dynamics (MHD). Ideal MHD follows from the assumption (only approximately satisfied) that the plasma has zero electrical resistance. Plasmas are actually slightly resistive, and this discrepancy is the primary source of several behaviours that are not satisfactorily predicted by ideal MHD. However, ideal MHD has been found to be sufficiently accurate for plasma current, shape and position control purposes and it is commonly used as a first approximation method in almost every tokamak magnetic analysis, including real time control [52]. The system of equations of the ideal MHD are governed by quasi-stationary Maxwell's equations, given by

$$\nabla \times \boldsymbol{E} = -\frac{\partial \boldsymbol{B}}{\partial t} \tag{3.1}$$

$$\nabla \times \boldsymbol{H} = \boldsymbol{J} \tag{3.2}$$

$$\nabla \cdot \boldsymbol{B} = 0 \tag{3.3}$$

with the material constitutive relationships:

$$\boldsymbol{B} = \mu \boldsymbol{H} \tag{3.4}$$

$$\boldsymbol{J} = \sigma(\boldsymbol{E} + \boldsymbol{v} \times \boldsymbol{B} + \boldsymbol{E_i}) \tag{3.5}$$

Where $\boldsymbol{E}$ is the electric field, $\boldsymbol{B}$ is the magnetic flux density, $\boldsymbol{H}$ is the magnetic field, $\boldsymbol{J}$ is the current density, t is the time, μ is the magnetic permeability, σ is the electric conductivity, $\boldsymbol{v}$ is the velocity and $\boldsymbol{E_i}$ is the external applied electric field. In the plasma region, the plasma velocity is determined by the momentum balance:

$$\rho\left(\frac{\partial \boldsymbol{v}}{\partial t} + \boldsymbol{v} \cdot \nabla \boldsymbol{v}\right) = \boldsymbol{J} \times \boldsymbol{B} - \nabla p \tag{3.6}$$

Pressure p, velocity $\boldsymbol{v}$ and density ρ are coupled with the continuity and conservation of energy equations:

$$\frac{\partial(p\rho^{-\gamma})}{\partial t} + \boldsymbol{v} \cdot (p\rho^{-\gamma}) = 0 \tag{3.7}$$

$$\frac{\partial \rho}{\partial t} + \nabla \cdot (\rho \boldsymbol{v}) = 0 \tag{3.8}$$

Where in (3.7) adiabatic behaviour and entropy conservation is assumed for the fluid.

Conveniently considering a cylindrical coordinate system (r,φ,z) and assuming an axisymmetric behaviour of the system (i.e. all quantities are independent from the toroidal direction φ), it is possible to express $\boldsymbol{B}$ and $\boldsymbol{J}$ in function of two important scalar functions, namely the poloidal magnetic flux ψ and the poloidal current function f. The poloidal magnetic flux ψ is defined as the magnetic flux linked to circumference obtained by revolving the point (r,z) around the z-axis (see Figure 3.2):

$$\psi_{pol} = \oiint_S \boldsymbol{B} \cdot \hat{n}\, dS \tag{3.9}$$

Actually, ψ is the poloidal flux per radian $\psi = \psi_{pol}/2\pi$ that is more frequently used to simplify the expressions. Analogously, f is the flux of the poloidal current. As shown in [53], using ψ and f, it is possible to express $\boldsymbol{B}$ and $\boldsymbol{J}$ as:

$$\boldsymbol{B} = \frac{1}{r}\nabla\psi \times \boldsymbol{i_\varphi} + \frac{f}{r}\boldsymbol{i_\varphi} \tag{3.10}$$

$$\boldsymbol{J} = \frac{1}{r}\nabla\left(\frac{f}{\mu}\right) \times \boldsymbol{i_\varphi} - \frac{1}{\mu_0 r}\Delta^*\psi\ \boldsymbol{i_\varphi} \tag{3.11}$$

Where $\boldsymbol{i_\varphi}$ is the unit vector in the toroidal direction, μ_0 is the magnetic permeability of the vacuum and Δ^* is a second-order differential operator defined by:

$$\Delta^*\psi \equiv r\frac{\partial}{\partial r}\left(\frac{1}{\mu_r r}\frac{\partial\psi}{\partial r}\right) + \frac{\partial}{\partial z}\left(\frac{1}{\mu_r}\frac{\partial\psi}{\partial z}\right) \tag{3.12}$$

Where μ_r is the relative magnetic permeability, which is unity in a vacuum but also in non-magnetic materials such as air and plasma.

Regarding the axisymmetric approximation, it has been shown that axisymmetric effects play a crucial role in elongated plasma [54][55]. Furthermore, the influence of the currents induced in the actual three-dimensional structures by the time-varying magnetic field during a plasma evolution has been studied in [56][57], showing that their main effects on the plasma can be reproduced by introducing a set of equivalent axisymmetric circuits.

Introducing the further assumption that inertial effects can be neglected (i.e. plasma evolves in a quasi-static approximation), which is reasonable since the extremely small plasma mass and considering the typical time scales of plasma evolution (e.g. plasma disruptions), (3.6) becomes:

$$\boldsymbol{J} \times \boldsymbol{B} = \nabla p \tag{3.13}$$

From which $\boldsymbol{J} \cdot \nabla p = 0$ and $\boldsymbol{B} \cdot \nabla p = 0$. Considering (3.10) and (3.11), these relations yield to $\nabla p \times \nabla\psi = 0$ and $\nabla p \times \nabla f = 0$, that implies that also $\nabla f \times \nabla\psi = 0$. Taking into account these relations and introducing (3.10) and (3.11) in the equilibrium condition (3.13), with some algebra it is possible to obtain:

$$\Delta^*\psi = -\mu_0 r^2\frac{\partial p}{\partial\psi} - f\frac{\partial f}{\partial\psi} \tag{3.14}$$

That is the so-called Grad-Shafranov equation.

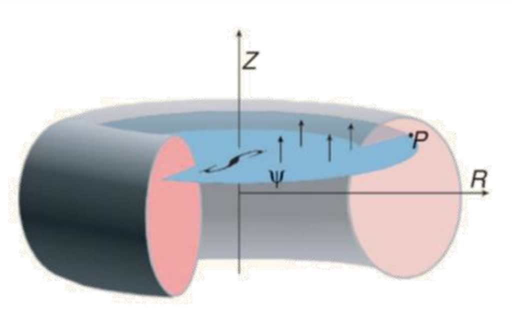

Figure 3.2: poloidal magnetic flux through the surface S

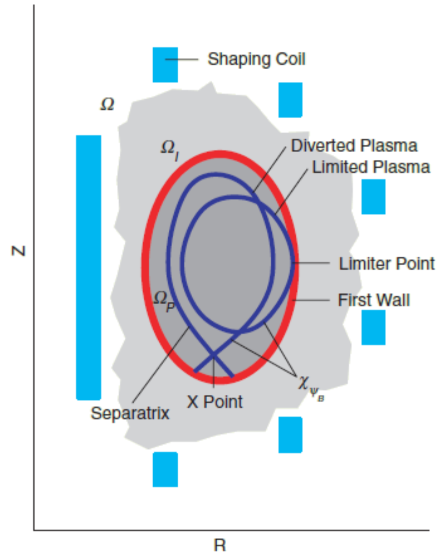

Figure 3.3: Poloidal cross section of a tokamak. In the poloidal plane Ω, the domain ΩI is the inner region of the coils, while the plasma region is Ωp

In Grad-Shafranov equation the sum of the two terms at the right-hand side of the equal sign represents the plasma toroidal current density J_ϕ. The equation describes the equilibrium and the quasi-static evolution for an isotropic (showing the same physical properties in all directions) plasma. This formulation can be extended to various domains, where the magnetic flux is present. It can be observed that, according to Poisson's equation, the term $\Delta^*\psi$ is equal to zero in the vacuum region. Moreover, $\Delta^*\psi$ is proportional to the toroidal current density $J_{\Phi,ext}$ in the poloidal shaping coils or in other external conductor domains.

To summarize, the plasma equilibrium is completely characterized on the poloidal plane by the following non-linear PDE problem [53]:

$$\Delta^*\psi = \begin{cases} = 0 & \textit{in vacuum} \\ -\mu_0 r^2 p' - FF' & \textit{in the plasma domain} \\ -\mu_0 r J_{\phi,ext}(r,z) & \textit{in the external conductor domain} \end{cases} \tag{3.15}$$

$$\begin{gathered} \psi(r,z,0) = \psi_0(r,z) \\ \psi(0,z,t) = 0 \\ \lim_{r^2+z^2\to\infty} \psi(r,z,t) = 0 \end{gathered} \tag{3.16}$$

The system of equations (3.15) together with Boundary Conditions (BCs) (3.16) is used to calculate the poloidal flux ψ at the time t once that $J_{\Phi,ext}$ is known and $p(\psi)$ and $f(\psi)$ are defined. Rigorously, $p(\psi)$ and $f(\psi)$ should be determined by the resolution of the transport equations (3.6), (3.7) and (3.8). Anyway, it is well known that the use of small number of scalar degrees of freedom (DOF) provides a sufficient basis for an adequate description of MHD equilibria. In [58] it is shown that the plasma current profile can be approximately represented by three DOF, namely the total plasma current *Ip*, poloidal beta β_p and internal inductance *li*, defined as:

$$\beta_p = \frac{4}{\mu_0 r_c I_p^2}\int_{V_P} p d\tau \tag{3.17}$$

$$l_i = \frac{4}{\mu_0 r_c I_p^2}\int_{V_P} \frac{B_p^2}{2\mu_0} d\tau \tag{3.18}$$

where r_c is the horizontal coordinate of the plasma current centroid (r_c, z_c) defined as:

$$r_c = \left(\frac{1}{I_p}\int_{\Omega_P} r^2 J_\phi dS\right)^{\frac{1}{2}} \tag{3.19}$$

$$z_c = \frac{1}{I_p}\int_{\Omega_P} z J_\phi dS \tag{3.20}$$

From which it appears clear that β_p and *li* are measure of the plasma internal distribution of pressure and current.

Using this approximation, the functions $p(\psi)$ and $f(\psi)$ can be expressed in terms of *Ip*, β_p and *li*. Therefore, (3.15) becomes a free boundary problem (i.e. plasma boundary is one of the unknown) which gives the plasma equilibrium at each time *t* once the plasma parameters *Ip*, β_p and *li* are preassigned and the toroidal current density $J_{\Phi,ext}$ in the external conductors is given or dynamically determined. The plasma boundary is usually defined to be the outermost closed magnetic flux surface entirely contained inside the vacuum vessel and is determined by an iterative calculation. Topologically, the boundary is either the outermost flux contour not intersecting any solid object or it is a separatrix, that is, a surface containing an X-point (Figure 3.3), which is a point where the poloidal magnetic field is zero, or, equivalently, the flux function presents a saddle point. The X-point often exists independently of whether it is a part of the most external closed flux surface. Two domains of interest can be identified on the poloidal plane Ω in order to determine the plasma shape (Figure 3.3):

- Ω_I is the region enclosed by the shaping coil locations;
- the subset Ω_P of Ω_I is the *plasma region*, defined as the vacuum region interior to the containment vessel, where plasma may exist.

The flux function ψ defined in the domain Ω_I is a real-valued function of *r* and *z* monotonically decreasing from the center of the plasma toward the edge. The boundary flux value ψ_b, which identifies the plasma boundary surface $\chi_{\psi b}$, is determined by comparing the flux value ψ_X at the X point with the maximum value $\psi_{\text{firstwall}}$ of the flux along the first wall, which is constituted by the plasma facing structures. When the X-point flux is higher than $\psi_{\text{firstwall}}$, the *separatrix* is internal to every flux surface touching the wall, and, consequently,

the plasma boundary coincides with the part of the *separatrix* inside the plasma domain Ω_P (Figure 3.3). In this case, the plasma is in a *diverted configuration*, otherwise, it is a *limited configuration*, physically touching the first wall at the limiter point P_{limiter} characterized by $\psi(P_{\text{limiter}}) = \psi_{\text{firstwall}}$.
Through the years, several numerical codes, that requires iterative procedures, have been developed to solve the ideal axisymmetric MHD equilibrium problem. Among others, CarMa0NL [59], DINA and TSC [60] codes have been intensively used in the ITER design.

3.1.2 MAXFEA code

MAXFEA code is a 2D ElectroMagnetic equilibrium code that solve the Grad-Shafranov non-linear problem with a FEM approach. It was created by Pietro Barabaschi in 1991-1992 [61]. MAXFEA allows to perform both static and dynamic simulations, based on the dynamics of the external coil currents and either a bulk or distributed plasma current. The plasma equations are coupled with the circuits equations for the active and passive conductors surrounding the plasma region. The numerical technique employed to compute the solution is based on the finite-element formulation (the equations are solved on the vertices of the mesh triangles). MAXFEA provides a complete magnetic description of the plasma, including both the plasma current density distribution and the flux distribution. The input data are provided by the code itself, in form of simulated currents in all conductors, including plasma. It allows to perform dynamic plasma evolutions in normal or off-normal (e.g. disruptions) conditions, driven by pre-programmed or user activated events. MAXFEA code could be used for different purposes such model the magnetic configuration to optimize plasma shape, perform dynamic simulation of the magnetic configuration evolution along the discharge, simulate plasma disruptions, assess the performances of a closed loop control system in keeping the perturbed plasma [62], evaluate fields and forces in operation and disruption conditions and so forth. An example of a typical MAXFEA model is reported in Figure 3.4, while in Figure 3.5 an example of an equilibrium computed by means of MAXFEA is shown.
The Grad-Shafranov parametrization used in the code expresses $p(\psi)$ and $f(\psi)$ as function of the parameters α and β (inputs of the code), that are respectively related to li and β_p:

$$p(\bar{\psi}) = p_a\left(-\frac{\alpha+1}{\alpha}\bar{\psi} + \frac{1}{\alpha}\bar{\psi}^{\alpha+1} + 1\right) \tag{3.21}$$

$$f(\bar{\psi}) = f_a\sqrt{\left(1+\frac{1}{\alpha}\right)\left(\frac{\alpha+1}{\alpha} - \bar{\psi} + \frac{\bar{\psi}^{\alpha+1}}{\alpha+1}\right)} \tag{3.22}$$

Where $\bar{\psi} = (\psi - \psi_a)/(\psi_b - \psi_a)$ is the normalized flux. Note that α appears explicitly in the equations, while β is implicitly absorbed in p_α and f_α , that are respectively plasma pression and poloidal current function values in correspondence of the plasma magnetic axis.

When used for disruptions simulations, MAXFEA allows to evolve a reference starting equilibrium according to a predefined disruption scenario following a series of pre-programmed or user activated events. In addition to provide a complete description of the plasma evolution in terms of plasma movement, current distribution, magnetic field, and so forth, MAXFEA provides information on the EM loads acting on the components as result of the interaction between the toroidal currents, both external and induced, and the poloidal field. This kind of interaction is typically the dominant term in the eddy current related global forces in the components. Therefore, MAXFEA provides a good approximation in terms of total currents and forces induced in the structures. However, being an axisymmetric code, MAXFEA provides only a limited and partial understanding of what really happens in the 3D structures. In fact, in an actual tokamak geometry the presence of ports, divertors, IVCs, etc, with local electrical connections, toroidal discontinuities and so forth, produces non-trivial currents paths and, therefore, non-trivial forces concentrations. These forces are typically non-negligible and must be evaluated to study the related mechanical response of the components. In order to overcome this limitation, a procedure based on the use of MAXFEA code in combination with ANSYS APDL has been developed and presented later in this Section.

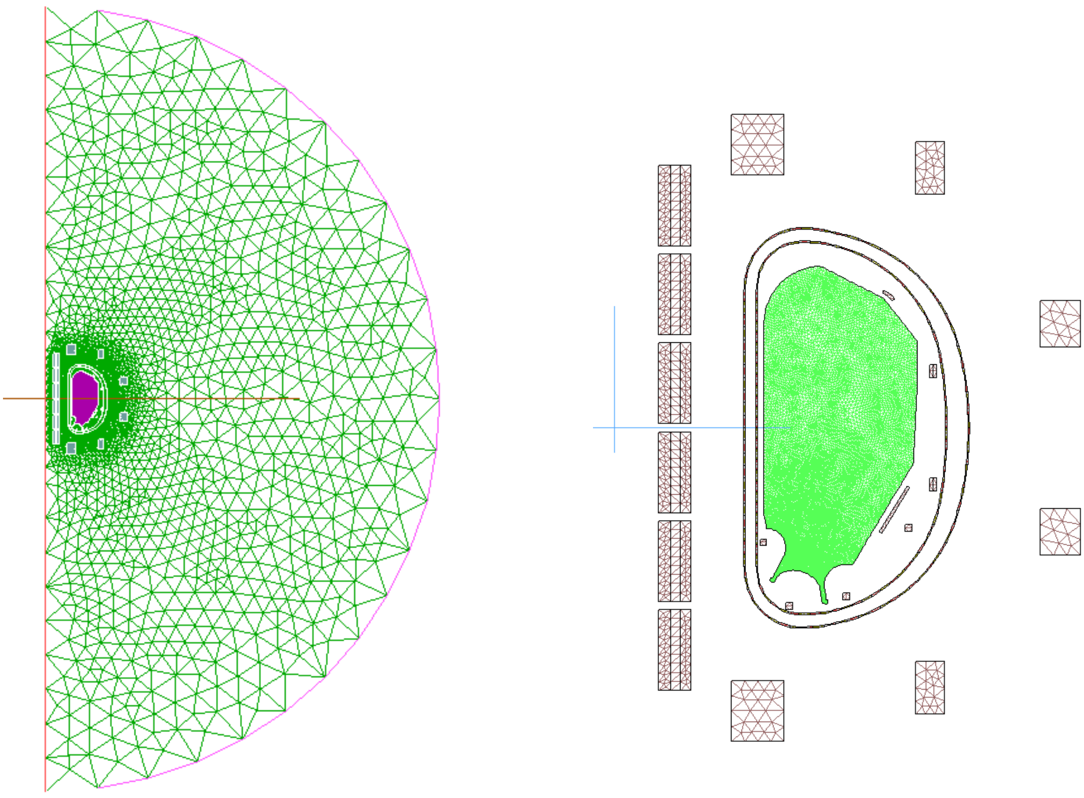

a) b)

Figure 3.4: MAXFEA DTT Model a) Overview b) Zoom of the VV, coils and plasma regions

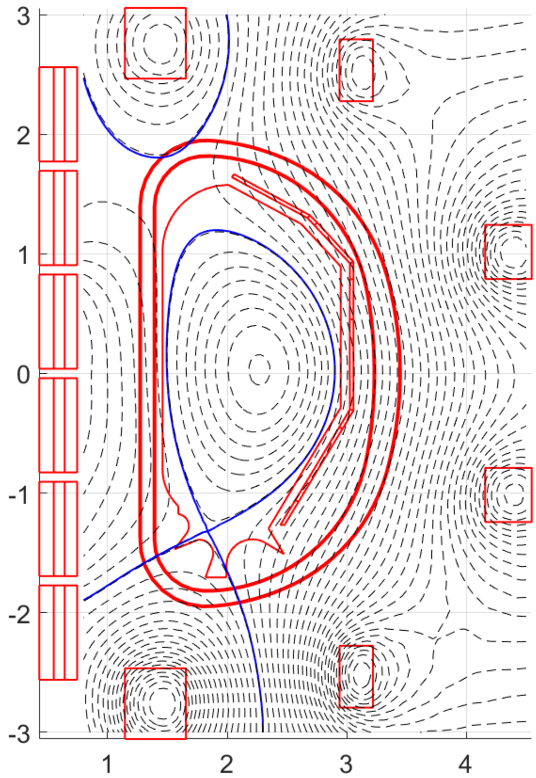

Figure 3.5: DTT SN 5.5 MA computed by means of MAXFEA code

3.1.2.1 Halo current in MAXFEA

As discussed in Section 2, Halo Current represent one of the main EM loads on the components during disruptions. MAXFEA code treats the HC with a first-principle method. Since MAXFEA assumes that plasma evolves with quasi-static approximation, the plasma is always in a state of mechanical equilibrium and therefore the following force balance holds:

$$F_{pla} = F_{coils} + F_{eddy} + F_{halo} = 0 \tag{3.23}$$

Where F_{coils} is the force that the external active coils exert on the plasma, while F_{eddy} is the force that the plasma experiences due to the presence of induced eddy currents in the surrounding structures. From this force balance MAXFEA can estimate the *global* force that HC should exert on the structures. During the evolution, the halo behaviour is simulated by defining the overall plasma boundary as the magnetic surface corresponding to a magnetic flux equals to the flux of the LCFS minus a *chosen fraction*, defined through an input parameter. Then, the *total amount* of HC is estimated starting from the force balance and this assumption on the *halo region width*. In Figure 3.6 a snapshot of the DTT plasma equilibrium during the CQ phase of the downward VDE scenario is reported, showing the halo region and a qualitative representation of the related force.

With this approach MAXFEA allows to evolve the plasma considering the presence of the HC. Anyway, MAXFEA is not able to track detailed HC path into the structures, but it provides only a global information of the total poloidal halo current expected. Indeed, the exact poloidal path in the 3D structures of such currents has no significant influence on the axisymmetric plasma evolution, since they mainly produce toroidal field, which is not relevant in the solution of axisymmetric equilibrium.

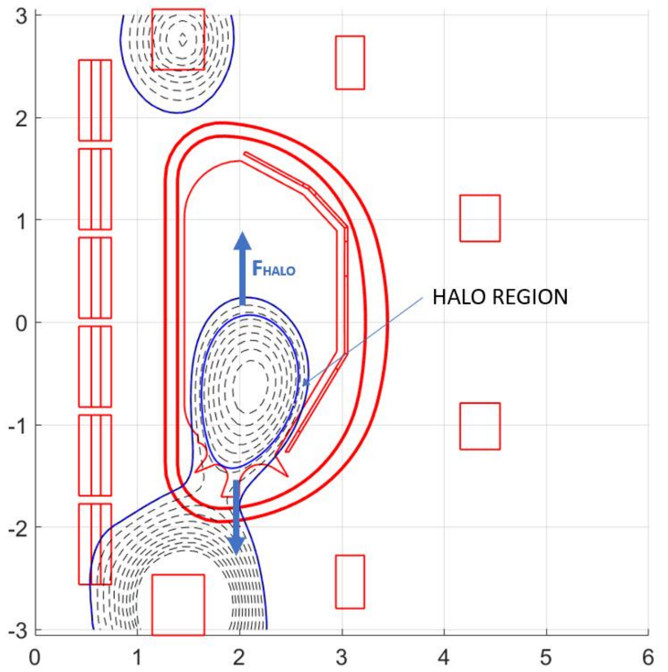

Figure 3.6: Representation of HC region during the CQ phase of the DTT downward VDE

3.2 From MAXFEA to ANSYS: 3D detailed EM analysis

Downstream a MAXFEA simulation, 3D models in ANSYS APDL environment are developed and then the previously computed MAXFEA plasma evolution is introduced in the models. In this way, the plasma becomes the source terms of the 3D analyses. In particular, the plasma is represented in the 3D models in an equivalent way with a number of techniques, as described later in this Section.

The three main sources of EM loads on the structures during plasma disruptions are: the Poloidal Field Variation (PFV) and the Toroidal Field Variation (TFV) during plasma evolution, especially during the Thermal Quench (TQ) and the Current Quench (CQ), and the Halo Currents (HC), significative during the CQ. Eddy currents coming from the PFV are mainly in toroidal direction and mostly interact with Poloidal Field. On the other hand, the currents induced by TFV and HC are mainly poloidal and mostly interact with the Toroidal Field. These forces are in-plane forces. The misalignment between the poloidal components of the eddy and halo currents and the poloidal magnetic field, could produce locally out of plane forces within the passive structures and also a net force. However, the latter is typically negligible with respect to the in-plane net forces.

The procedure presented in this Section is composed of three main workflows, to include PFV, TFV and HC contributions inside ANSYS APDL.

As far as the PFV is concerned, the plasma is introduced and represented in the model by means of a set of equivalent filaments able to reproduce the same PFV in time previously computed by means of MAXFEA. The PFV analysis is basically connected with the plasma movement and current evolution. Therefore, it is important to well simulate the distribution of the current both in space and in time with a proper choice of the filaments set. A schematic representation of the proposed workflow is depicted in Figure 3.7.

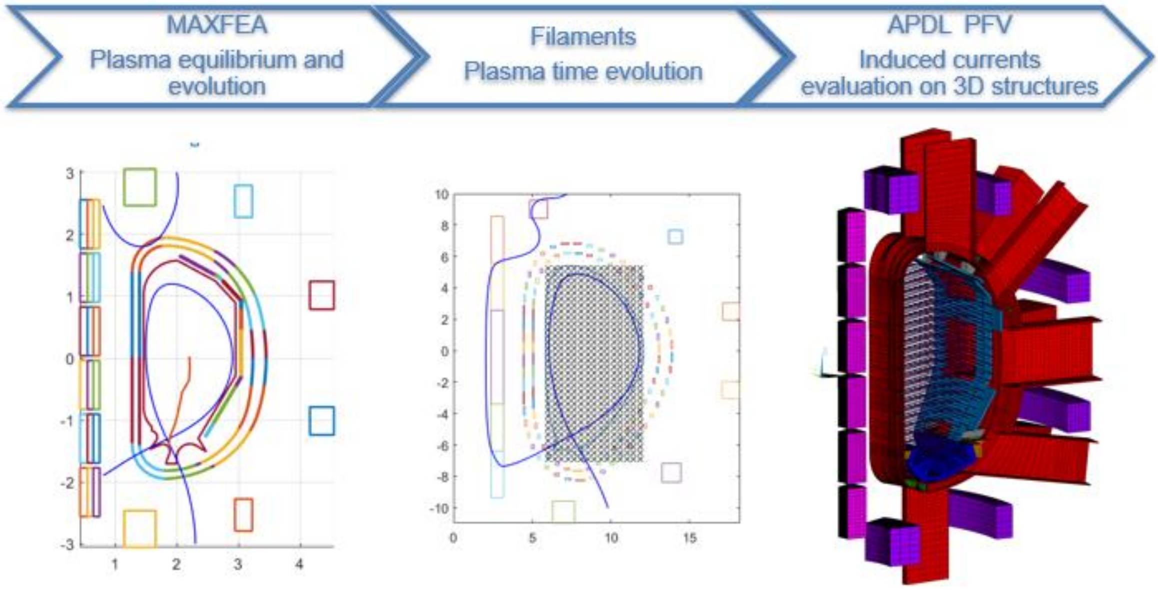

Figure 3.7: Adopted workflow for the evaluation of currents and forces on 3D structures coming from PFV: a) MAXFEA simulation of plasma equilibrium evolution according to a disruption scenario; b) generation of a filaments grid with the capability to simulate the same plasma evolution of MAXFEA in terms of PFV; c) 3D simulation within ANSYS APDL environment; filaments used as source terms

Regarding the TFV analysis (Figure 3.8), in this case the plasma is represented in a different way:

1) A torus with a thin thickness is defined in the plasma region and modelled inside the 3D model developed within ANSYS APDL environment (Figure 3.8b).
2) An equivalent poloidal current in the rectangular torus able to reproduce the same plasma TFV evolution previously computed in MAXFEA is determined and used as source term for the EM transient analysis (Figure 3.8c).

In order to compute the equivalent poloidal excitation current in the defined rectangular torus the following analytic approach is proposed. For a rectangular torus with infinitesimal thickness (Figure 3.9) onto which flows a poloidal current uniformly distributed along the toroidal direction, from the Ampere law and following symmetry consideration:

$$B(r) = \frac{\mu_0 i_p a}{r} \tag{3.24}$$

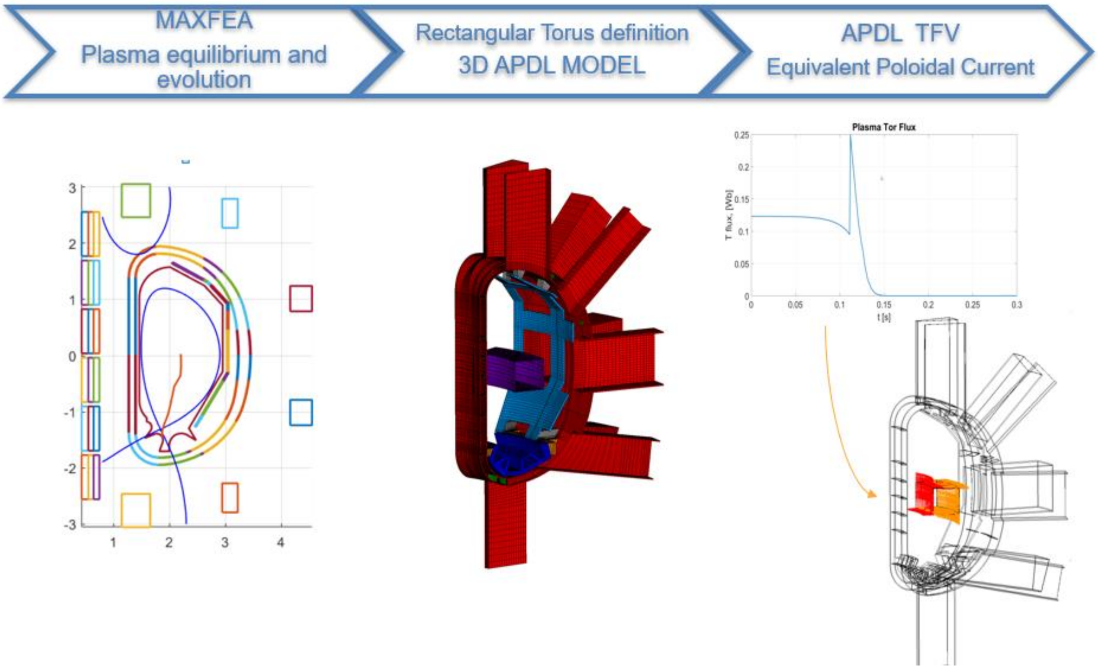

Figure 3.8: Adopted workflow for the evaluation of currents and forces on 3D structures coming from TFV: a) MAXFEA simulation of plasma equilibrium and evolution according to disruption scenario; b) A rectangular torus with thin thickness is modelled inside the 3D model developed within ANSYS APDL environment; c) An equivalent poloidal current is determined and used as source term.

Where B is toroidal field inside the rectangular torus, a is shown in Figure 3.9 and i_p is the poloidal current per meter [A/m] such that the total poloidal current in the torus will be:

$$Ip = i_p 2\pi a \tag{3.25}$$

From equation (3.24), the toroidal flux through the torus cross-section ϕ_B will be:

$$\phi_B = \mu_0 i_p a h \ln\left(\frac{b}{a}\right) \tag{3.26}$$

From equation (3.26) is then possible to estimate i_p once that ϕ_B evolution is known (namely the plasma TFV evolution computed with MAXFEA):

$$i_p = \frac{\phi_B}{\mu_0 a h \ln\left(\frac{b}{a}\right)} \tag{3.27}$$

Finally, from equation (3.27) is possible to compute the poloidal current to impose at each element of the rectangular torus, with a thin thickness, defined in the TFV model:

$$i_{ele} = \frac{i_p \theta a}{n_{ele\_tor}} \tag{3.28}$$

Where n_{ele_tor} is the number of elements in toroidal direction and θ is the toroidal angle extension of the implemented TFV model. It should be noted that the mesh of the rectangular torus should be modelled with the same toroidal angle extension for all the elements. This approach is valid in the limit in which the rectangular torus features a thin thickness.

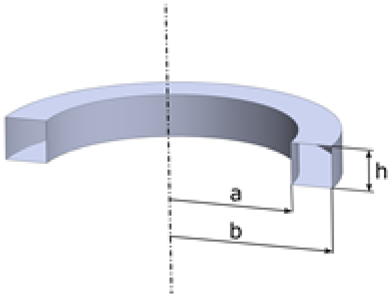

Figure 3.9:Main parameters of the rectangular torus with infinitesimal thickness

As far as the HC analysis is concerned, the proposed workflow is depicted in Figure 3.10. As discussed before, MAXFEA provides information on the global poloidal halo current, without tracking detailed HC paths into the structures. In order to evaluate 3D detailed HC distribution in the structures, the following approach is proposed. Firstly, in analogy with what it was done for ITER [63], possible in and out locations for the HC are assumed according with the MAXFEA simulation and possibly considering conservative conditions from the point of view of the EM loads (Figure 3.10c). These in and out locations represent the interface between the ex-plasma halo region and the PFCs. Then, starting from the information on the *global* HC expected from the previous MAXFEA simulation (Figure 3.10b), the HC is injected through the considered in and out locations in the 3D ANSYS model.

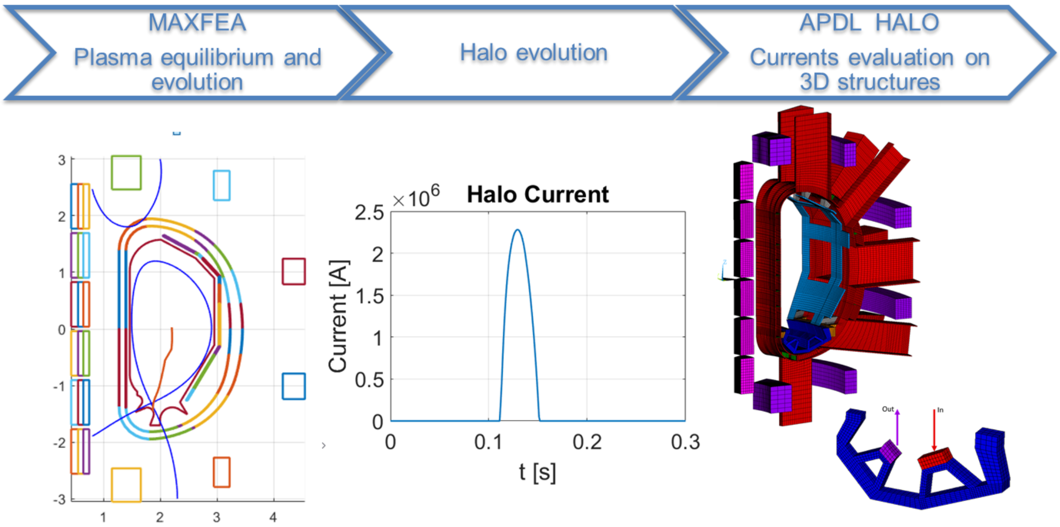

Figure 3.10: Adopted workflow for the evaluation of currents and forces on 3D structures coming from HC: a) MAXFEA simulation of plasma equilibrium and evolution according to disruption scenario; b) The global HC expected is extracted from MAXFEA simulation; c) The HC is injected into the structures in the 3D APDL model assuming possible in and out locations (in figure it is reported the ITER divertor from [6])

Finally, all the EM contributions (PFV, TFV and HC) obtained with 3D simulations, are combined in the post-processing phase with a linear superposition. In particular, it is worth to say that the models for the different analyses are developed in a such way that by simply changing the element type and the properties of specified set of the elements it is possible to obtain one model from the others, i.e. models share the same mesh. In this way, the various EM contributions can be easily added element by element, facilitating the post-processing operations.

One of the main advantages of the proposed approach is that the analyses are completely modular: each EM contribution on each component can be isolated and deeply analysed if needed. This circumstance permits to divide non-trivial evolutions of the currents, fields and forces in more elementary sub-contributions, facilitating a deeper understanding of the phenomenon. Clearly, this approach is possible until ferromagnetic materials are not present in the models, that is the case of all the applications reported in this Thesis. This possibility allows to run separate analysis for each EM contribution, exploiting the Magnetic Vector Potential (MVP) formulation provided by ANSYS [64]. Nevertheless, this procedure can be extended also to the case in which ferromagnetic non-linearities have to be considered, in much similar fashion to what presented in [65], being careful to use the appropriate problem formulation in ANSYS, namely the Edge-Based formulation. Regardless of whether one is analysing phenomena in the steady state, transient or frequency domain, it is always highly desirable to reduce the size of the model as much as possible to minimize the computational resources and time required to solve the model. In fact, the mesh size is a known problem for this kind of analysis. The high complexity of the tokamak system is due to the numerous in-vessel and in-cryostat components, e.g. auxiliary systems, diagnostics, etc. Moreover, they are never fully symmetric in toroidal direction, but each sectors could have specific features. Fortunately, it is often possible to simplify the problem and identify symmetric regions (from the physical point of view) that can represent the whole system with the desired level of accuracy required for the purpose of the considered analysis. Disruptions analysis are often focused on the evaluation of the loads on the tokamak main structures, such as the VV, the in-vessel components, the coils and so forth. Therefore, it is often possible to neglect the presence of ‘small’ systems (e.g. diagnostics, antennas, etc) that do not have a strong influence on the loads experienced in such components. In any case, these simplifications depend strongly on the phenomenon analysed and on the specific features of the device considered. In this Thesis, the identification of all the possible simplifications including the individuation of representative region of minimum amplitude was the first step in the models development. In this way, it was possible to exploit the typical cyclic symmetry of this kind of devices to reduce the dimension of the models resorting to the use of cyclic BCs. If not otherwise stated, the adopted element type in the models was the SOLID97 [64]. This element type features up to 4 Degrees of Freedom (DoF), namely the three vector potential A components (for all conductive and non-conductive elements) and the VOLT (for current induction). In the three kind of analysis different kind of cyclic BCs have to be applied: orthogonal magnetic field at the lateral surfaces for the TFV and the HC; tangent field at the lateral surfaces for the PFV. In terms of excitations, as discussed, poloidal excitation currents are required for the TFV and HC while toroidal excitation currents are introduced in the PFV.

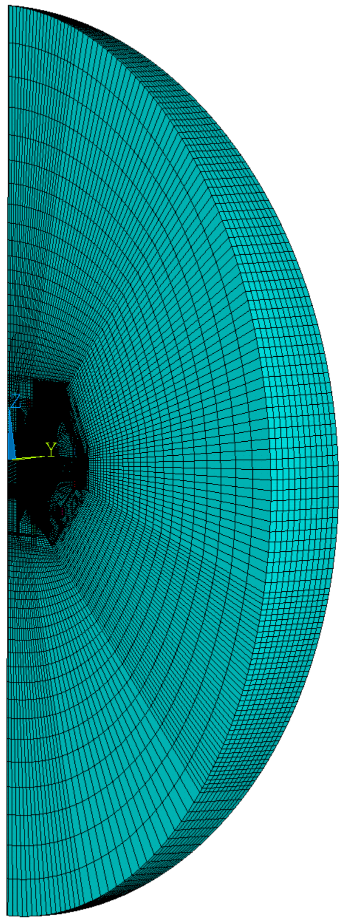

Figure 3.11: Overview of the whole DEMO model FEM domain (sphere sector)

4 DEMO

DEMO is the ultimate goal of the EU roadmap: a fully-integrated science and technology fusion power plant able of long operation time, tritium self-sufficiency and net electricity output, demonstrating the viability of fusion as an alternative energy source for electricity generation. Although DEMO is expected to benefit largely from the know-how gained with the design, construction and operation of ITER, important areas where DEMO requires significant progress compared to ITER still remain, either because the corresponding solution found in ITER is not suitable in DEMO or because the issues are DEMO-specific and not present in ITER [9]. Indeed, the current DEMO pre-conceptual design phase [8] focuses largely on these areas. In particular, eight key design integration issues (KDIIs) have been identified as critical and selected for their high impact on plant and tokamak architecture, safety and maintainability [66]. All of the KDIIs affect in their resolution the design and the technology of the main DEMO key systems, such the Breeding Blanket (BB). Among them, one of these KDIIs is represented by the protection of the first wall (FW) during plasma transients. The present DEMO BB FW has a steady-state heat load capability of no more than ~1-2MW/m^2 [67]. This limit would be easily exceeded during plasma transient for both normal (e.g. plasma ramp-up/down) and off-normal events (e.g. unforeseen plasma perturbations, disruptions, etc), when the plasma comes in contact with the FW. Currently, the strategy for protecting the DEMO FW from plasma transients includes the introduction of discrete high heat flux limiters [68]. These limiters should protect the BB FW from damage, while at the same time their number should be minimized in order to reduce the impact on the Tritium Breeding Ratio (TBR) and cost/complexity. Therefore, the individuation of all the possible locations of plasma-wall contact represents an important information for an optimal design of these components.

To support the deployment of DEMO wall protection strategy, the development of comprehensive analyses is essential to understand the implications of transient perturbation on plasma shape and evolution. The occurrence of such perturbation (e.g Edge Localized Modes (ELMs), unforeseen H-L and L-H transitions, minor disruptions (mDs), etc.) is strongly connected to variations of plasma internal parameters and, consequently, to plasma displacements. If they are coupled with the natural vertical instability of the plasma, plasma perturbations could trigger, ultimately, uncontrolled VDEs with the plasma colliding the upper or lower part of the PFCs. In this context, MDs are also a matter of concern since the plasma often develops vertical instability after the TQ and eventually comes in contact with the FW during its evolution. Recently, the candidate has been directly involved in studies related to plasma perturbations in DEMO relevant scenarios, that led to a journal publication [69]. In this work, a multi-tokamaks study supported by the construction of an inter-machine database containing experimental transient plasma perturbations and disruptions (MDs and VDEs) from JET and ASDEX Upgrade (AUG) has been carried out. The aim was to characterize some plasma perturbations that may lead to high control efforts by the vertical stability system in terms of variations of the plasma internal parameters and vertical displacements. In this context, MAXFEA code was used to reproduce some of the database experimental plasma perturbations and disruptions in JET and ASDEX. Then, such experimental transient plasma perturbations and disruptions have been opportunely scaled to DEMO reference geometries considering different magnetic configurations and simulated by means of MAXFEA to evaluate the related plasma evolutions and, consequently, all the possible plasma-wall contact zones interested. The EM loads in terms of current and forces on the DEMO structures have been also computed. This study gave the opportunity to carry out an important V&V activity. In fact, MAXFEA was extensively validated against experimental JET and ASDEX discharges and benchmarked against other predictive analysis on DEMO (this work is not explicitly presented in this Thesis but the reader is warmly advised to refer to [69] for further information). However, the EM loads on the IVCs such as the BB could not be evaluated with MAXFEA 2D simulations. In fact, in the BB modules no net toroidal current can flow and the EM loads are a complex combination of 3D eddy current loops and halo paths with poloidal and toroidal fields. Therefore, detailed 3D EM analyses have to be considered for a comprehensive evaluation of EM behaviour of this kind of structures. In the recent years, a strong effort has been made to define a methodology for the implementation of consistent EM analyses of the BB, as presented in [65]. Due to the complexity of the considered system, EM loads are evaluated by means of different EM codes (e.g. DINA [60], CARIDDI [70], CarMa0NL [59], MAXWELL [71], etc.) that rely on various numerical approaches.

Based on the use of MAXFEA code, proved to be a reliable tool with the capability to reproduce experimental plasma transients [69], and APDL, that allows to overcome the limitations of 2D simulations, the methodology proposed in this Thesis offers a valid alternative tool to be used in this context. Indeed, it has been recently included as part of the integrated design strategy for DEMO FW protection from plasma transients, whose recent update is given in [72] (the candidate is directly involved in this journal publication as co-author).

This Section presents the application of the developed procedure to a simplified DEMO model, in which the presence of ferromagnetic effects is neglected. The relative low level of complexity allowed to better understand the correctness of PFV and TFV transfer from MAXFEA to 3D APDL model and develop the whole procedure. In this context was possible to evaluate deeply how the PFV and TFV contributes interact with both poloidal and toroidal EM field. This DEMO simplified model includes only the PF coils system and the VV with ports, neglecting the presence ferromagnetic IVCs, i.e. the BB and Divertors systems. Since no IVCs are considered in this simplified testcase, HC computed inside MAXFEA is not then used within 3D analysis. Hence, only the EM contributions related to PFV and TFV coming from MAXFEA simulation are transferred inside ANSYS APDL.

This study was the testbed for the validation of the proposed methodology. Once validated, its reliability has been recognized in EUROfusion and the developed procedure was included as part of the DEMO FW protection integrated design strategy [72], to be used in future more detailed studies in this context (e.g. increasing the complexity of the models by including IVCs and considering ferromagnetic non-linearities). Furthermore, it was also successfully applied in much more detailed analyses in the context of DTT and ST40 projects, as presented in Section 5 and Section 6 respectively.

The study herein presented is the subject of the journal publications reported in [73].

4.1 Numerical models

4.1.1 MAXFEA 2D axisymmetric model

An overview of the MAXFEA model is shown Figure 4.1a. In Figure 4.1b the reference DEMO PMI SN equilibrium at the end of flat top of the plasma scenario reproduced with MAXFEA is reported together with that computed by means of CREATE-NL code [74], that is commonly used in EUROfusion. The comparison highlights a very good agreement between the two codes.

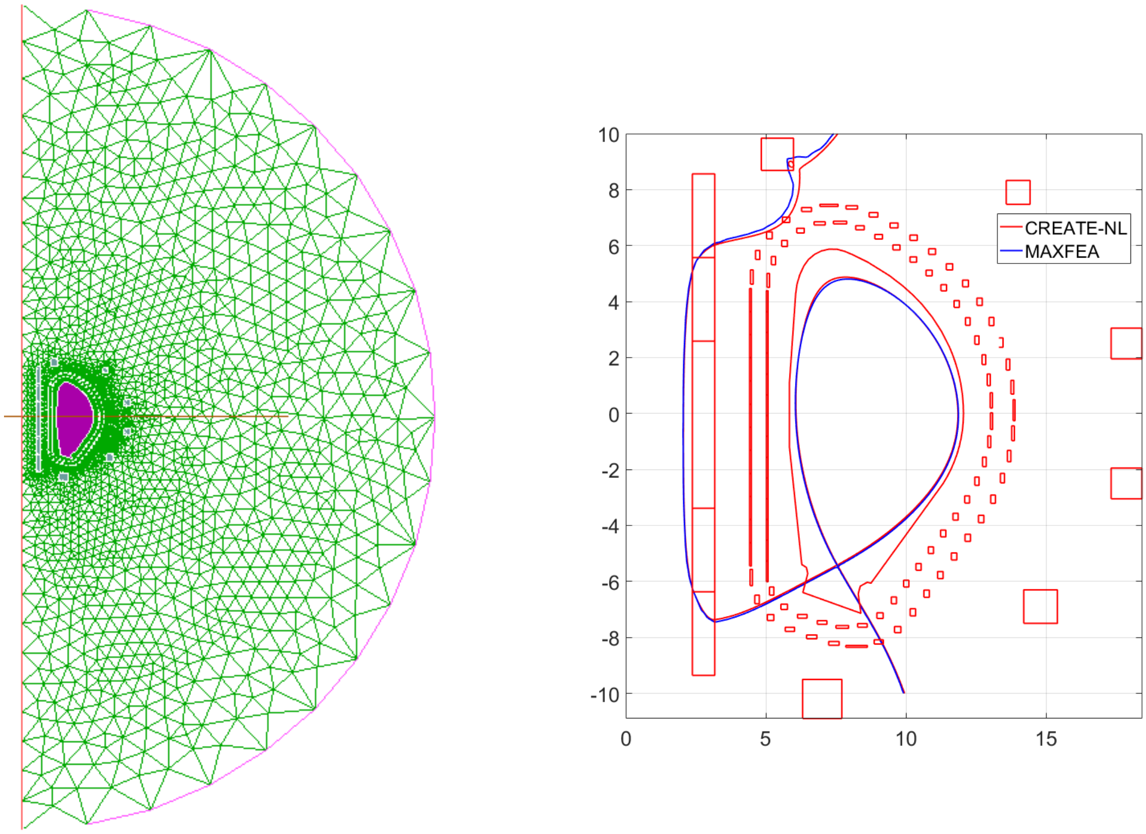

a) b)

Figure 4.1: MAXFEA model a) Overview of the whole FEM domain b) Zoom in the plasma region. The reference SN reproduced by means of MAXFEA is reported in blue, red for the CREATE-NL

Regarding the disruption scenario, a fast Upper Vertical Displacement Event (UVDE) has been considered. The VDE disruption scenario has been modelled as follow:

- Destabilizing kick is imposed @10ms after the start of the simulation to force plasma movement imposing a certain voltage on a dummy coil for few time steps (time step = 1ms);
- Consequently, the plasma starts to move vertically towards the wall, reducing the plasma area, typically with little change in the total plasma current since flux conservation is assumed;
- At a certain point, when the plasma reaches a given critical value of the safety factor (q95 = 2), TQ is imposed as betapol drop in 1 time step and a plasma current spike is found, as regularly observed experimentally, due to the flux conservation and redistribution of the plasma current;

- CQ starts immediately after TQ ($t_{CQ} = 78\ ms$), imposing a proper negative voltage on plasma. During the CQ phase, HC also arises.

4.1.2 APDL 3D Model

The 3D APDL model for the PFV analysis (herein identified as Model PFV) is shown in Figure 4.2 centre. The model consists in a DEMO half sector (11.25°) and features 294 k mesh elements and about 272 k mesh nodes. The adopted element type is the SOLID97, defined by eight nodes, and with up to five degrees of freedom per node. The 3D APDL model for the TFV analysis (herein identified as Model TFV) is shown in Figure 4.2 right. The Model TFV was obtained from the Model PFV, merely changing the material properties and the element degree of freedoms of appropriate set of elements, namely from filaments to the rectangular torus. In other words, the two models are obtainable from the same mesh, circumstance that simplifies the post-processing phase, since the various EM contributions, coming from PFV and TFV, can be merely summed elementwise. Figure 4.2 left shows an overview of the whole FEM domain. The boundary conditions for the PFV analysis are tangent field on the lateral boundaries and the toroidal equivalent currents in the filaments as excitations terms. As far as the Model TFV is concerning, the orthogonal field is applied at the lateral surfaces and equivalent poloidal currents on the rectangular torus as input excitation. For both models, on the external region surface, well far from the magnets, the far field flux condition was considered.

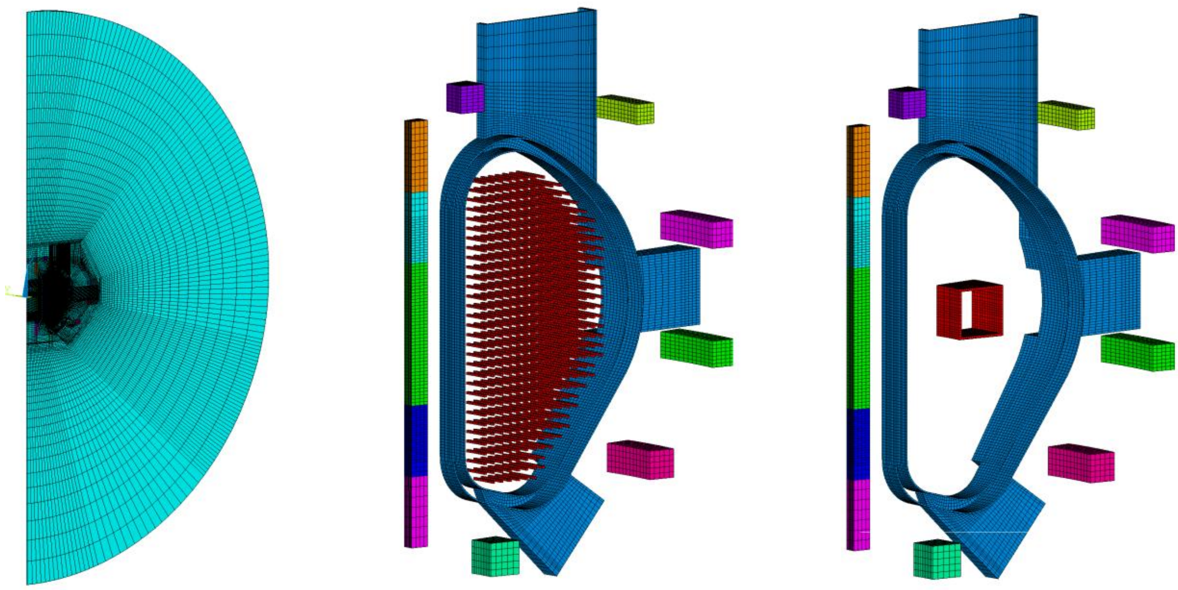

Figure 4.2: Overview of the Model PFV (left) and zooming of the VV structures, PF coils system and the filaments (centre); Model TFV zooming of the VV structures, PF coils system and the rectangular torus (right).

4.2 Results

In this section the results of the transient 2D simulation, of the comparison between MAXFEA and ANSYS APDL and of the 3D analyses are presented.

4.2.1 MAXFEA 2D results

The results of MAXFEA UVDE simulation are reported from Figure 4.3 to Figure 4.6. Regarding the plasma current (named I_{pla} and depicted with blue curve in Figure 4.3), in an initial phase, when plasma is moving upward until it reaches q95 = 2, a small reduction of current is observed because of flux conservation assumption. When the plasma reaches the given critical safety factor value TQ is imposed (takes place at 1.285s, identified with left black vertical line) and a plasma current spike is found, as regularly observed experimentally, due to the flux conservation and redistribution of the plasma current. Immediately after TQ, the CQ begins (CQ ends at 1.367s, identified with right black vertical line). In the CQ phase, HC arises as shown with the red curve and at the end of this phase eddy current in the VV reaches its maximum (yellow curve).

The vertical EM forces (note that the forces are those related to the interaction between toroidal eddy currents and poloidal field, since the 3D effects are not evaluable inside MAXFEA code), acting on the VV are instead reported in Figure 4.4 (I_{pla} is also depicted with red curve). In blue it is represented the global vertical force acting on the VV due to eddy currents, whose peak occurs at about the end of the CQ with a value of about 31.3 MN. After the CQ the force starts to decrease reaching a negative peak of about -11.5MN at 2.236s. This trend is connected with the progressively redistribution of the induced current according with VV geometry and resistivity. In fact, since the VV presents a quite strong up-down asymmetry, after the plasma termination the induced current starts to redistribute with the characteristic τ_{VV} in a such way that the force distribution becomes progressively more vertically unbalanced and, even if the induced global current starts to decrease as consequence of the Joule losses, a force peak is found.

In Figure 4.5 is reported the evolution of the plasma current centroid ($r_c - z_c$) during the UVDE together with the plasma initial equilibrium (blue curve), whilst the plasma TFV flux evolution against time is shown in Figure 4.6.

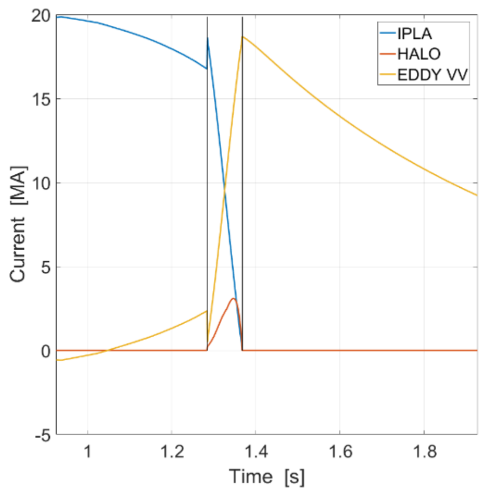

Figure 4.3: MAXFEA plasma current (blue curve), eddy currents (red curve) and halo currents (yellow curve).

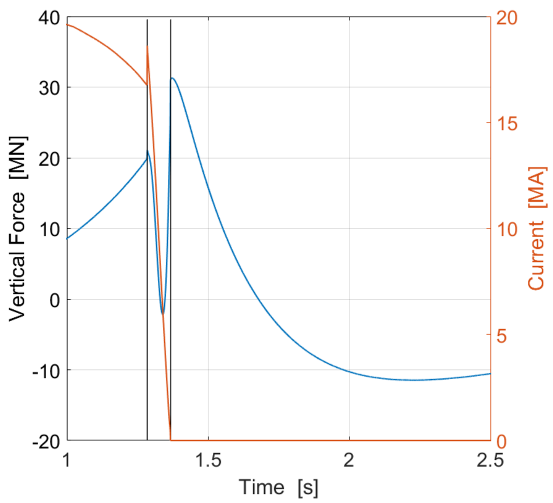

Figure 4.4: MAXFEA Vertical Force on the VV due the eddy currents (blue curve, refers to left ordinate axis) and Plasma current (red curve, refers to the right ordinate axis).

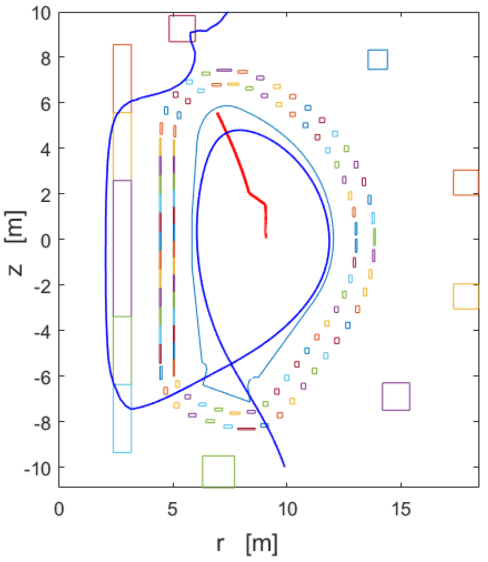

Figure 4.5: Plasma initial equilibrium at DEMO SN @EOF and plasma centroid (rc-zc) movement during the UVDE.

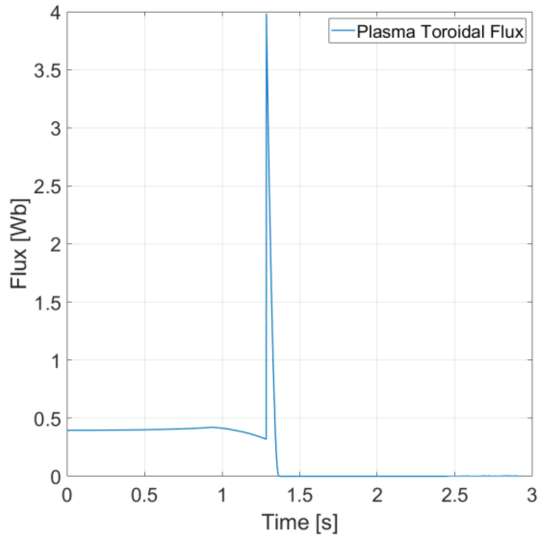

Figure 4.6: Plasma TFV evolution during the UVDE.

4.2.2 Preliminary test: MAXFEA vs AXISYMMETRIC APDL CASE

A preliminary test was considered with the aim to cross-check MAXFEA results with those obtained with ANSYS APDL by means of the proposed procedure. A 3D model considering a simplified axisymmetric VV (herein identified as Model TEST) has been obtained from Model PFV merely changing the material properties and the element degree of freedoms of appropriate set of elements (see Figure 4.7). This means that, in this Model TEST, current cannot be inducted on the VV ports during the UVDE.

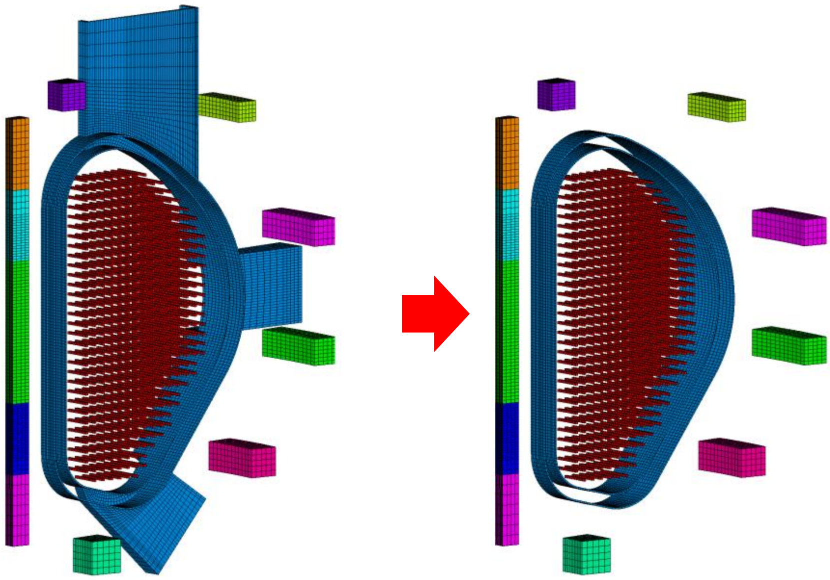

Figure 4.7: Model PFV (left) and Model TEST (right), obtained from Model PFV merely changing the material properties and the element degree of freedoms.

As it can be observed in Figure 4.8, an almost perfect agreement was found between MAXFEA and APDL Model TEST analysis, in terms of total induced eddy current on the VV, and also in terms of total vertical force (360°) on VV, as shown in Figure 4.9. Is also possible observe that the set of filaments conserves the plasma current evolution (MAXFEA plasma current and the equivalent current in the filaments are almost overlapped, represented with blue solid and red dashed lines of Figure 4.8 respectively).

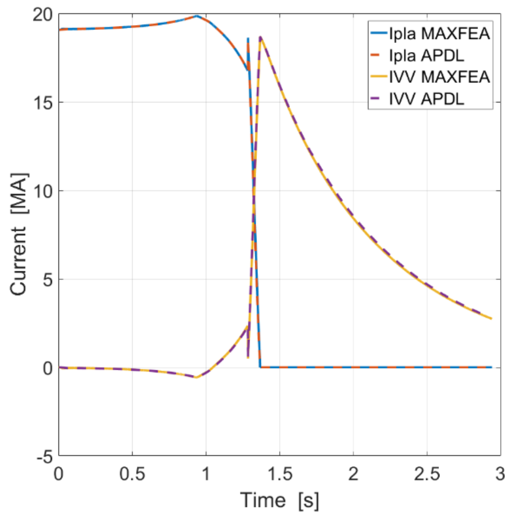

Figure 4.8: Currents MAXFEA vs APDL Model TEST

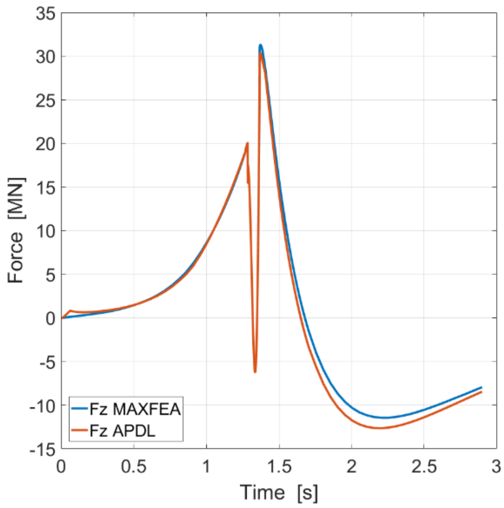

Figure 4.9: Vertical Force over 360° MAXFEA vs APDL Model TEST

The results show that there is a good agreement between the two codes, thus verifying the quality and the robustness of the 3D models (Model PFV, Model TFV and Model TEST share the same mesh) and the correctness of the proposed procedure. In Figure 4.10 and Figure 4.11 the current density and force density distributions in the VV at the time CQ ends (when the vertical force is at its peak, about 31.3 MN) are shown.

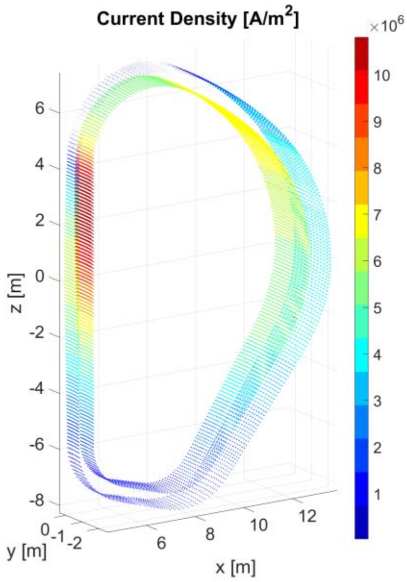

Figure 4.10: Model TEST: current density distribution at the end of the CQ.

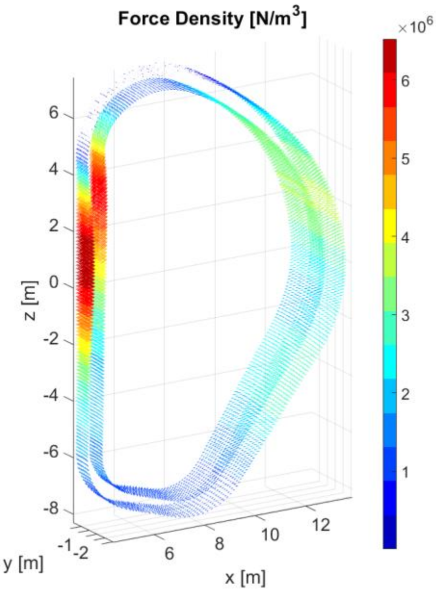

Figure 4.11: Model TEST: force density distribution at the end of the CQ.

4.2.3 Full 3D analysis: Model PFV and Model TFV

All the quantities that refer to the VV complete sector (22.5°) were obtained in the post-processing phase with a proper data manipulation exploiting the existing symmetries and are expressed with respect to the cartesian reference system shown in Figure 4.12. A comparison in terms of induced currents and vertical force between Model TEST and the full 3D analysis (Model PFV + Model TFV) is shown in Figure 4.13 and Figure 4.14. The current density and force density distributions on the VV at the end of CQ are shown instead in Figure 4.15 and Figure 4.16, respectively. All the results shown hereafter include all the EM contributions, in terms of currents (i.e. J_{PFV} and J_{TFV}) and fields (i.e. B_{pol} and B_{tor}). In particular, the toroidal field has been calculated resorting to the analytic formulation $B_{tor} = A/r$, in which $A = B_T \cdot R = 47.54\, T \cdot m$, where $R = 9\, m$ and $B_T = 5\, T$. The results highlight that the presence of the 3D structures (i.e. ports) does not strongly affected the VV response in terms of total induced eddy current, that presents a peak of about 18.7 MA at the end of the CQ, as shown in Figure 4.13. Conversely, the presence of the ports produces not negligible effects on the total vertical force (360°) after the time CQ ends, as shown in Figure 4.14, whilst the peak occurring at end of the CQ remains approximately the same (about 31.3 MN). As discussed in Section 4.2.1, after the plasma termination the induced current starts to redistribute with the characteristic τ_{VV} in a such way that the force distribution becomes progressively more vertically unbalanced and, even if the induced global current starts to decrease as consequence of the Joule losses, a negative force peak is found. This trend is found to be more pronounced if 3D effects are included. Furthermore, if the VV ports are considered, a non-trivial distributions of induced currents and forces arise, generating local concentrations as shown in Figure 4.15 and Figure 4.16 respectively. Both distributions are related to the end of CQ instant of plasma evolution. From force density point of view, it is possible to observe a local concentration of forces around the upper port that is an order magnitude greater than those extrapolated with Model TEST (see Figure 4.16). In this zone, in fact, the eddy currents have to distribute around the port determining current concentrations. In particular, at the port sides the eddy current coming from PFV develops a predominant poloidal component that interacts with external toroidal field generating a torque. Finally, in Figure 4.17 and in Figure 4.18, the resultant forces along x and y directions on the VV over a sector (22.5° of angular amplitude) are shown. As it is possible to observe, the force along x direction experiences a peak value of about -19MN. Furthermore, a net force along y direction (cartesian reference system) is also observed, which is not predictable by the axisymmetric analyses (MAXFEA - Model TEST). Indeed, this net force is mainly due to poloidal currents paths coming from the PFV and related to the presence of the ports via interaction with the toroidal magnetic field.

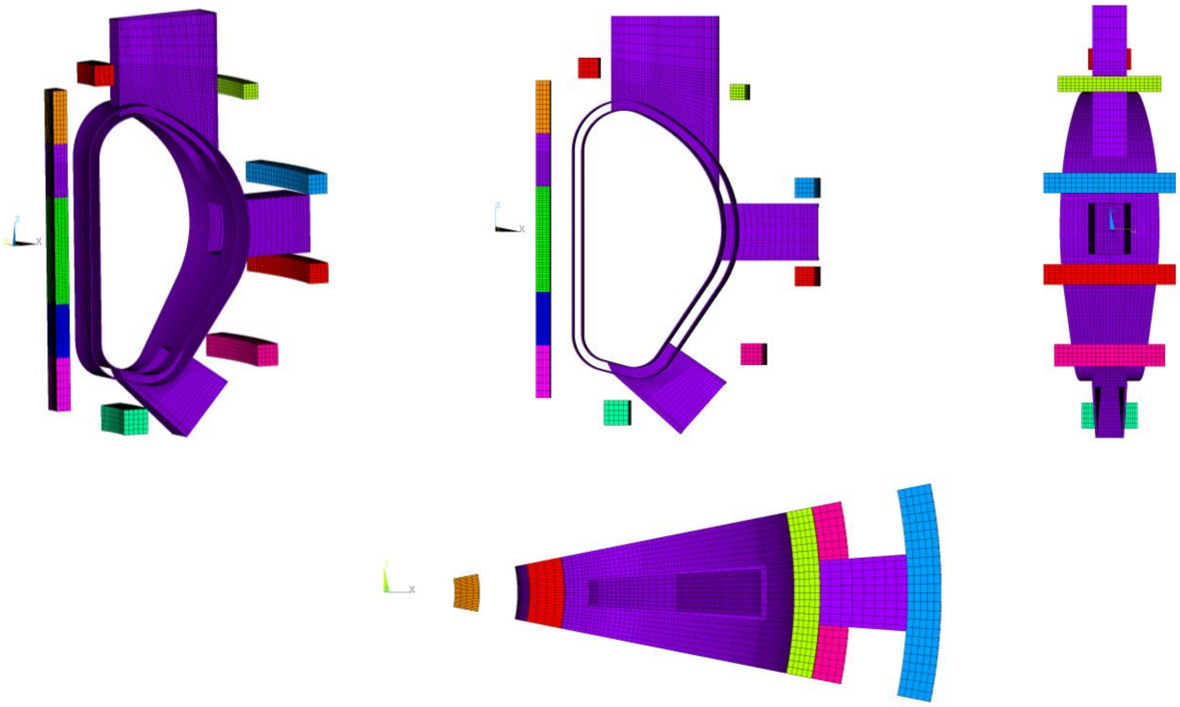

Figure 4.12: Different views of the VV complete sector (22.5°) and reference coordinate system.

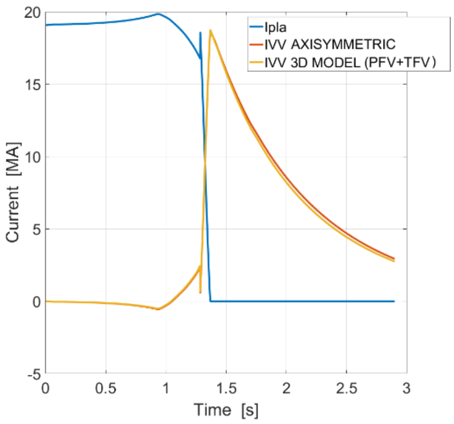

Figure 4.13: Currents MODEL TEST vs FULL 3D ANALYSIS (MODEL PFV + MODEL TFV).

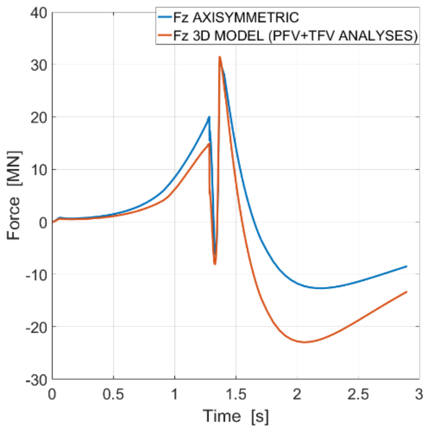

Figure 4.14: Vertical Force 360° MODEL TEST vs FULL 3D ANALYSIS (MODEL PFV + MODEL TFV).

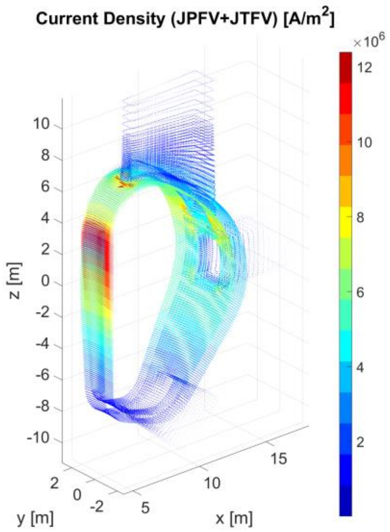

Figure 4.15: Full 3D analysis: current density force distributions at the end of the CQ.

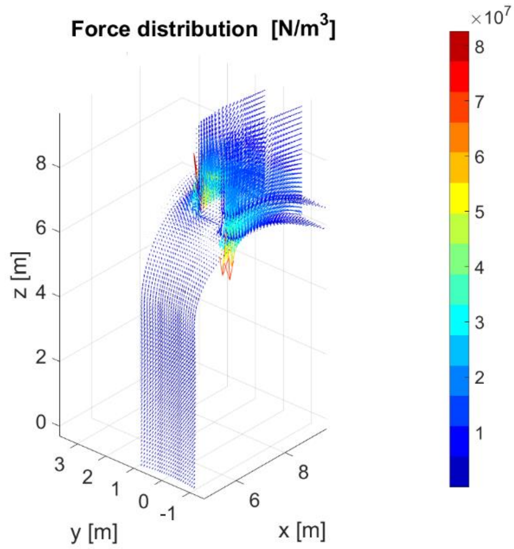

Figure 4.16: Full 3D analysis: force distribution in the upper port inboard at the end of the CQ (right).

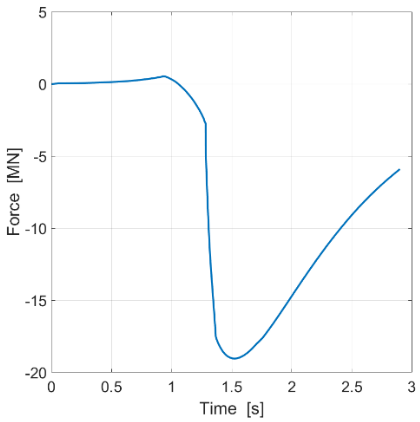

Figure 4.17: Force resultant on the VV along x direction over a sector (22.5°) (MODEL PFV + MODEL TFV).

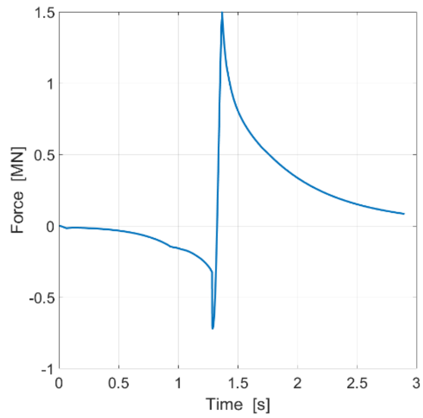

Figure 4.18: Force resultant on the VV along y direction over a sector (22.5°) (MODEL PFV + MODEL TFV).

4.3 Conclusions

In this Section, the application of the proposed Methodology to DEMO was presented. In particular, DEMO PMI SN magnetic configuration was reproduced considering a simplified geometry (i.e. VV and ports, BB and Divertors are not included in the model) and a fast UVDE was chosen as disruption scenario.

At first, an almost perfect agreement was found between MAXFEA and APDL considering an axisymmetric 3D VV, both in terms of currents and vertical force, thus verifying the 3D model. Then, the procedure was applied to DEMO VV including the presence of the 3D geometries (i.e. ports). Results highlight the presence of a non-trivial distributions of currents and forces, with local concentration. Despite the higher level of complexity needed to perform a detailed 3D analysis, the concentrations are too relevant to be neglected. Indeed, it is possible to observe a local concentration of forces at the inner board of the upper port at the time CQ ends that is an order magnitude greater than those extrapolated with axisymmetric analyses (MAXFEA – Model TEST). In this zone, the interaction of the eddy currents with external toroidal field generates also a torque, not predictable with MAXFEA and Model TEST. The results also highlight that the presence of the 3D structures does not strongly affected the VV response in terms of total induced eddy current, that shows a peak of about 18.8 MA. Conversely, the presence of the ports produce not negligible effects on the total vertical force (360°) after the time CQ ends, whilst the peak occurring at the end of the CQ is approximately the same (about 31.3 MN).

This study was the testbed for the development of this methodology. Once validated, its reliability has been recognized in EUROfusion and the proposed procedure has been included as part of the DEMO FW protection integrated design strategy [72], to be used in future studies in this context.

The studies herein presented have been reported in the following journal publications [69], [72] and [73].

5 DTT

Amongst all the different physics and technological areas where DEMO requires significant progress compared to ITER, the area of power exhaust plays a crucial role since predictive capability of present-day models is low and this area is expected to play a major role in limiting DEMO designs due to the much larger value of P_{tot}/R in DEMO than in present-day devices and even in ITER [9]. In fact, since it is expected that the limits to divertor target heat flux in DEMO might be even lower than those foreseen for ITER due to the high neutron fluence (a limit as low as $5MWm^{-2}$ has been postulated for DEMO), and the fusion power will be substantially higher at only slightly larger major radius, the exhaust problem in DEMO will be significantly more challenging than in ITER. Since the extrapolation from the present devices (largely the medium-sized tokamaks) to DEMO based on modelling alone is considered too large, the possibility to design a dedicated Divertor Tokamak Test facility (DTT) has been proposed within the EUROfusion road map [6]. Aim of DTT is to access a set of possible alternative solutions for DEMO, including the test of advanced magnetic configurations and liquid metal divertors. In 2015, a team of international experts has demonstrated the possibility to realize a flexible and effective facility able to bridge the power exhausts gaps between ITER and DEMO (The DTT proposal [11]). Since then, the DTT project has moved on. Presently, the conceptual design phase approaches its conclusion (DTT Interim Design Report [12]) and the engineering phase is started. Different overview papers have been published in the last few years to describe the status of the DTT project [13]–[15], with the more recent update given in [16]. Nowadays, the project is managed by a DTT legal entity mainly composed by ENEA and ENI and with the participation of important Italian research centres and universities, including Tuscia University [17].

Within DTT project framework, in the recent past the candidate was directly involved in preliminary multiphysical studies aimed to support the conceptual design of the DTT VV, that led to a journal publication [75]. In particular, structural analyses were conducted considering the EM loads from fast upper and lower VDEs simulated by means of MAXFEA.

Since then, the design of the DTT Vacuum Vessel and Ports (VVP) has moved on and it is currently in the final design stage. Therefore, the necessity to analyse in detail the behaviour of this component under the EM loads coming from plasma disruptions has emerged in order to verify the design or drive further modifications in the iterative design process. In this context, a study to analyse the mechanical and electro-magnetic behaviour of the DTT VVP has been carried out considering different types of plasma up-ward and down-ward VDEs, exploring different duration of the CQ (fast events CQ 4ms, slow events CQ 40ms). To perform this analysis, the proposed methodology based on the use of MAXFEA code in combination with ANSYS APSL has been successfully applied. From this study, it has emerged that the VVP mechanical response is acceptable in all of the scenarios but, during a particular event, namely the DVDE slow scenario, a stress concentration in correspondence of the connection of the pedestal with the VV outer shell has emerged. As a consequence, mechanical reinforcement in this region has been introduced in order to obtain an optimal design of the VVP.

Here, the EM and mechanical response of the DTT VVP during this DVDE slow event is presented. The aim of this Section is to show the successful application of this novel procedure in the context of the DTT project and its reliability and capability to support the final stage design of these kind of components.
The study herein reported is the subject of the journal publication recently submitted to *Fusion Engineering and Design* and currently in the final stage of the review process [76].

5.1 Methodology

In this study, the proposed methodology is applied to study a DVDE scenario with a CQ duration of 40ms. All the EM contributions are computed and then applied to the structural model. As shown later in the next sections, it was analysed also a case in which a Toroidal Peaking Factor (TPF) is considered in the HC distribution. In particular, the TPF was introduced applying the following sinusoidal function to the force distribution related to the HC:

$$F_{\text{HC-}TPF} = F_{\text{HC}}\ (1 + \sin\theta)$$

where $0 \leq \theta \leq \pi$ is the toroidal angle. As consequence, in this case the EM halo forces are zero for $\theta = 0$ and assume twice the nominal value for $\theta = \pi$.
The 3D structural model has to be realized with different features with respect to a 3D EM simulation, implying dissimilar mesh models. Hence, the loads coming from EM simulations, in terms of force densities, have to be interpolated on the mechanical mesh model.
During the CQ phase of the DVDE slow scenario, a vertical force peak was observed as the result of a combination of both eddy and halo currents. The VVP structural response is studied at this critical time instant.

5.2 FE models

The DTT VV consists of two stainless steel (SS) shells of 15 mm thick each, separated by several toroidal and poloidal ribs. Each VV sector is 20° wider in toroidal direction and feature 5 ports. In only 6 out of 18 sectors the lower port is replaced by the VV pedestal (located every 60°). The considered in-vessel components are: a preliminary design of the divertor cassette and its supports (i.e. inner and outer rails), and stabilizing plates with supports, that feature a toroidal continuity.

5.2.1 EM models

5.2.1.1 MAXFEA 2D axisymmetric model

In this section the MAXFEA model is exposed. The developed model, whose overview is given in Figure 5.1, includes:

- CS and PF coils
- The Vacuum Vessel (dark red areas in Figure 5.1b)
- The stabilizing plates (dark blue areas in Figure 5.1b)

In order to take into account the presence the VV ports, the resistivity of these components has been opportunely scaled with the ratio vacuum/filled in toroidal direction. Instead, the divertor system is not included in the model since its effect on the plasma evolution can be neglected. In fact, as shown in more in details later on, the divertor cassettes are segmented in the toroidal direction and insulated from each other so that no net toroidal current can arise.

The reference equilibrium reproduced with MAXFEA is shown in Figure 5.1b, together with that computed by means of the CREATE-NL code [74], showing a very good agreement between the two codes.

The DVDE slow scenario has been modelled as follow:

- Destabilizing kick is imposed @10 ms after the start of the simulation to force plasma movement imposing a small voltage on a dummy coil for few time steps (1ms);
- Consequently, the plasma starts to move vertically towards the wall, reducing the plasma area, typically with little change in the total plasma current since flux conservation is assumed.
- At a certain point, when the plasma reaches a given critical value of the safety factor (q95 = 2), TQ is imposed as betapol drop in 1 time step and a plasma current spike is found, as regularly observed experimentally, due to the flux conservation and redistribution of the plasma current.
- CQ starts immediately after (40ms), imposing a proper negative voltage on plasma. During the CQ phase, HC growth is considered.

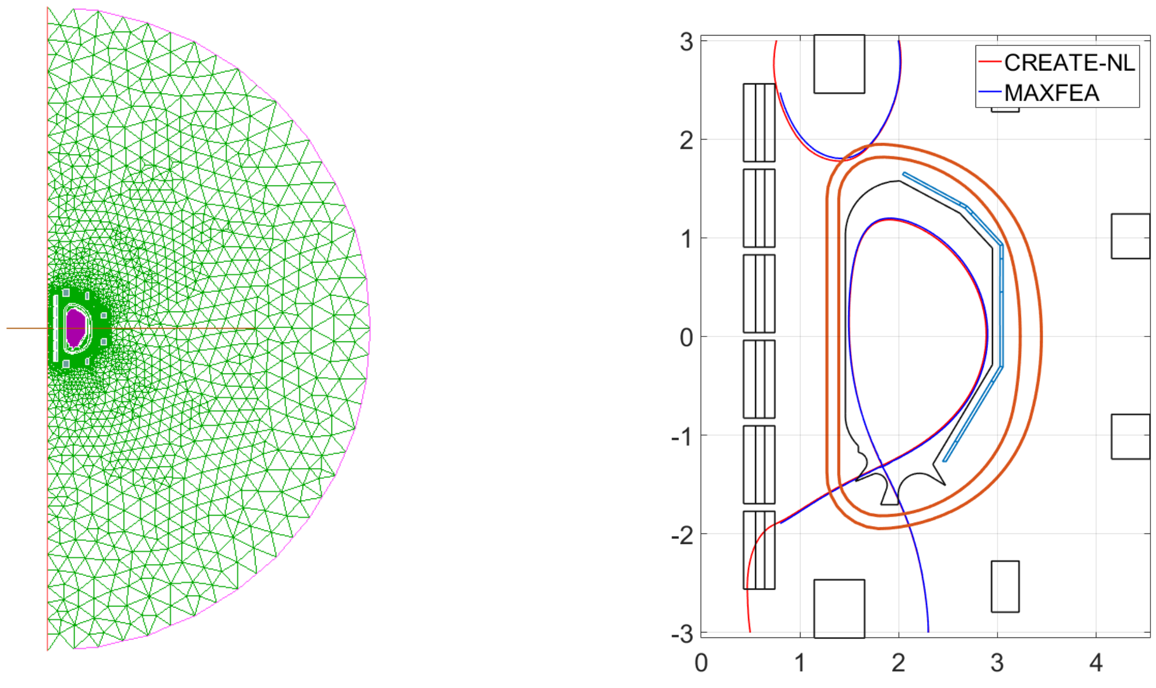

a) b)

Figure 5.1: MAXFEA model a) Overview of the whole FEM domain b) Zoom in the plasma region. The VV and the stabilizing plate are represented in dark red and dark blue, respectively. The reference SN reproduced by means of MAXFEA is reported in blue, red for the CREATE-NL

5.2.1.2 APDL 3D EM Model

The 3D EM model requires some preliminary simplification in order to reduce the complexity of the whole model. In fact, as discussed, the differential formulation of the FE analysis needs to also model the vacuum. For this reason, to facilitate mesh operations, in the development EM model all the fillets were replaced with sharp edges. Another simplification is to neglect the presence of the poloidal ribs, since their presence does not affect the result significantly. Also the VV pedestal was neglected in the model, being insulated from VV outer shell. The divertor was represented in a simplified way and its cassette and the stabilizing plates considered connected to the VV inner shell through their relative supports (see Figure 5.3). The periodicity of the system allows to consider only one sector and a half. In the post processing phase the current and force distributions were then extrapolated over three sectors, being this the minimum amplitude for mechanical cyclic symmetry (due to the presence of VV pedestal every 60°).

The EM model is composed of 983k nodes and 727k SOLID97 elements. The same mesh model is adopted for PFV, TFV and HC simulations. In the first case the plasma PFV is introduced through a set of filaments (see Figure 5.2 center), whilst in the second a torus is adopted to apply the plasma TFV (see Figure 5.2 right). Regarding the HC simulations, the total HC computed with the MAXFEA simulation is injected into the structures through chosen in and out locations. The assumption of the in and out locations will be presented in Section xx. Figure 5.2 left shows the whole FEM domain.

In Figure 5.3, from left to the right, an overview of the toroidal ribs (depicted in green), of the stabilizing plates and support (depicted in cyan and grey respectively) and of divertor cassettes and supports (depicted in blue and orange respectively) is provided.

In the results shown in the following sections, the contribute of toroidal magnetic field is included in a simplified way, namely considering the analytic formulation $B_{tor} = A/r$, in which $A = B_T \cdot R = 13.14\ T \cdot m$, where $R = 2.19\ m$ and $B_T = 6\ T$ [16].

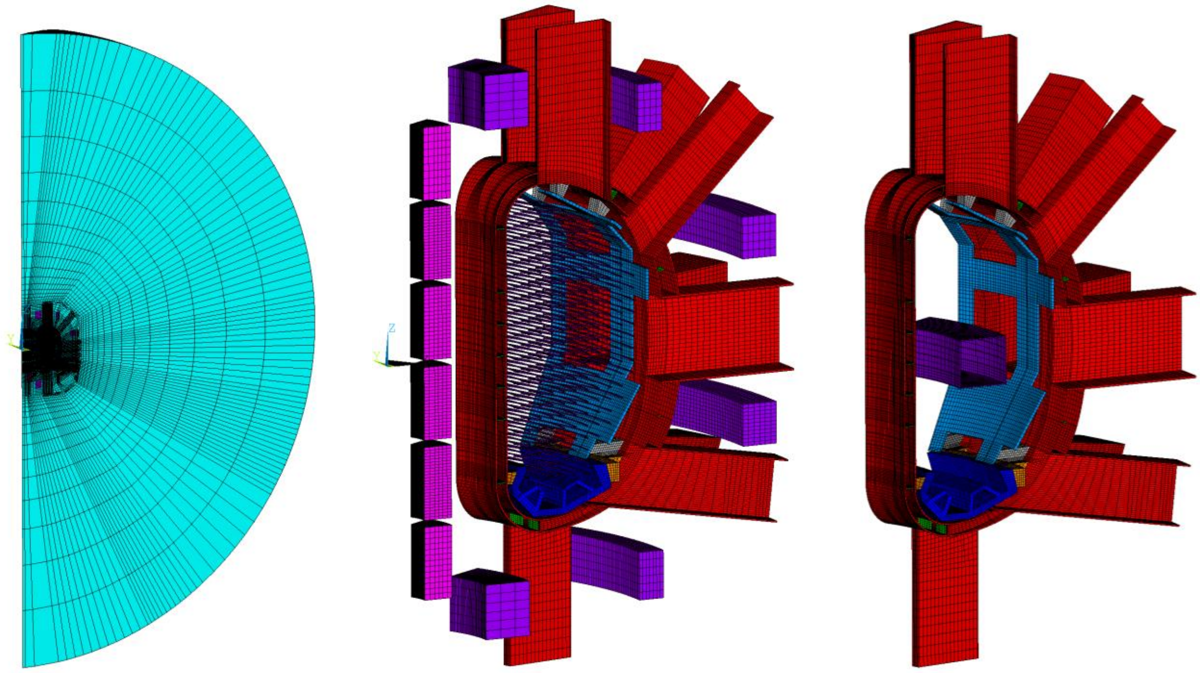

Figure 5.2:3D APDL EM model: overview of the whole model with region (left), mesh with filaments for PFV analysis (center) and mesh with torus for TFV analysis (right)

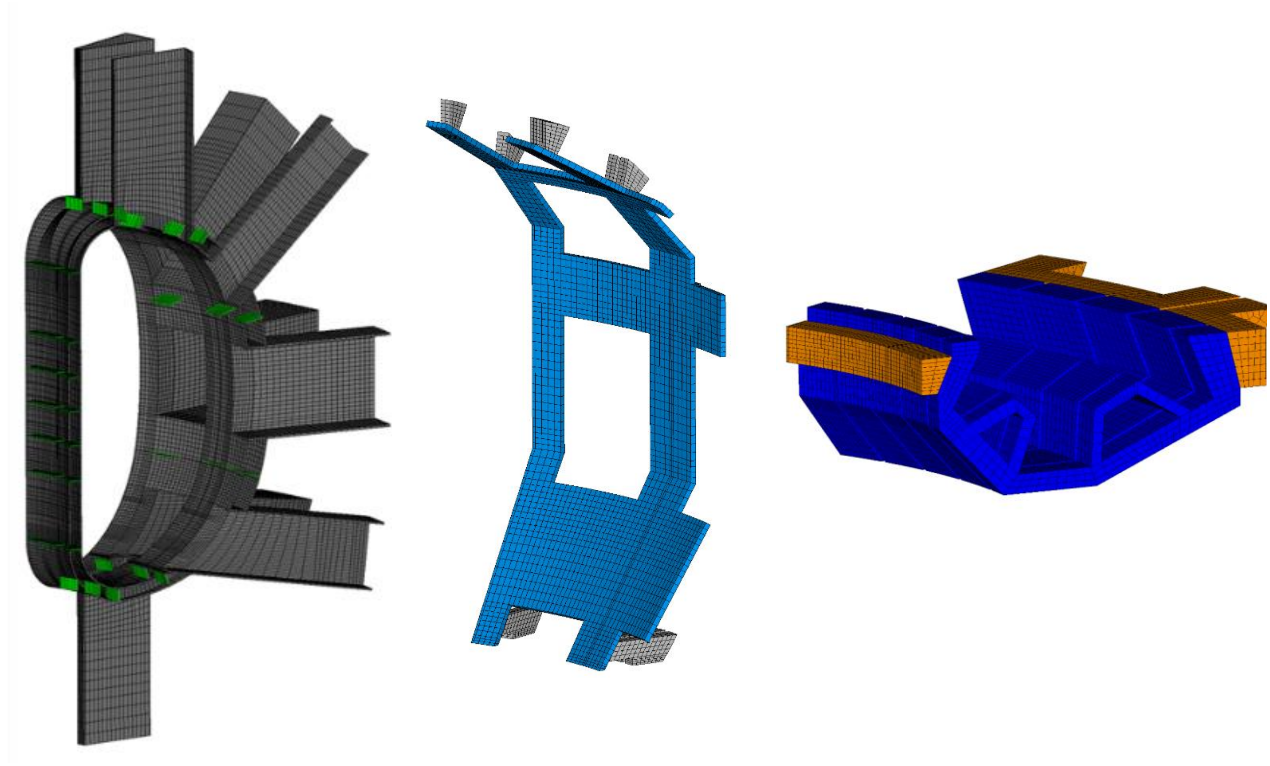

Figure 5.3: 3D APDL EM model mesh details: toroidal ribs depicted in green (left), stabilizing plates and support, depicted in cyan and grey respectively (center), divertor cassettes and supports depicted in blu and orange respectively (right)

5.2.2 Structural Models

5.2.2.1 3 sectors (60°)

The structural model, is composed by 3 sectors (i.e. 60°), that is the minimum amplitude for the cyclic symmetry when TPF is not considered. In the central sector the port 5 is replaced by the gravity support. Compared to the EM model, in the structural one all the fillets have been included, as can be seen in Figure 5.4 (left). Moreover, also the poloidal ribs have been modelled, in addition to the toroidal ones, as shown in Figure 5.4 (right). However, in this case the divertor and the stabilizing plates have not been included in the model, but their contribution was considered only in terms of resultant forces and moments.
The mesh model consists of 1333k nodes and 1490k elements, composed of SOLID185 bricks and contact elements (CONTA174 and TARGE170). The cyclic symmetry was applied through a set of constraint equations. The VV gravity support is fixed at the bottom and connected to VV outer shell through contact elements. The port bellows are considered free to slide along their axis, whilst the movement in the other two directions is prevented. The EM loads acting on the structure are interpolated from the EM models and applied as body force densities on the VVP. The resultant forces and moments on the divertor and the stabilizing plates were applied to a master node, located at the center of the tokamak, and linked to the support structures via RBE3 elements.

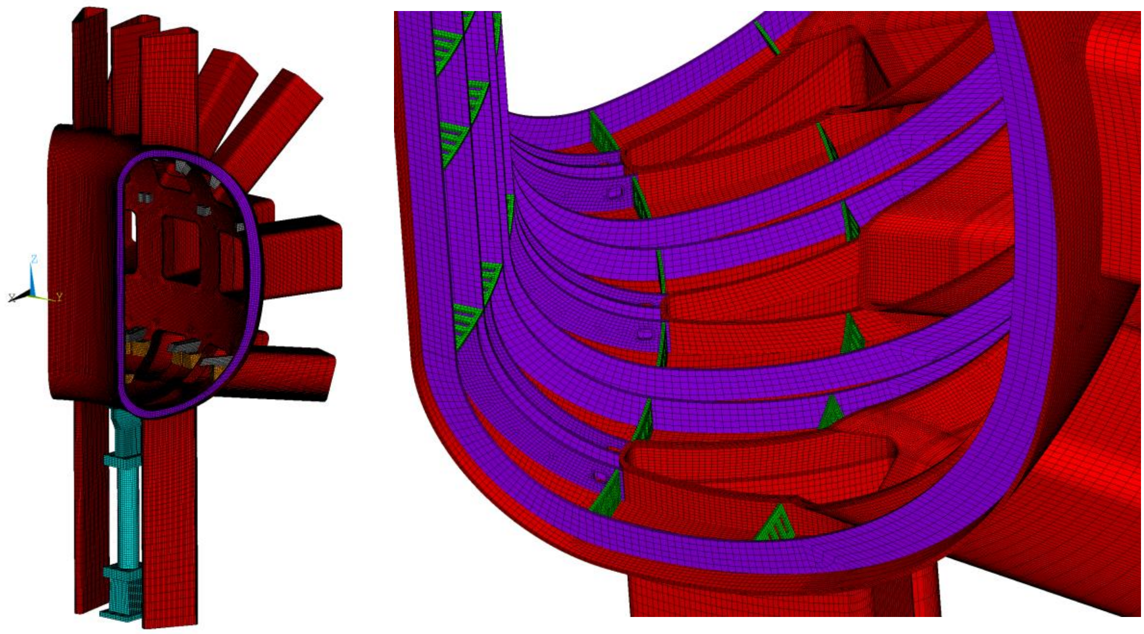

Figure 5.4: 3D APDL 60° structural model: global mesh (left) and overview of the bottom part of the vessel in which the inner shell is hidden to show the toroidal and poloidal ribs, depicted in green and purple respectively (right)

5.2.2.2 18 sectors (360°)

If the TPF is introduced in the halo currents force distribution, the cyclic symmetry condition used in the 60° model shall no longer be valid. When the TPF is equal to 2 it is necessary to use a full 360° model. In Figure 5.5 the full model is shown together with a detail of the mesh, obtained from 60° model with 6 toroidal repetitions. The mesh consists of approximately 8000k nodes and 900k elements.

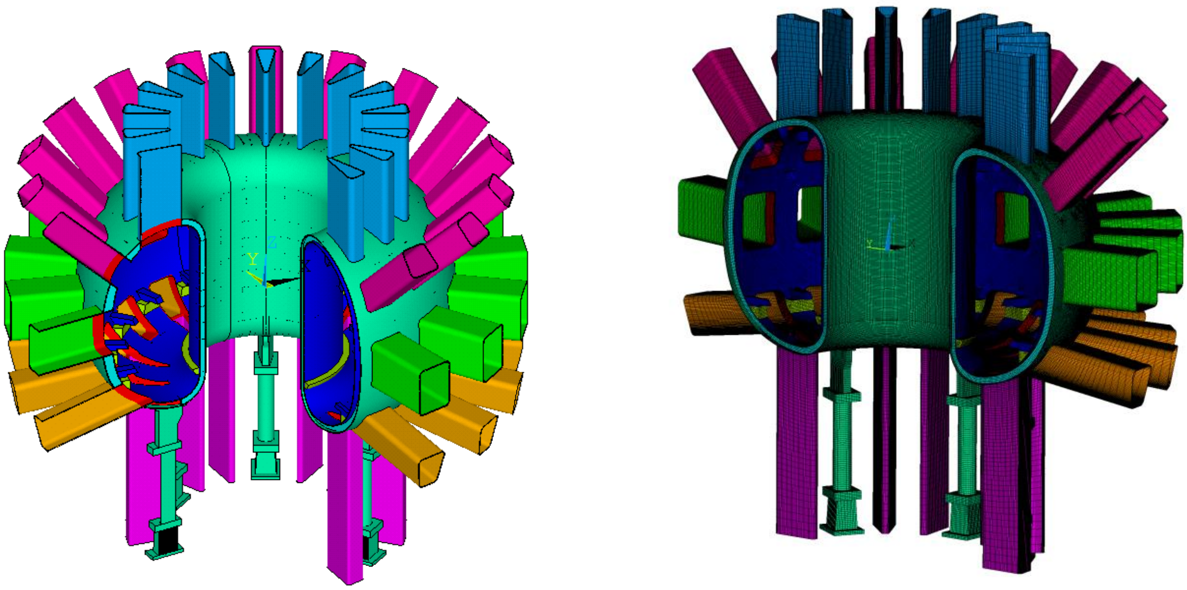

Figure 5.5: APDL 360° mesh model overview (half model).

5.3 Results

The results of the EM and Structural analyses are exposed in Section 5.3.1 and 5.3.2, respectively. Section 5.3.1.1 reports the results of the MAXFEA analysis, while Section 5.3.1.3 presents the full 3D EM analysis (PFV+TFV+HC). In Section 5.3.1.2, the 3D EM model validation is discussed. From the mechanical point of view, the time instant in which a vertical force peak has been observed as the result of the combination of eddy and halo currents is considered (herein named eddy+halo instant) (Section 5.3.2.1). Moreover, also the impact of a TPF equal to 2 has been analyzed at the same time instant (Section 5.3.2.2).

5.3.1 EM analysis

In the following sections, the results of the MAXFEA 2D analysis, of the comparison between MAXFEA and ANSYS APDL and of the full 3D analyses are exposed.

5.3.1.1 MAXFEA analysis

The results of the MAXFEA DVDE slow simulation are reported from Figure 5.6 to Figure 5.9. Regarding the plasma current (named I_{pla} and depicted with blue curve in Figure 5.6), in an initial phase, when plasma is moving downward until it reaches q95 = 2, a small reduction of current is observed because of flux conservation assumption. When the plasma reaches the given critical safety factor value, TQ is imposed (takes place at 0.112s, identified with left black vertical line) and a plasma current spike is found, as regularly observed experimentally, due to the flux conservation and redistribution of the plasma current. Immediately after TQ, the CQ begins (CQ ends at 0.152s, identified with right black vertical line). In the CQ phase, HC arises as shown with the red curve, reaching a peak of about 2.3MA. Nearly the end of this phase, at 0.143s, eddy current reaches its maximum of about 3.7MA (yellow curve).

The vertical EM forces acting on the VV are instead reported in Figure 5.7 (I_{pla} is also depicted with purple curve). In blue it is represented the global vertical force acting on the VV due to eddy currents, whose peak occurs at about the end of the CQ with a value of about -8 MN. Instead, in red it is reported the global vertical force due to the halo current, whose peak of about -7.4MN occurs 0.127s, when HC is at its maximum. Yellow curve shows the total eddy + halo force, highlighting a peak of about -10.6MN at 0.137s. Note that the forces connected with the eddy currents are those related to the interaction between toroidal induced currents and poloidal field, since the 3D effects are not evaluable inside MAXFEA code.

In Figure 5.8 the evolution of the plasma current centroid (r_c - z_c) during the UVDE together with the plasma initial equilibrium (blue curve) is reported, whilst the plasma TFV flux evolution against time is shown in Figure 5.9.

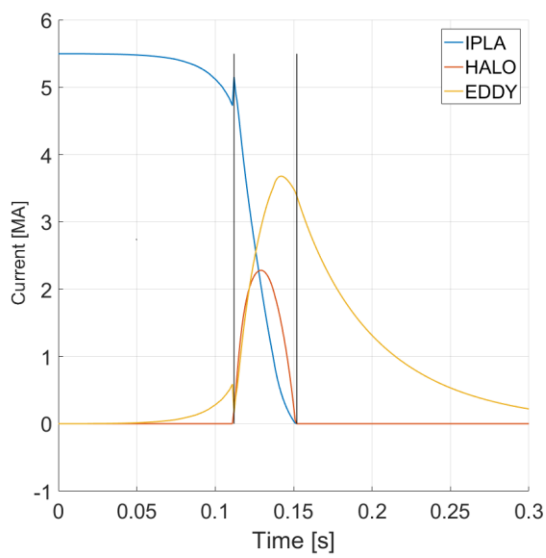

Figure 5.6: MAXFEA plasma current (blue curve), eddy currents (yellow curve) and halo currents (red curve).

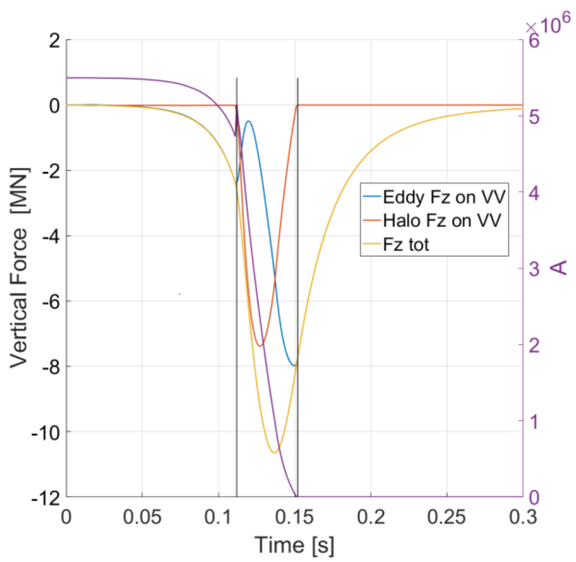

Figure 5.7: MAXFEA Vertical Force on the VV due the eddy currents (blue curve, refers to left ordinate axis), due to the halo currents (red curve, refers to left ordinate axis), due to eddy+halo (yellow curve, refers to left ordinate axis) and Plasma current (purple curve, refers to the right ordinate axis).

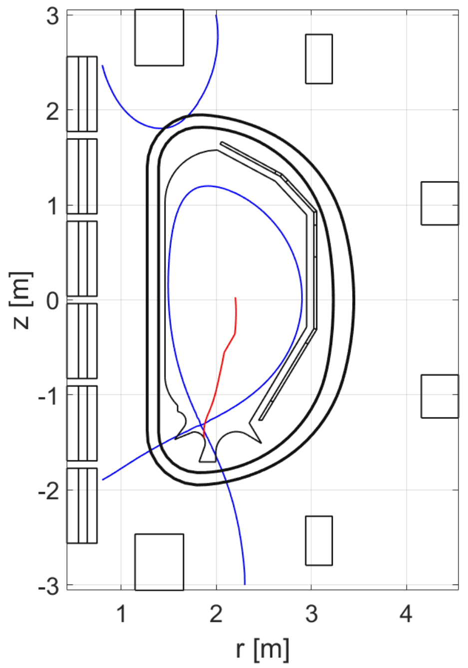

Figure 5.8: Plasma initial equilibrium (SN @SOF) and plasma centroid (rc-zc) movement during the DVDE slow.

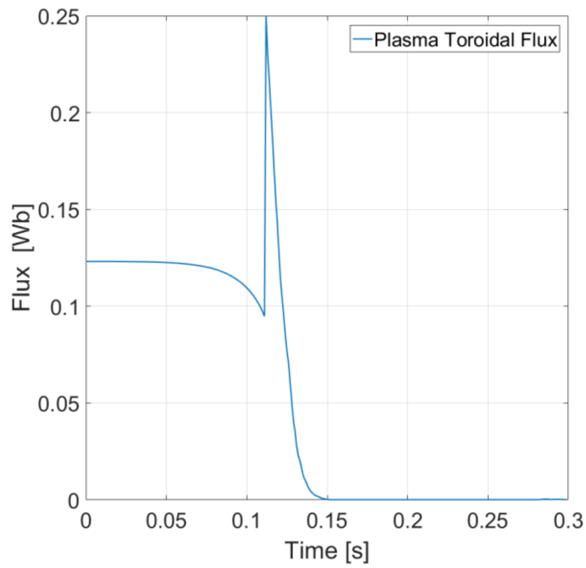

Figure 5.9: Plasma TFV evolution during the UVDE.

5.3.1.2 3D model validation with simplified axisymmetric test-case: MAXFEA vs APDL

A preliminary test has been carried out with the aim to validate the APDL 3D Model against MAXFEA. To this end, a simplified 10° axisymmetric model (herein identified as Model TEST) has been obtained from the 3D Model (PFV, TFV and HC analyses share the same mesh) merely changing the material properties and the element degrees of freedom of appropriate set of elements in order to reproduce the same geometry of the MAXFEA analysis (Figure 5.10). Furthermore, a MAXFEA simplified simulation (herein identified as MAXFEA TESTCASE) has been performed simply considering the reference resistivity of the SS for the structures in order to obtain the same conditions between MAXFEA and APDL also in terms of material properties. The equivalent resistivities previously discussed to take into account the toroidal discontinuities of the components are not considered in this test case, thus a slightly different plasma evolution with respect of what reported in Section 5.3.1.1 is obtained.

The results are shown in Figure 5.11 and Figure 5.12. As it can be observed in Figure 5.11, an almost perfect agreement was found between MAXFEA TESTCASE and APDL Model TEST, in terms of total eddy current in the VV and in the Stabilizing Plate, and also in terms of total vertical force (360°) on these components, as shown in Figure 5.12. From Figure 5.11 it is also possible to observe that the set of filaments conserves the plasma current evolution (MAXFEA plasma current and the equivalent current in the filaments are almost overlapped, represented with blue solid and red dashed lines, respectively). The results show that there is a very good agreement between the two codes, thus verifying the APDL 3D model.

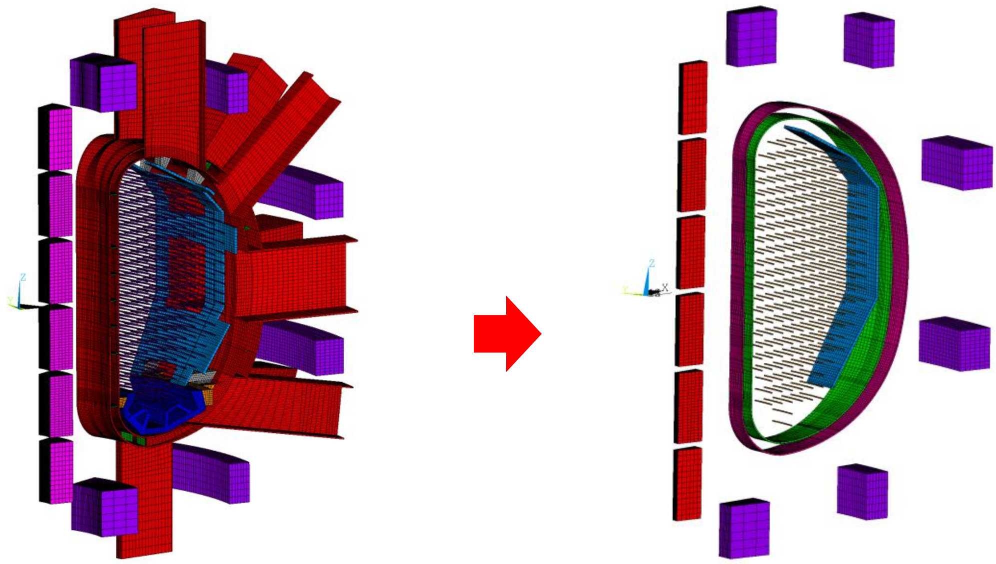

Figure 5.10: 3D Model with filaments for PFV analysis (left) and Model Test (right), obtained from the 3D Model merely changing the material properties and the element degrees of freedom of specified set of elements.

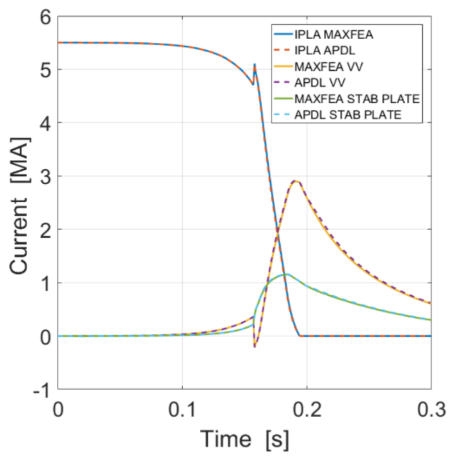

Figure 5.11: Currents MAXFEA TESTCASE vs APDL Model TEST

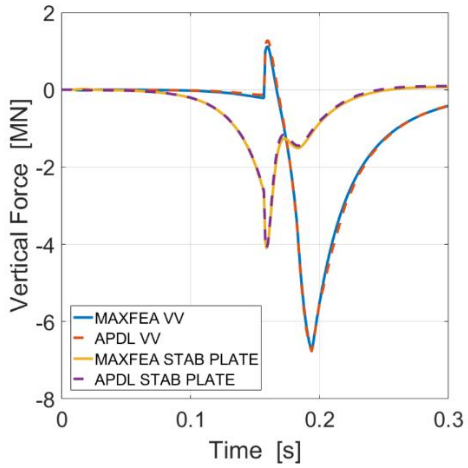

Figure 5.12: Vertical Force due to eddy currents over 360°: MAXFEA TESTCASE vs APDL Model TEST

5.3.1.3 Full 3D Analysis: PFV + TFV + HC

Starting from the MAXFEA simulation shown in Section 5.3.1.1, a full 3D EM analysis has been performed introducing the plasma evolution in the 3D Model with the techniques exposed in Section 3. A comparison in terms of induced currents and vertical forces between MAXFEA 2D simulation and the full 3D analysis (PFV+TFV+HC) is shown in Figure 5.13 and Figure 5.14. The results highlight that the presence of 3D effects does not strongly affect the structures response in terms of global quantities (i.e. total currents and forces). A force peak of about -10MN is observed at 0.140s (eddy+halo instant) looking at the red curve in Figure 5.14. On the other hand, the presence of the ports, of local electrical connections and so on, produces non-trivial and non-negligible forces concentrations, with the appearance of local moments and torques on the components. Figure 5.15 shows some eddy currents paths (PFV+TFV) on the components near the end of CQ, at 0.143s, when the eddy current is at its maximum. Instead, Figure 5.16 shows the force density distribution due to the eddy currents in all the components at the same time instant.

As far as the HC is concerning, Figure 5.17 shows the current density in a divertor cassette at the peak of the HC, at 0.129s, while Figure 5.18 presents the force density at the same time instant. Figure 5.17 shows also the assumed in and out HC locations.

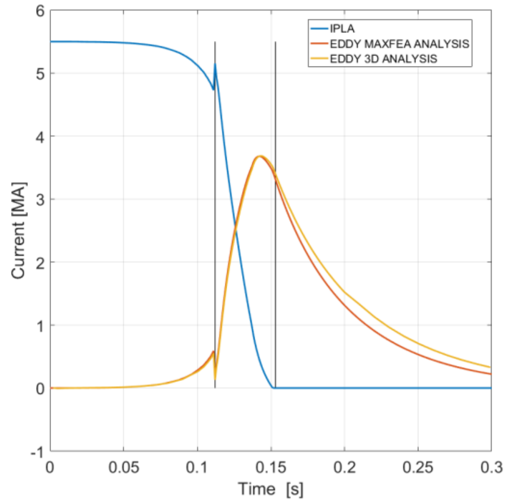

Figure 5.13: Eddy Currents MAXFEA vs Full 3D

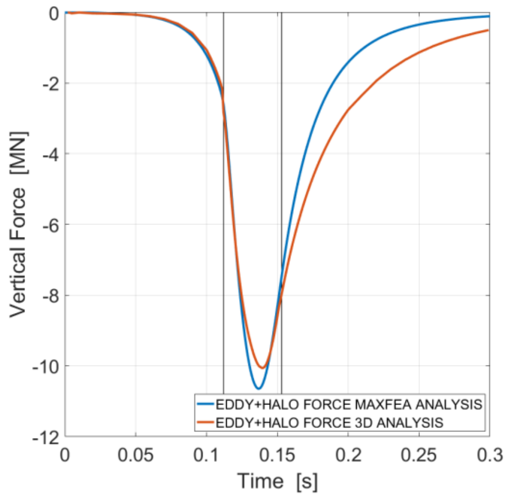

Figure 5.14: Vertical Force due to both eddy and halo currents over 360°: MAXFEA vs Full 3D

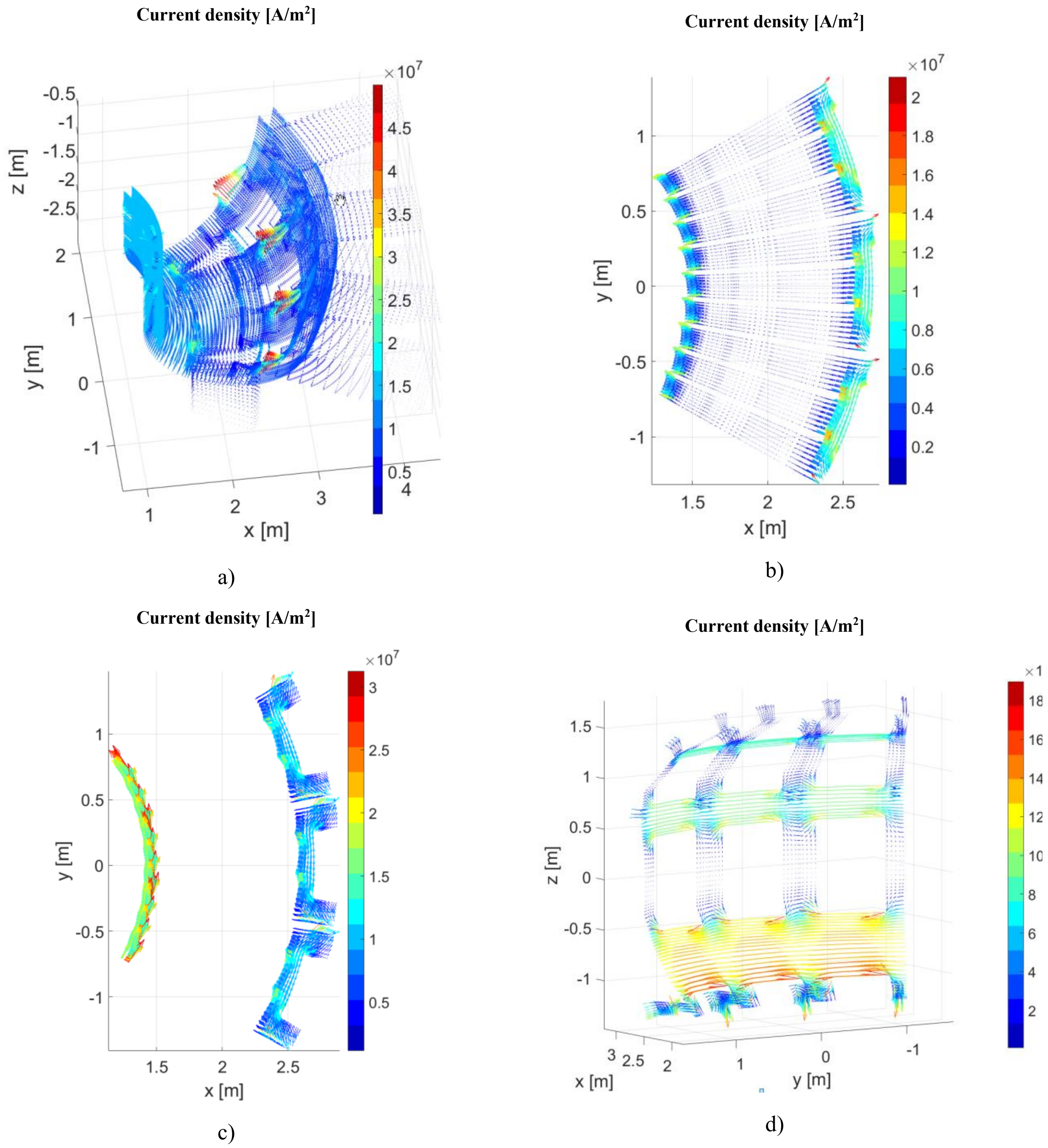

Figure 5.15: Eddy current distribution at 0.143s a) VV b) Divertor cassettes c) Divertor inboard and outboard supports d) Stabilizing plates + Supports

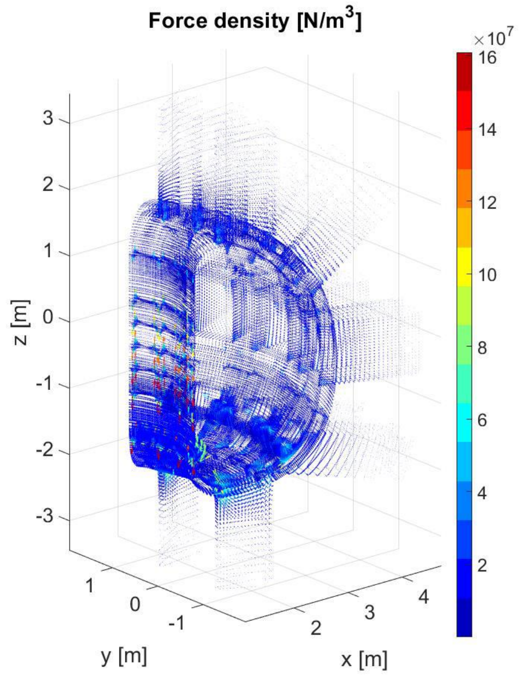

Figure 5.16: Force distribution due to eddy currents (PFV+TFV) at 0.143s in all the structures (VV + stabilizing plate and supports + divertor cassettes and supports)

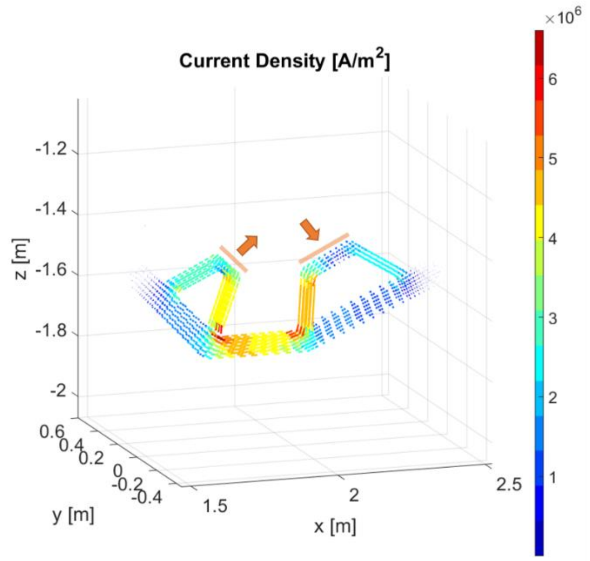

Figure 5.17: Halo current distribution in a divertor cassette at 0.129s together with the assumed in and out locations

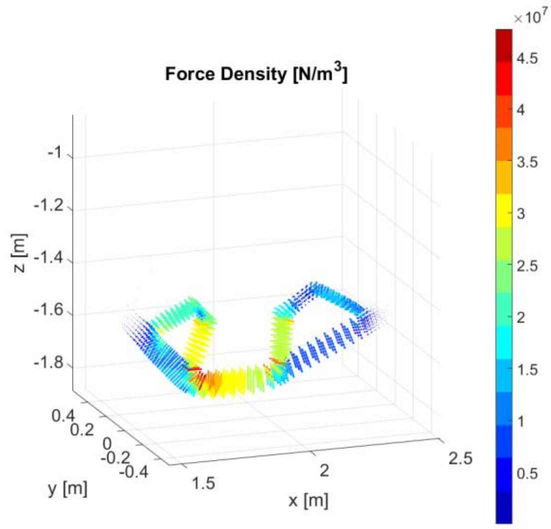

Figure 5.18: HC force distribution in a divertor cassette at 0.129s

5.3.2 Structural analyses

The structural results, in terms of total, radial and vertical displacements and von Mises stress, are shown in the following sections. In the stress contour maps the values lower than the prescribed stress limit (i.e. 186.7MPa for 316LN steel @60°C) are represented with colors, with the purpose to highlight only the portion of the model that violate the allowable limits. These values have been calculated as 2/3 of the yielding stress, as explained in the ITER structural design criteria [77].

5.3.2.1 DVDE slow at eddy+halo F_z peak (0.140s)

In this section the results, in terms of displacements and stresses, are illustrated for a DVDE slow with CQ duration of 40ms at 0.140ms. This time instant corresponds to the maximum value of vertical force due to both eddy and halo currents. In Figure 5.19 radial, vertical and total displacement are represented from left to right respectively. The maximum radial displacement, which occurs on the gravity support, is equal to 1.92mm. The maximum values of the vertical (at bottom curved VV portion) and the total (at gravity support) displacements are instead -1.63mm and 1.92mm, respectively.

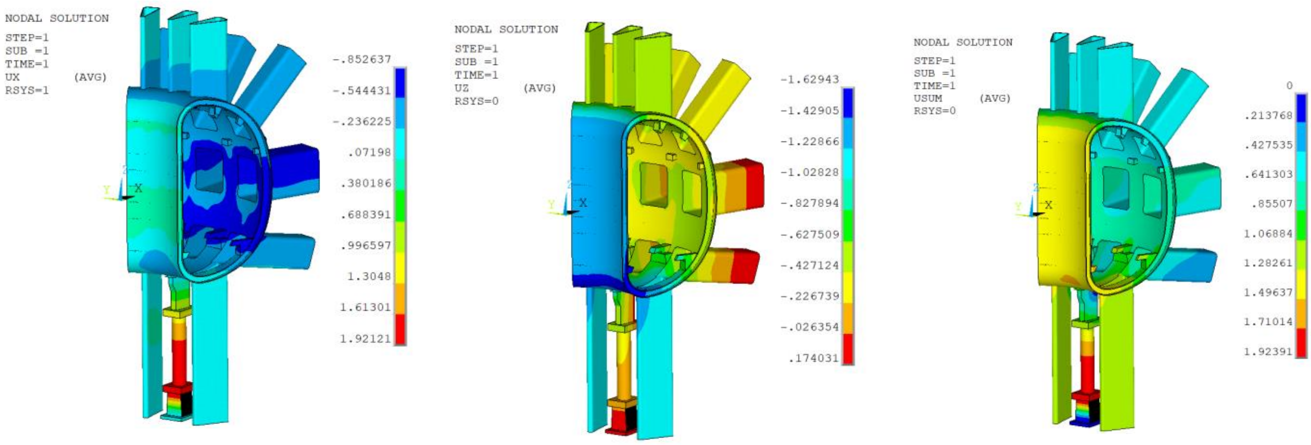

Figure 5.19: DVDE slow (No TPF) @0.140s: radial displacement (left), vertical displacement (center) and total displacement (right).

An overview of the von Mises stress contour on the whole 3 sectors is given in Figure 5.20 left. It is possible to observe how the stress level is below the allowable value except that in limited zones of the structure. Figure 5.20 right shows a zoom in the upper ports zone. As observable from Figure 5.21, the stress limit is violated on the VV outer shell all around the pedestal and also in different portions of the toroidal and poloidal nearby the support. However, it must be said that some parts of the ribs are modelled without any fillet, circumstance that leads to numerical peaks. It can be stated that the most critical zone is represented by the connection of the pedestal with the outer vessel.

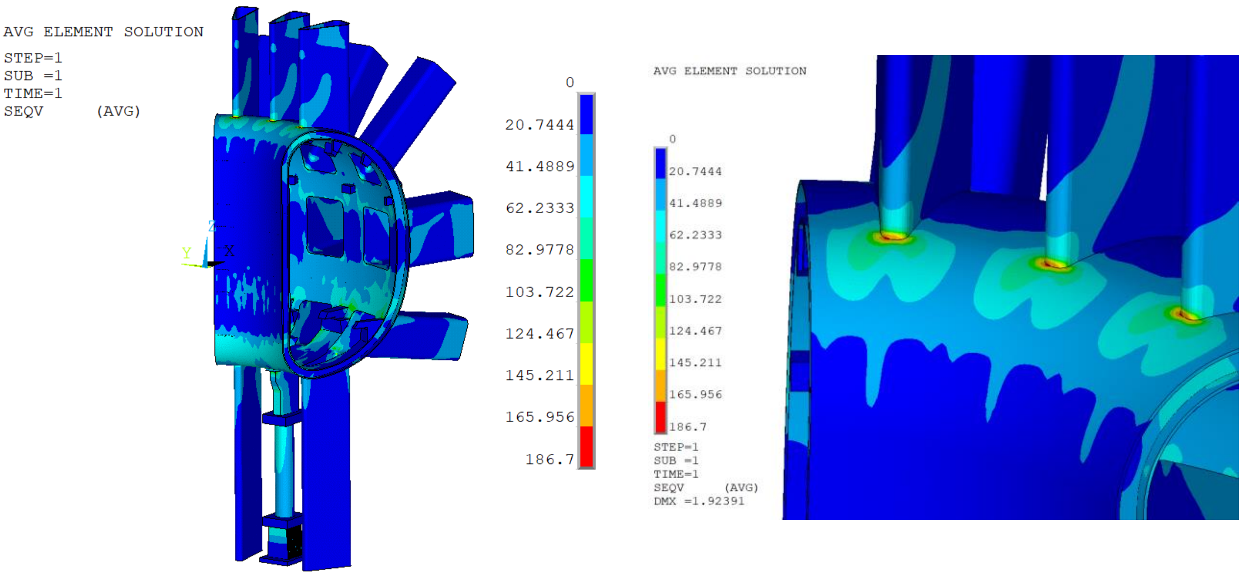

Figure 5.20: DVDE slow (No TPF) @0.140s: overview of von Mises stress contour of the three sectors (left) with a zoom of the upper ports (right).

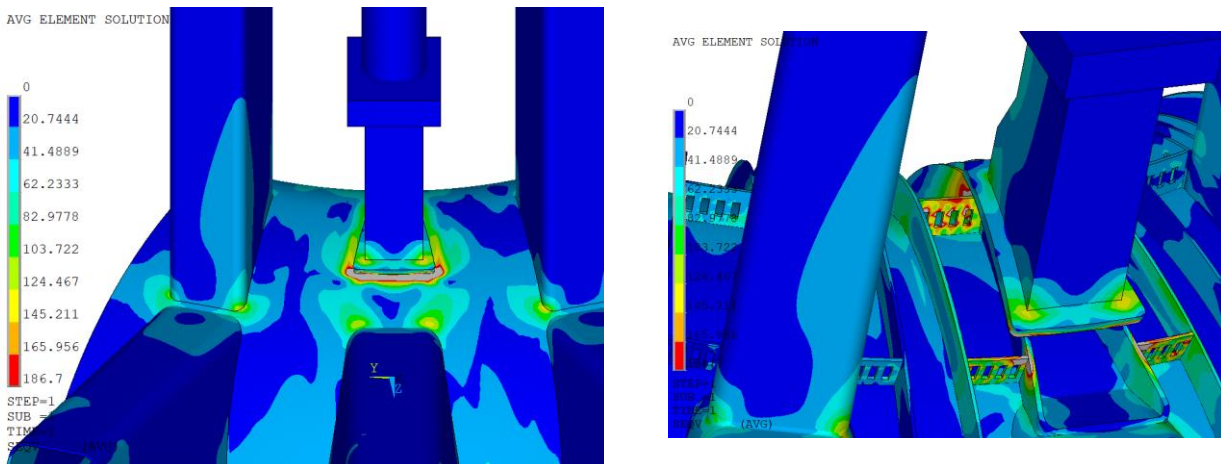

Figure 5.21: DVDE slow (No TPF) @0.140s: von Mises stress contour around the connection of the gravity support with the VV outer shell (left) and VV internal overview (right).

5.3.2.2 DVDE slow at eddy+halo with TPF=2 F_z peak (0.140s)

In this simulation a TPF, equal to 2, for the halo currents has been taken into account. As consequence of the halo force TPF, the minimum amplitude of the structural model to be considered is 360°. In *Figure 5.22*, the radial, vertical and total displacements are represented from left to right respectively. The maximum radial displacement, which occurs on the gravity support, is equal to 2.08mm. The maximum values of the vertical (inboard VV region around last three sectors) and the total displacements (gravity support) are instead -2.03mm and 2.09mm respectively.

An overview of the von Mises stress contour is given in Figure 5.23 left. It is possible to observe how the stress level also in this case is below the allowable value except that in limited zones of the structure. Figure 5.23 right shows a zoom in the upper ports zone. As observable from Figure 5.24, right the stress limit is violated in different portions of the toroidal and poloidal ribs in correspondence of the pedestal. The most critical zone is also in this case represented by the connection of the pedestal with the outer vessel. It is possible to state that this zone is the most stressed, especially in correspondence of the maximum halo TPF value.

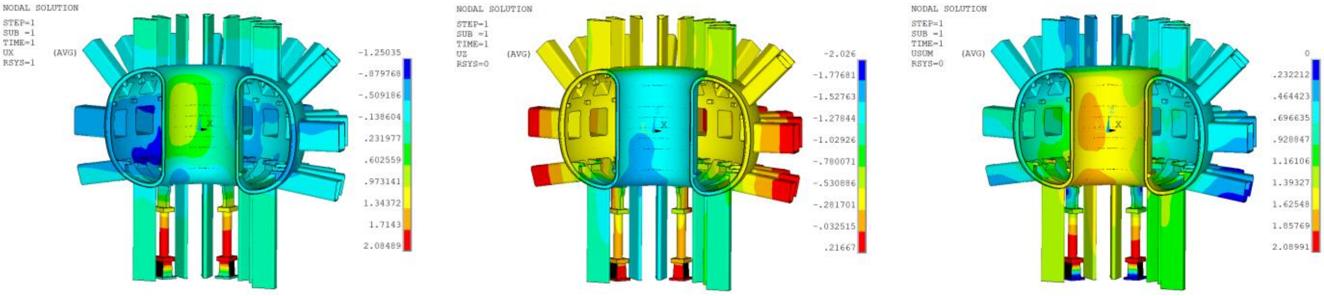

Figure 5.22: DW + EM loads of DVDE slow (TPF = 2): radial displacement (left), vertical displacement (center) and total displacement (right).

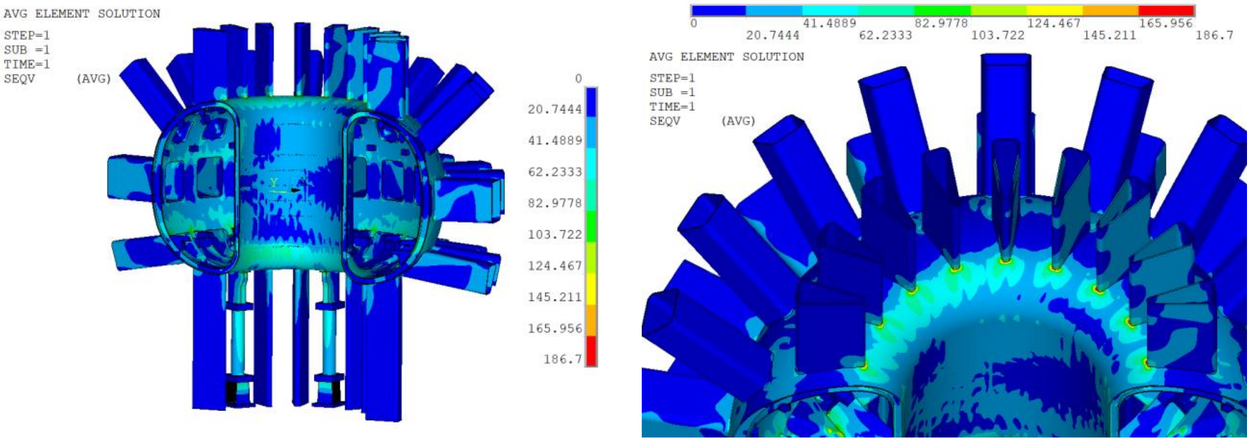

Figure 5.23: DW + EM loads of DVDE slow (TPF = 2): overview of von Mises stress contour expressed in MPa of the half of the VVP (left) with a zoom of the upper ports (right).

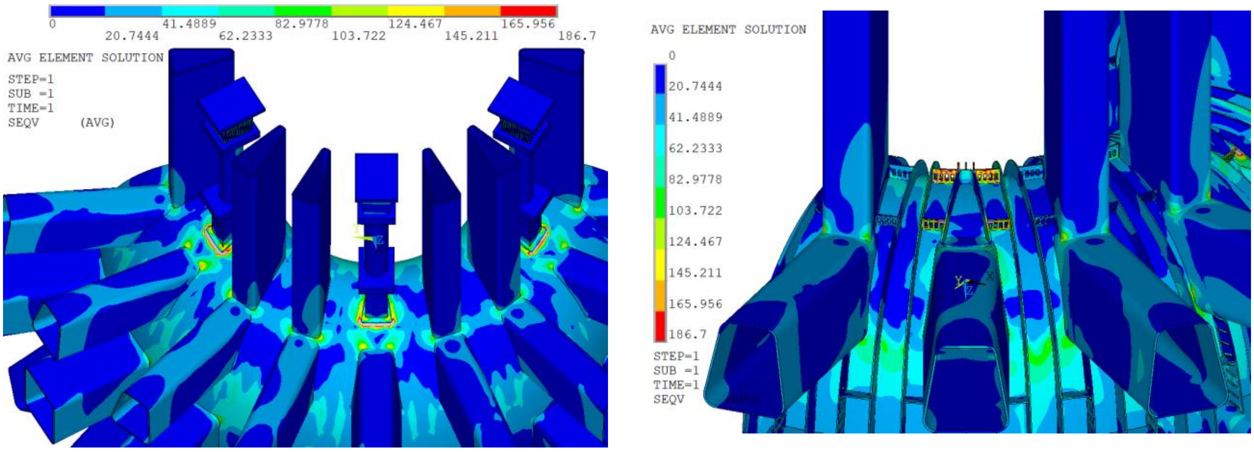

Figure 5.24: DW + EM loads of DVDE slow (TPF = 2): von Mises stress contour around the connection of the gravity support with the VV outer shell (left) and VV internal overview (right).

5.4 Conclusions

In the context of the DTT project, the MAXFEA code has been used in combination with ANSYS APDL following the proposed methodology to study the EM and structural response of the DTT VVP during plasma VDEs. From this study, it has emerged that the VVP mechanical response is acceptable in all the scenarios but, during a particular event, namely the DVDE slow scenario, a stress concentration in correspondence of the connection of the pedestal with the VV outer shell has emerged. Downstream this analysis, mechanical reinforcements in this zone have been introduced in order to optimize the design. The aim of this Section is to show the successful application of this novel procedure in this context and its reliability as supporting tool in the final stage optimization design of these kind of components. In particular, in this Section the abovementioned DVDE slow scenario has been presented. The EM analysis has shown that a vertical force peak of around -10MN is reached as the result of the combination of eddy and halo currents during the CQ phase. From the structural point of view, the EM loads occurring at this time instant produce a stress concentration localized in the connection of the pedestal with the outer vessel. This stress concentration has required the introduction of mechanical reinforcements in this zone in order to optimize the VVP design.

The studies herein presented led to journal publications [75] [76].

6 ST40

Tokamak Energy Ltd. is a privately funded company based in the UK. Founded in 2009, the company is developing compact fusion power plants based on two promising technologies: Spherical Tokamaks (STs) and High Temperature Superconductors (HTS) [19]–[21]. The ST route to fusion has generated considerable interest since the mid-1980s [22]–[24]. This concept demonstrates all the main feature of high aspect ratio conventional tokamaks having at the same time the real potential to significatively reduce costs and timescales on the path to Fusion power. Over the years, research has shown that STs have beneficial properties such as operating at high plasma beta, higher elongation and possibly exhibit higher confinement, although more data are needed at higher field and lower collisionality to determine this fundamental aspect [19]. In the past, the first attempts to design ST based devices did not produce convincing design and until recently STs have remained on the margins of Fusion research. However, recent advances in both tokamak physics and superconductor technology have made a ST fusion reactor a possibility. The key technological advance is the advent of rare-earth HTS. This technology allows significant increase in the toroidal field (TF), which was found to improve confinement in STs. The TF magnet can also operate at relative high temperatures, which is beneficial in the design of magnets where space is very limited in central column of a ST. The combination of the efficiency of STs and the benefits of the HTS opens a route to lower-volume fusion reactors. The mission of Tokamak Energy is to exploit this opportunity by pioneering the use of spherical tokamaks in conjunction with HTS magnet technology.

On its path to Fusion power, Tokamak Energy Ltd. is presently operating ST40 [19][25][26]. ST40 is a new generation high field ST whose main design parameters are: $R_0 = 0.4 - 0.6$m, $A = 1.7 - 2.0$, $I_{PLA} = 2$MA, $B_T = 3$T, $\kappa = 2.5$. ST40 is the highest field device of its kind (until recently STs have typically operated at TF around 0.3 – 0.5 T). ST40's main components are presented in Section 6.1. An overview of ST40's latest experimental results is provided in [78]. In the near future, an important ST40 upgrade is planned and foresees the manufacturing and the installation of a new inner vacuum chamber, called IVC2, that is currently in the final design stage. Therefore, the necessity to analyse in detail the Electro-Magnetic (EM) behaviour of this component under the loads coming from plasma disruptions has recently emerged in order to verify the design or drive further modifications. In this context, firstly, similarly to what previously done with JET and ASDEX within the Inter-machine plasma perturbation studies xx, an extensive work was done to validate MAXFEA versus existing ST40 experimental disruptions. This first step was essential to build confidence in the model. Then, a predictive study to analyse the EM response of IVC2 during a plasma disruption has been carried out using MAXFEA code in combination with ANSYS APDL, following the proposed methodology. In particular, an upward VDE fast disruption scenario has been considered. Downstream the EM analysis, the mechanical behaviour of ST40 has been also studied developing a global structural model of the system. The aim of this Section is to present the results of this analysis to show the successful application of this procedure in the context of the new generation high field ST40 tokamak.

The study herein reported is the subject of the journal publication recently submitted to *Fusion Engineering and Design* and currently in the final stage of the review process [79].

6.1 ST40 and IVC2

The main components of ST40 are the Inner and Outer Vacuum Chambers (IVC and OVC) and the toroidal and poloidal field (TF and PF) coils [25]. An overview of the current ST40 main components is given in Figure 6.1. The OVC is a Stainless Steel (SS) structure that houses the IVC, PF and TF coils. The OVC mechanically supports the TF, PF and IVC components and is designed to withstand the strong EM forces expected during both normal (e.g. TF in-plane and out-of-plane forces, PF forces during the plasma scenario, etc.) and off-normal conditions (i.e. plasma disruptions). It is supported by four legs and the entire assembly sits on top of the assembly platform (not reported in Figure 6.1). The IVC is made of 10 mm thick 314 SS, apart from the centre tube that is made of 4 mm thick Inconel covered by a set of graphite limiters, and it is designed to be pumped down to ~10^{-8} mbar during plasma operation [25]. A couple of up-down symmetric divertors, presenting a castellation of graphite tiles on copper plates and connected with the IVC through SS supports, have recently been introduced in ST40 to enable double null (DN) diverted operations with up to 1MA of plasma current [80].

Regarding the ST40 coils, they are all made of copper. The TF magnet consists of a central column and outer limbs connected together with flexible copper demountable joints. An overview of the TF system is in Figure 6.1b. The centre post consists of 24 copper wedges with a 15° twisted in the central part to allow connecting one TF turn to the next, while in the outer zone the turns are arranged in 8 limbs with 3 turns in each. To accommodate the EM forces acting on the magnet, each outer limb is equipped with two SS support brackets (top and bottom), connected to the OVC with two carbon fiber straps each. In addition, there are two torque plates, one at the top and one at the bottom of the device (namely the E-Ring in Figure 6.1b), with eight carbon fiber straps each, to add extra support against twisting.

Concerning the PF coils, ST40 presents four pairs of coils, namely the BVL, BVM, BVT and DIV coils, for the plasma current, position and shape control (Figure 6.1c). ST40 has also a Central Solenoid (CS) directly wounded on the TF central column to ramp and maintaining the flattop current but it is not used for inductive start up. At this end, in fact, ST40 uses a process called merging compression (MC) [81], firstly developed for START [82] and later utilized in MAST [83]. For that purpose, two in-vessel MC coils are installed, as shown in Figure 6.1c, together with a pair of push (PSH) coils located outside the IVC2.

An overview of IVC2 is reported in Figure 6.2. The IVC2 will be composed of three main parts connected through Inconel and SS flanges:

- The domes (top and bottom, green components in Figure 6.2), made of Inconel 718
- The outer shell (dark grey component in Figure 6.2), made of Inconel 718
- The central tube (bluish grey component in Figure 6.2), made of SS316

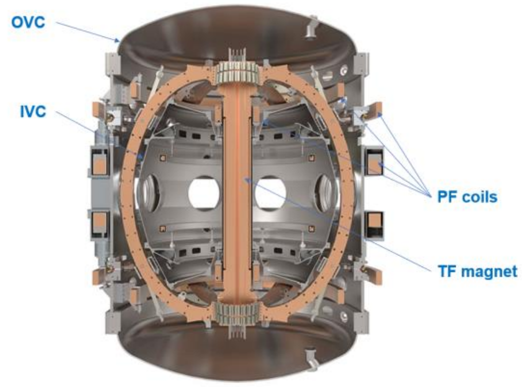

a)

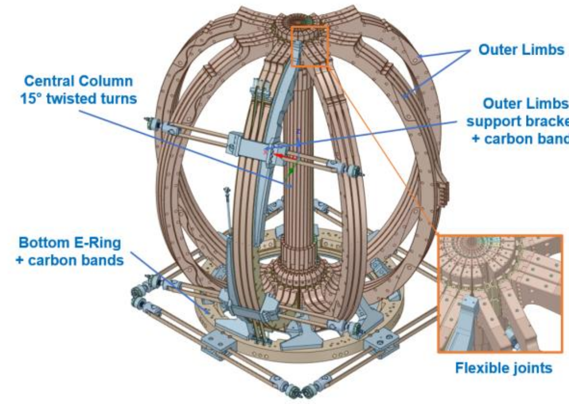

b)

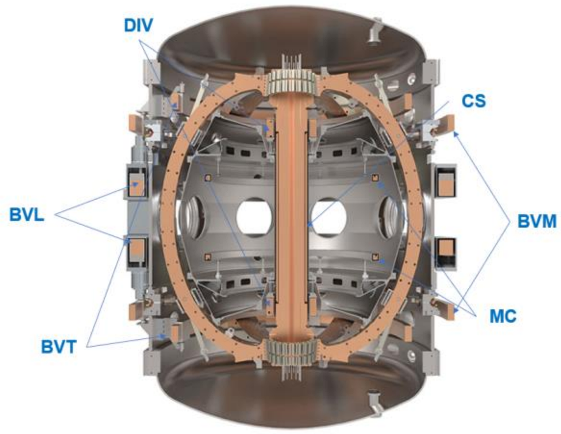

c)

Figure 6.1: Overview of ST40 main components a) Poloidal plane view of the main components b) Overview of the TF system with the central column, the outer limbs, the SS brackets + carbon bands, the bottom E-Ring + carbon bands and a zoom of the flexible joint connection c) PF coils system

Together with the IVC2, new divertor and stabilizing plate concepts will be introduced. In particular, two symmetric (top and bottom) divertors will be installed (Figure 6.2). The copper stabilization plates will be encapsulated in a SS jacket and connected in anti-series from top to bottom through an interconnection (in this arrangement any up/down symmetric change in flux will not induce any current to flow; but antisymmetric changes in flux will induce current to flow). A set of molybdenum tiles will be mounted on the SS case and will face the plasma. A similar concept is foreseen for the stabilizing plates. These passive stabilization structures guarantee a significative reduction of the vertical instability growth rate, while allowing for Merging/Compression start up, mid-plane and upper launched NBI's and being compatible with the divertor power exhaust [84].

Furthermore, the upgrade will include the installation of a new set of PF coils, namely the SX coils. These coils will provide for the formation of secondary x-points allowing the test of advanced divertor magnetic configurations, like the reference hybrid quasi-snowflake DN equilibrium analysed in this study and presented in Section 6.4.1.1.

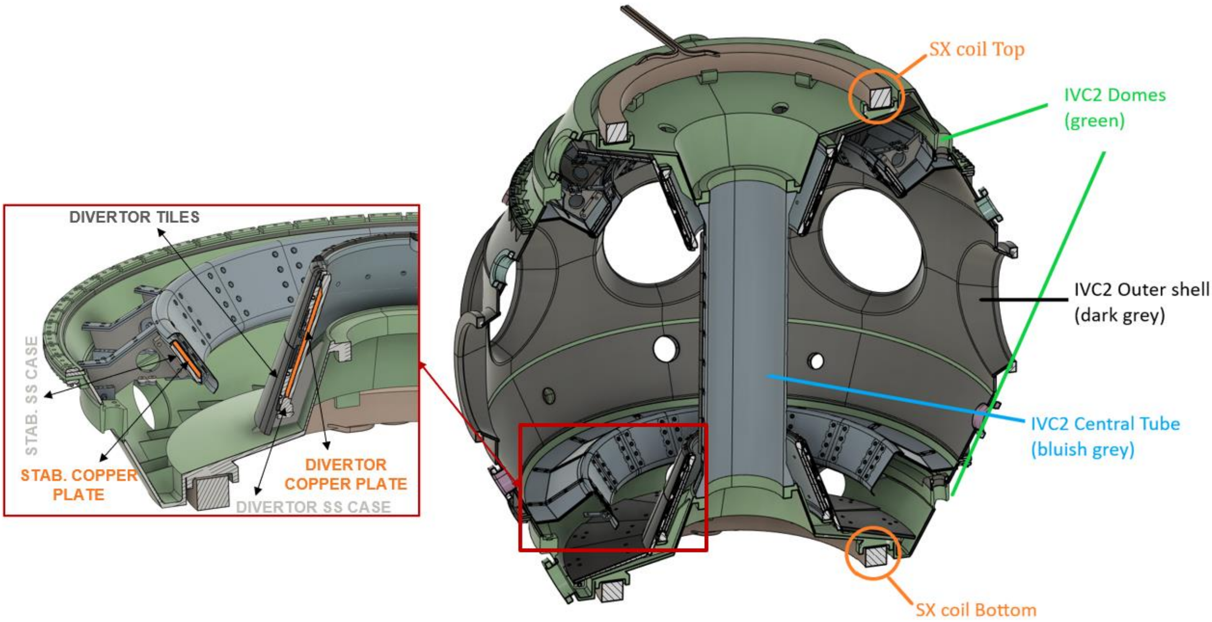

Figure 6.2: Overview of IVC2 with the Domes, the Central Tube, the Outer shell and the SX coils with a zoom of the Divertor and the Stabilizing Plate

6.2 MAXFEA validation against experimental VDEs

In this paragraph, the main results of the study aimed at validating MAXFEA against existing ST40 experimental disruptions are presented. This step was essential to build confidence in the model in view of the predictive analysis on IVC2. Two shots terminating with uncontrolled VDEs, namely shot #7153 and shot #8498, were simulated by means of MAXFEA with the goal to reproduce the plasma dynamic behaviour starting from the experimental data. MAXFEA simulations results and experimental observations were finally compared in terms of induced currents and plasma movement, showing good agreement.

Figure 6.3 left and Figure 6.4 left show the experimental plasma current together with r_c and z_c evolutions reconstructed by EFIT for #7153 and #8498 respectively. In both figures, some characteristic times of interest are also reported:

- The beginning of flat-top phase (tsof), represented with the dashed red line
- The disruption time (td), corresponding to the beginning of the TQ phase and represented with the dashed purple line
- The start of CQ (tCQstart), represented with the dashed green line
- The equilibrium time (tEQ), corresponding to the instant chosen as starting point for the simulation and represented with the dashed yellow line

Whereas, Figure 6.3 right and Figure 6.4 right report the plasma boundary at tEQ together with r_c-z_c trajectory for #7153 and #8498 respectively.

The shot #7153 presents the following main characteristics:

- Plasma current at flat top of about 500 kA

- VDE starts at ~ 20 ms when plasma start to move upward, and the vertical stability is lost. From this time on, plasma current progressively decreases from the flat-top value
- At ~ 59.7 ms (td), when plasma current is about 465.3 kA, TQ occurs and the characteristic plasma current spike is observed due to the flux conservation and the redistribution of the current (TQ duration of about 1 ms);
- Then, CQ begins (from a plasma current peak of ~ 491.7 kA at ~60.7 ms) and plasma losses all its current in ~ 2.6 ms (CQ duration).

The shot #8498 presents the following main characteristics:

- Plasma current at flat top of about 530 kA
- VDE starts at ~ 65 ms when plasma start to move downward, and the vertical stability is lost. From this time on, plasma current progressively decreases from the flat-top value
- At ~ 102,9 ms (td), when plasma current is about 419.2 kA, TQ occurs and the characteristic plasma current spike is observed due to the flux conservation and the redistribution of the current (TQ duration of about 0,5 ms);
- Then, CQ begins (from a plasma current peak of ~ 431.4 kA at ~103.4 ms) and plasma losses all its current in ~ 2.65 ms (CQ duration).

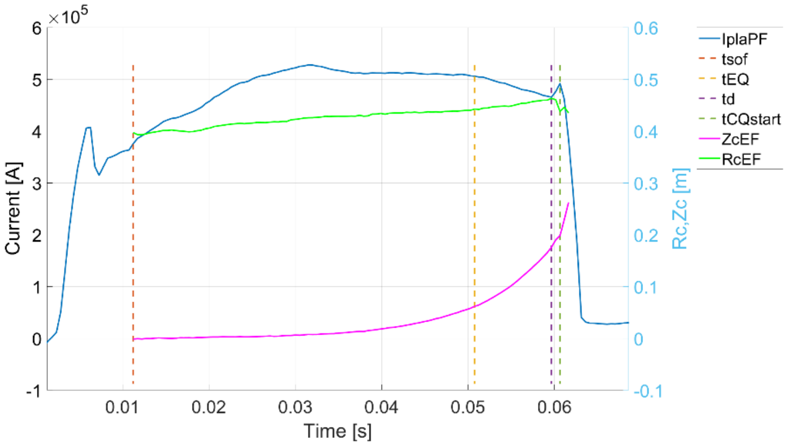

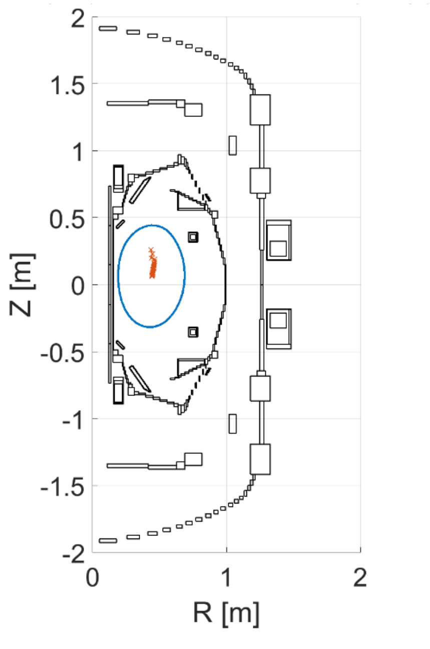

Figure 6.3: left) Experimental signals from shot #7153:plasma current in blue, rc in green, zc purple and characteristic times (tsof, tEQ, td, tCQstart); right) reference plasma LCFS at tEQ and rc-zc trajectory

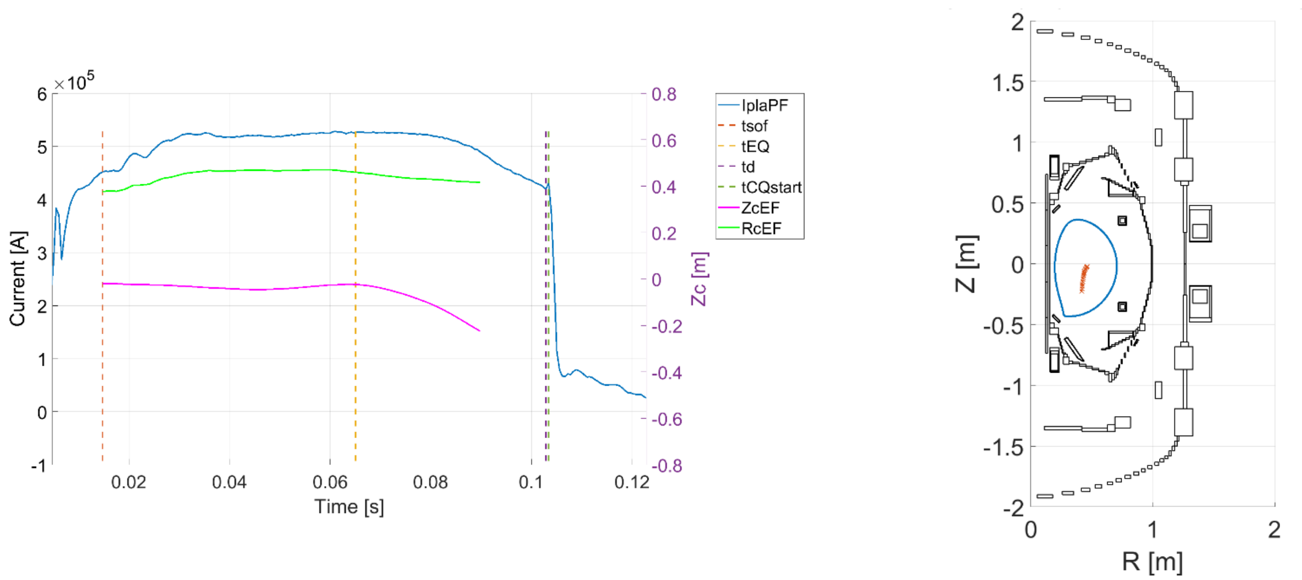

Figure 6.4: left) Experimental signals from shot #8498:plasma current in blue, rc in green, zc purple and characteristic times (tsof, tEQ, td, tCQstart); right) reference plasma LCFS at tEQ and rc-zc trajectory

At first, the plasma equilibrium at tEQ has been reproduced and compared with the experimental reference. In both cases the plasma equilibrium is well reproduced in terms of plasma shape, position and main parameters, as it can be appreciated in Figure 6.5, where the experimental plasma LCFSs are reported together with the MAXFEA reproduced ones. Then, starting from this equilibrium a transient evolution has been performed taking the experimental event as reference. In particular, similar evolutions of the plasma main parameters (i.e. Ip, β_p, li) are imposed. Figure 6.6 a-b shows the plasma current evolution simulated in MAXFEA together with the experimental signal for #7153 and #8498 respectively.

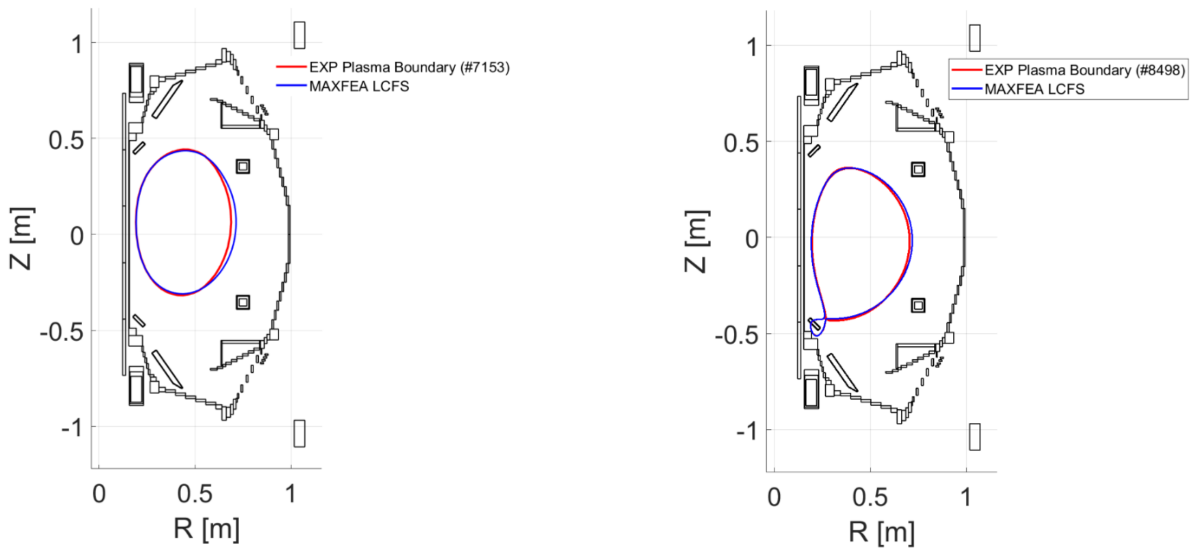

a) b)

Figure 6.5: Experimental plasma equilibrium (red line) vs the MAXFEA one (blue line) at tEQ a) #7153 b) #8498

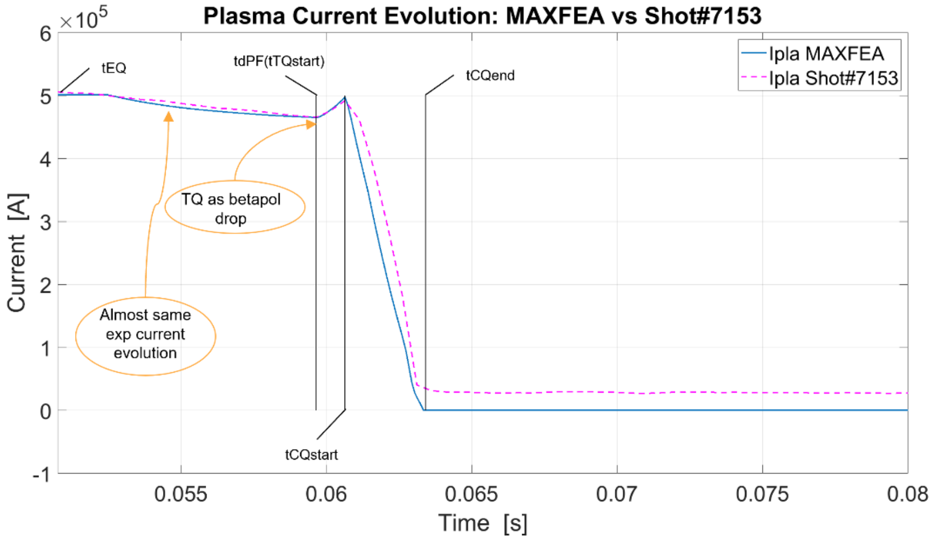

a)

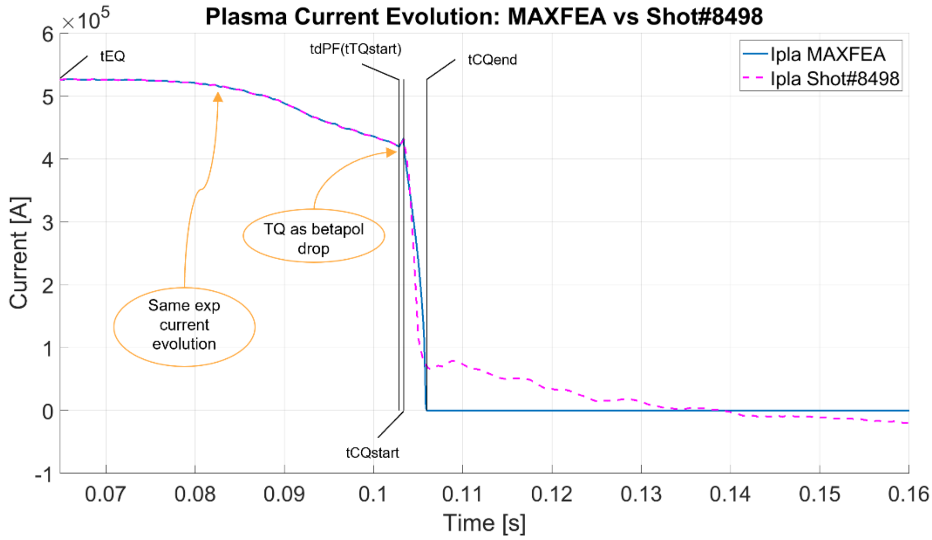

b)

Figure 6.6: Plasma current evolution in time: experimental signal (dashed purple line) and MAXFEA simulation (blue line) a) #7153 b) #8498

Finally, MAXFEA results and experimental observations have been compared in terms of plasma movement and induced currents. Figure 6.7 shows a sequence of snapshots of the plasma LCFS during the VDE as computed with MAXFEA, together with the experimental and the simulated trajectory of the plasma centroid (r_c – z_c) for both the cases. Whereas, Figure 6.9 shows the currents induced in the so-called gas shelves structures (namely GAS SHELF TOP and GAS SHELF BOTTOM in Figure 6.8) measured by dedicated Rogowski coils together with the MAXFEA eddy current evaluated in the same components. A very good agreement has been found in both cases, although in the shot #8498 the Rogowski signal related to the GAS SHELF TOP was not acquired due to a technical fault.

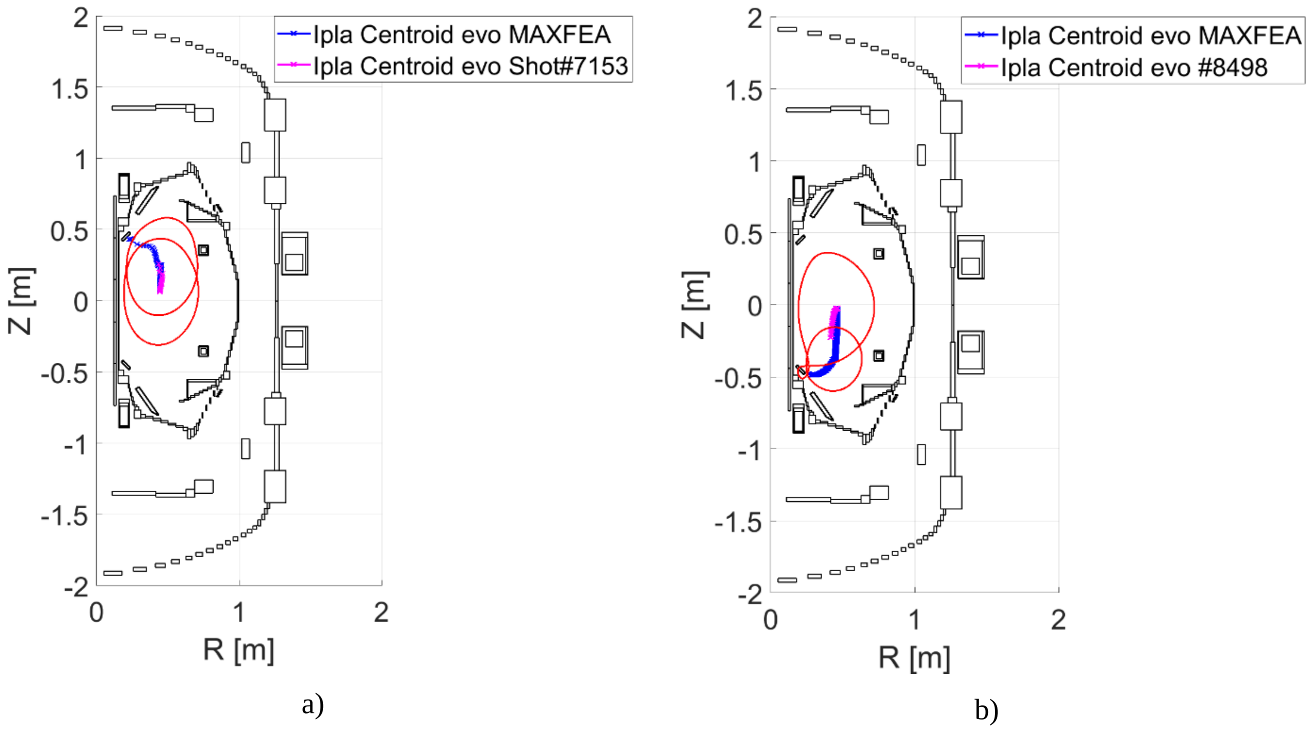

Figure 6.7: Plasma LCFSs at two different time instants during the VDE together with the experimental (purple line) and simulated (blue line) $r_c - z_c$ evolution a) #7153 b) #8498

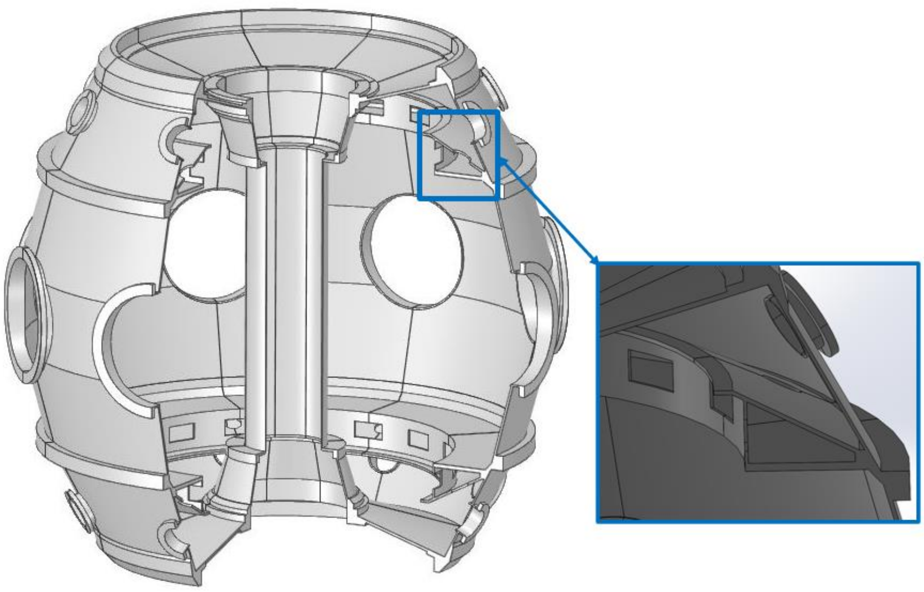

Figure 6.8: Gas shelves structures

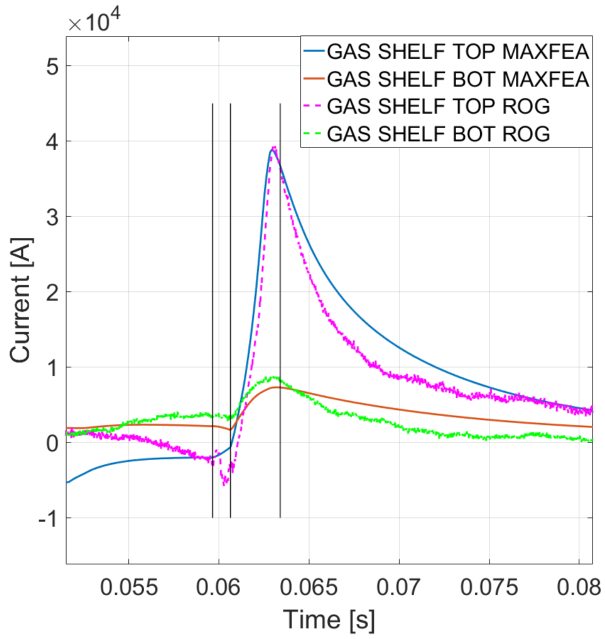

a)

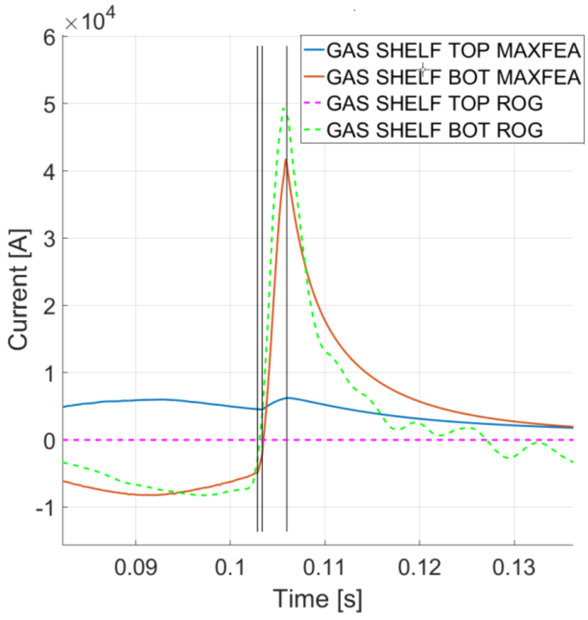

b)

Figure 6.9: Eddy currents in the gas shelf top and bottom structures: experimental signals (dashed lines) and MAXFEA simulation (solid lines) a) #7153 b) #8498

6.3 Methodology

Once validated, a predictive study to analyse the EM response of IVC2 during a plasma disruption has been carried out. In this study, the proposed methodology is applied to study an UVDE scenario with a CQ duration such that $\Delta t_{80\text{-}20}$ = 0.9ms as presented in Section 2. All the EM contributions are computed and then applied to the structural model.

The 3D structural model has to be realized with different features with respect to a 3D EM simulation, implying dissimilar mesh models. Hence, the loads coming from EM simulations, in terms of force densities, have to be interpolated on the mechanical mesh model.

Two critical instants are individuated, namely the time instant of maximum halo current (herein identified as halo peak), occurring during the CQ, and the time instant of maximum eddy current (herein identified as eddy peak), occurring at the end of CQ. The structural response of ST40 is studied at these two critical time instants.

6.4 FE models

6.4.1 EM models

6.4.1.1 MAXFEA 2D axisymmetric model

In this section the MAXFEA model is presented. An overview of the model is reported in Figure 6.10. The model includes:

- PF coils system (red areas in Figure 6.10b):
  In particular, the top and bottom MC coils have been considered connected in series in a closed loop configuration (11 turns each). The same assumption has been made for the PSH coils (8 turns each).

- OVC
- IVC2
- Divertors:

  The toroidal continuous copper plate of the top divertor is connected in anti-series with that of the bottom divertor and they are insulated from the relative SS case.
- Stabilizing Plates:

  The same anti-series connection of the divertors
- E-Rings

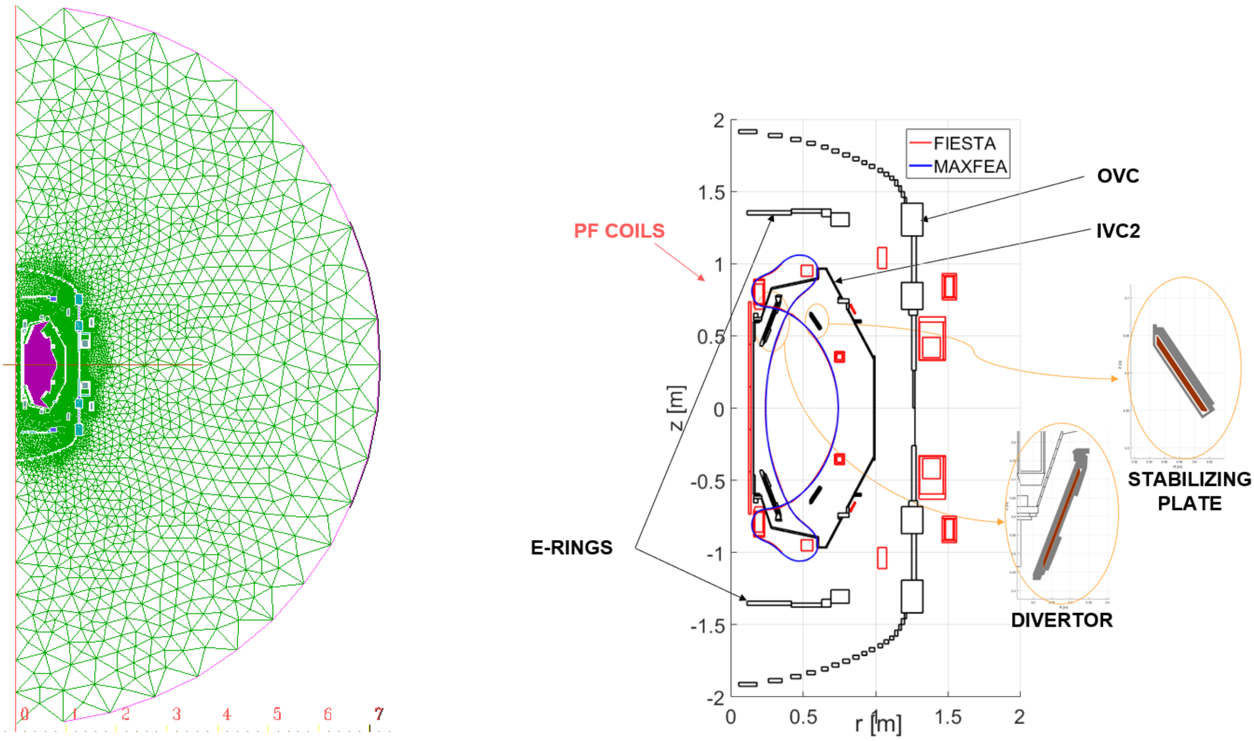

a) b)

Figure 6.10:MAXFEA model a) Overview of the whole FEM domain b) Zoom in the plasma region. The PF coils are represented in red. The other components included are indicated with arrows. A zoom of the Divertor and the Stabilizing Plate is shown on the right. The reference equilibrium reproduced by means of MAXFEA is reported in blue, red for the FIESTA

The reference plasma equilibrium reproduced with MAXFEA, namely a hybrid quasi-snowflake DN configuration with I_{PLA} = 2MA, is shown in Figure 6.10b, together with that computed by means of FIESTA code. The FIESTA code is a plasma equilibrium code developed in the Culham Centre for Fusion Energy (CCFE). The comparison shows a very good agreement between the two codes, proving MAXFEA capability to treat such kind of advance plasma configurations.

As far as the disruption scenario is concerned, an UVDE fast has been considered and modelled as follow:

- Destabilizing kick is imposed @1ms after the start of the simulation to force plasma upward movement imposing a small voltage on a dummy coil for few time steps (time step = 0.1ms).

- Consequently, the plasma starts to move vertically towards the wall, reducing accordingly the plasma area and the total plasma current since flux conservation is assumed.
- At a certain point, when the plasma touches the wall and becomes limiter, Thermal Quench (TQ) is imposed as beta poloidal drop in 1 time step and a plasma current spike is found, as regularly observed experimentally, due to the flux conservation and redistribution of the plasma current.
- Current Quench (CQ) starts immediately after, imposing a proper negative voltage on plasma. The CQ duration $\Delta t_{80\text{-}20}$ = 0.9ms. During the CQ phase, halo current growth is considered.

6.4.1.2 APDL 3D Models

The 3D APDL model is shown in Figure 6.11. The model consists of a ST40 sector (45°) and features approximately 850k elements and 700k nodes. The adopted element type is the SOLID97. The model features a high quality mapped mesh with mean values in terms of skewness and warping factor of about 0.220 and 0.004, respectively. Only 0.617% and 0.045% of the elements exceed skewness > 0.7 and warping factor > 0.3, respectively, and it is worth to say that these elements are localized in very limited zone of the air domain, far enough from the region of interest.

The same mesh model is adopted for Poloidal Field Variation, Toroidal Field Variation and Halo Current simulations (PFV, TFV and HC), following the proposed methodology. Regarding the HC simulation, the total HC computed with the MAXFEA simulation is injected into the structures through chosen in and out locations. The assumption of the in and out locations will be presented later in Section 6.5.1.3. In Figure 6.12, a zoom of the Divertor and the Stabilizing Plate is provided.

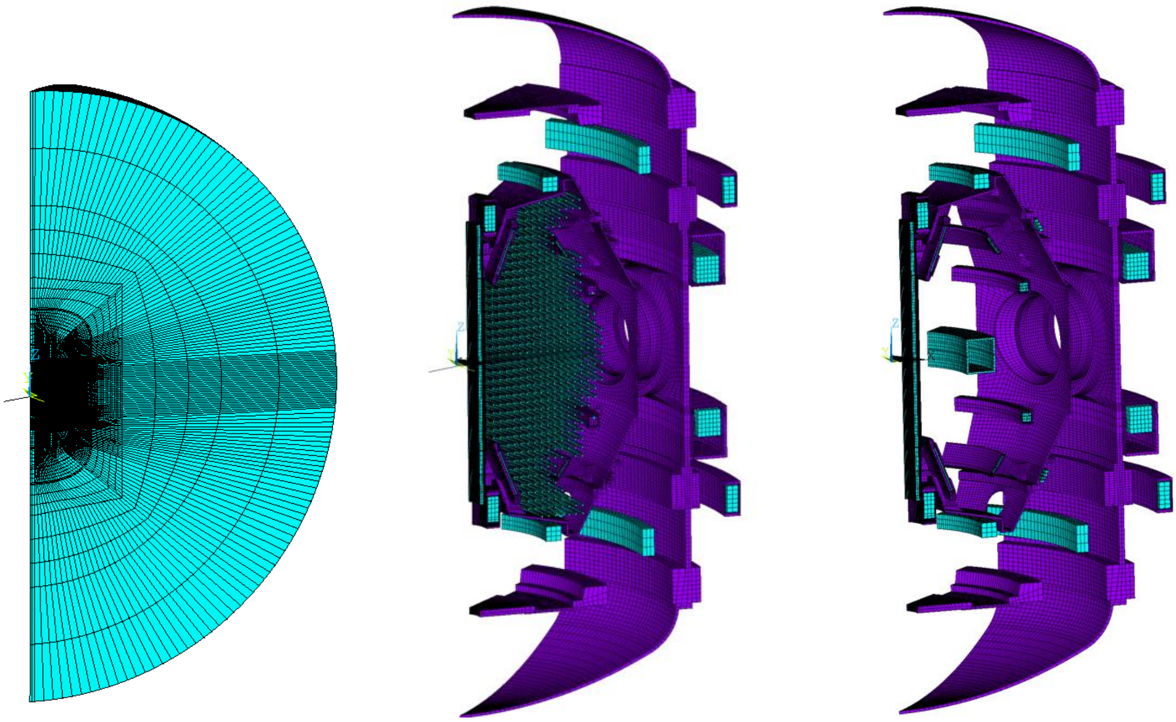

Figure 6.11: 3D APDL EM model: overview of the whole model with region (left), mesh with filaments for PFV analysis (center) and mesh with torus for TFV analysis (right)

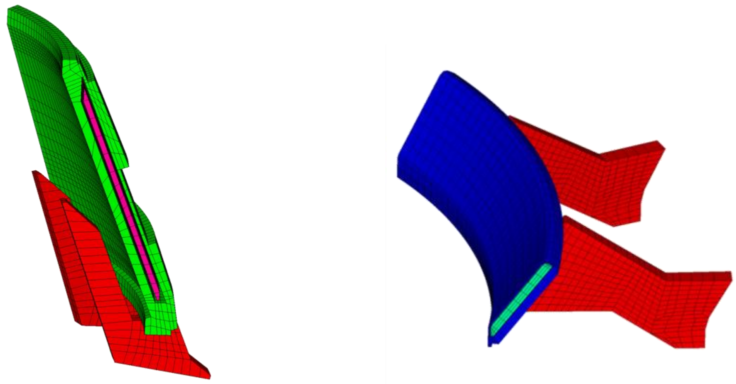

Figure 6.12: Zoom of the bottom Divertor (left) and Stabilizing Plate (right)

To simplify the whole model and reduce significatively its dimension, the presence of the TF coil system is neglected, since its presence does not affect the results significatively. The contribution of the magnetic field produced by the TF magnet on the structures is evaluated with a magnetostatic analysis by means of a different dedicated model (herein identified as TF COIL MODEL). The developed model is shown in Figure 6.13. It consists in a full detailed 360° mesh of the TF magnet with the 15° twisted central wires, the outer limbs and the flexible joint connections. The adopted element type is SOLID5 which allows the computation of the magnetic field in the components by means of an integral formulation. Therefore, no air mesh is required. The TF model features approximately 1.1m elements and 1.4m nodes. Computing the toroidal field with this high level of detail allows to evaluate the effect of the ripple and the presence of possible local effects due to the close vicinity of certain components with the magnet turns.

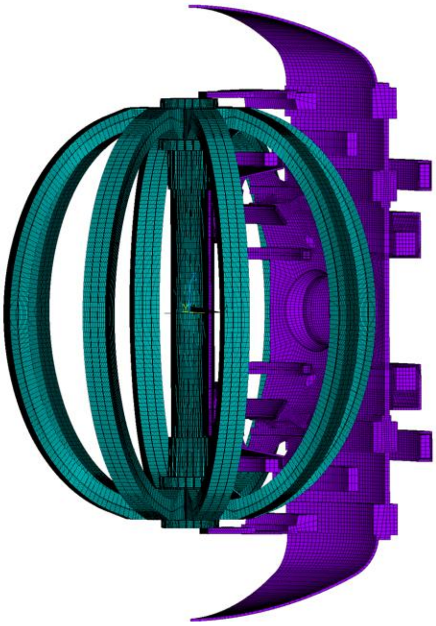

Figure 6.13: Overview of the TF COIL MODEL

6.4.2 Structural Model

The structural model has been developed considering the whole 360° of ST40. The mesh model consists of 4310k nodes and 3341k elements composed of SOLID185 bricks and includes more than 100 components, connected through 450 bonded contact set in ANSYS Workbench and with 300 joints elements defined with APDL code. An overview of the whole mesh in provided in Figure 6.14, together with main components isolated. The bellows are simulated with COMBIN7 element which present a stiffness calculated through a separate analysis. The IVC gravity support that connect the IVC to OVC are modelled through a MPC184 General element with all the displacements fixed, while all rotations are kept free. The carbon fiber straps for the connection of TF magnets outer limb with OVC are simulated with MPC184 General elements with displacements and rotations set free with a stiffness determined through a separate analysis, while the connections between these joints and the OVC are modelled through MPC184 Beam element. The additional carbon fiber straps connected to the E-Ring are modelled respecting the real geometry, while the connection with the OVC remain realized through MPC184 Beam element. The whole model is supported through the OVC legs that are fixed to the ground with a final plate; the connections between the OVC legs and its final plate is modelled through MPC184 Beam elements. The EM loads acting on the structure are interpolated from the EM models with the distance average method in ANSYS Workbench and applied as body force densities on the components.

a)

b)

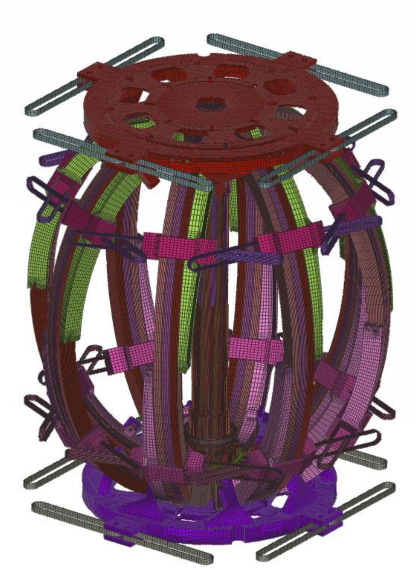

c)

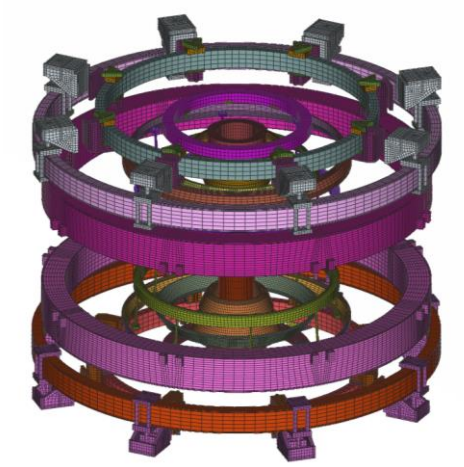

d)

Figure 6.14: a) Overview of ST40 global model mesh b) IVC2 c)TF coils and supports d) PF coils and supports

6.5 Results

6.5.1 EM analysis

The results of the magnetostatic analysis aimed at evaluating the magnetic field in the structures produced by the TF magnet are shown in Section . Then, the EM response of ST40 during the VDE scenario previously discussed is presented. In particular, Section reports the results of the MAXFEA analysis, while in Section the subsequent full 3D EM analysis (PFV+TFV+HC) is exposed.

6.5.1.1 TF coil magnetostatic analysis

As discussed, the contribution of the magnetic field produced by the TF magnet on the structures is evaluated with a magnetostatic analysis by means of the TF COIL MODEL. Figure 6.15 shows the current distribution in the TF turns together with a zoom corresponding to the connection between the central column and the outer limb, and Figure 6.16a-b show the resulting magnetic field in the poloidal and equatorial planes, respectively.

From Figure 6.16b, it is possible to observe the presence of the ripple. In Figure 6.16c, the magnetic field along PATH 1 and PATH 2 (shown in Figure 6.16b) is reported together with the simplified analytic formulation of the field as $B = A/r$, in which $A = B_T \cdot R = 1.2\ T \cdot m$, where $R = 0.4\ m$ and $B_T = 3\ T$. From this figure, we see the ripple has a negligible effect within the plasma zone.

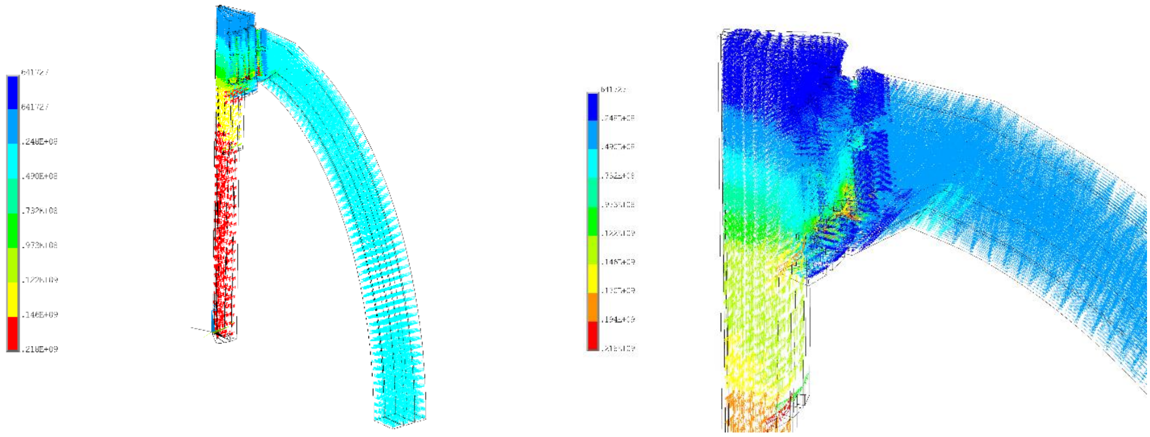

Figure 6.15: Current distribution in the TF coil [A/m^2]. Overview of the upper part of the magnet (left), zoom of the connection between the central column and the outer limb (right)

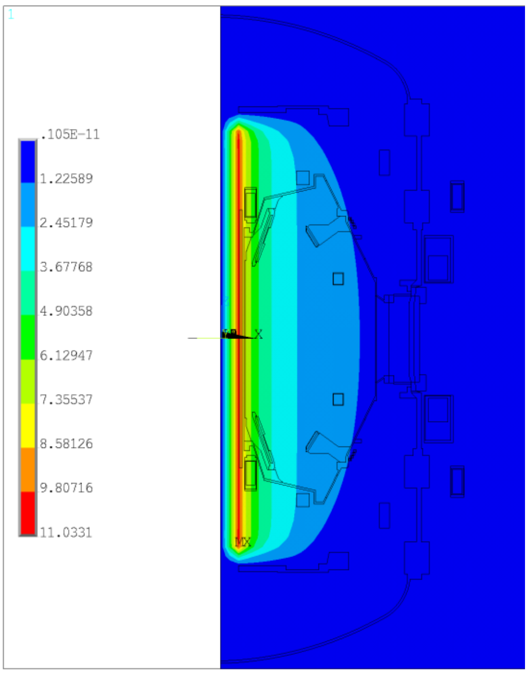

a)

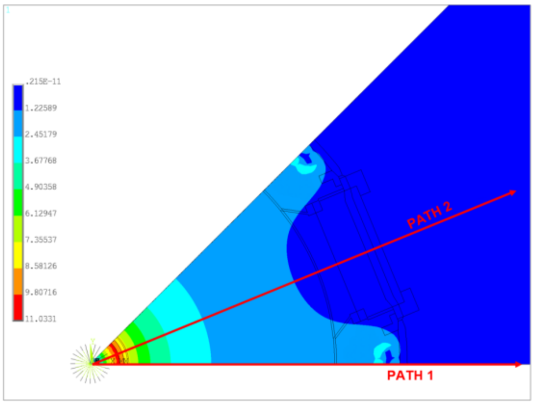

b)

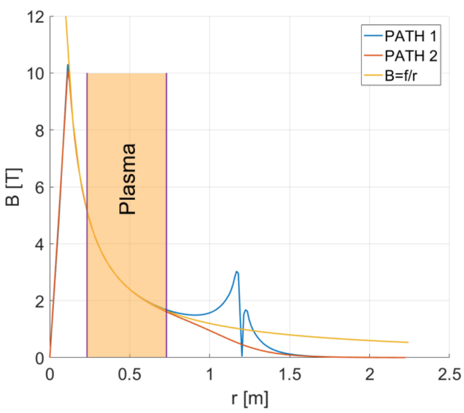

c)

Figure 6.16: Magnetic field produced by the TF magnet [T] a) Poloidal Plane b) Equatorial Plane c) Magnetic field along PATH 1 (blue line) and PATH 2 (red line) together with the analytic formulation $B = f/r$

6.5.1.2 MAXFEA analysis

The results of the MAXFEA UVDE fast simulation are reported from Figure 6.17 to Figure 6.20. In reference to the plasma current (named Ipla and depicted with blue curve in Figure 6.17), in an initial phase, when the plasma is moving upward until it touches the wall, a current reduction is observed because the plasma progressive shrinks and flux conservation is assumed. At a certain point the plasma touches the wall. In correspondence of this time instant, that takes place at 0.0656s and it is identified with left black vertical line in Figure 6.17, TQ is imposed and a current spike is found due to redistribution of the plasma current, as regularly observed experimentally. CQ takes place immediately after and ends at 0.0674s (identified with right black vertical line). In the CQ phase, HC arises as shown with the red curve, reaching a peak of about 0.54MA at 0.0668s. At the end of this phase, at 0.0674s, eddy current reaches its maximum of about 1.2MA (yellow curve). The vertical EM forces acting on the IVC2 are instead reported in Figure 6.18. The total vertical force acting on IVC2 due to the eddy currents is represented in blue. This force should be intended as the sum of the force directly experienced by the IVC2 and the forces that act on the components that are mechanical connected to it, namely the DIV, SX, PSH and MC coils, the Divertors and the Stabilizing Plates. This curve shows a peak of about -0.32MN at 0.0667s. Instead, the red curve shows the global vertical force due to the halo current, whose peak of about 0.23MN occurs at 0.0668s. Yellow curve shows the total eddy + halo force, highlighting a negative peak during the CQ, about -0.1MN at 0.0666s, and a positive peak slightly after the plasma termination, about 27kN at 0.0691s.

In Figure 6.19 the evolution of the plasma current centroid ($r_c - z_c$) during the UVDE together with the initial plasma equilibrium (blue curve) is reported. Figure 6.20 shows the plasma TFV flux evolution in time.

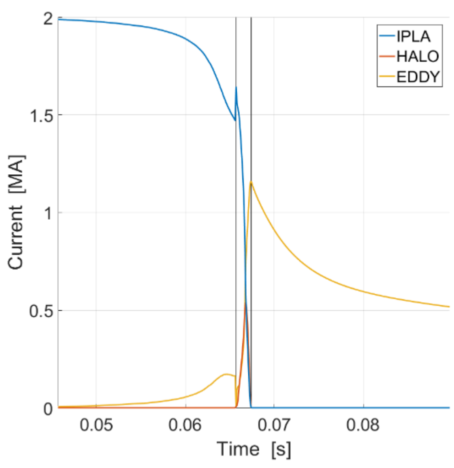

Figure 6.17: MAXFEA plasma current (blue curve), eddy currents (yellow curve) and halo currents (red curve).

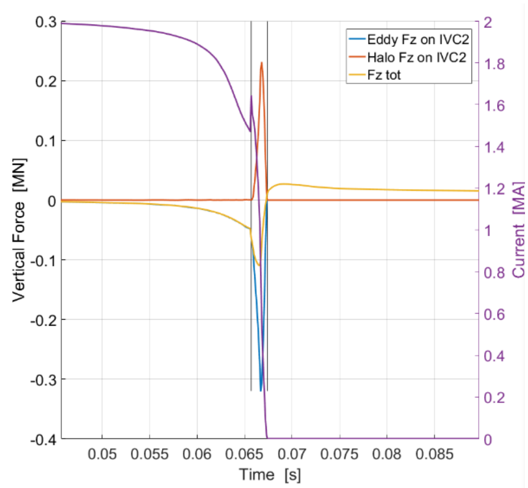

Figure 6.18: MAXFEA Vertical Force on the IVC2 due the eddy currents (blue curve, refers to left ordinate axis), due to the halo currents (red curve, refers to left ordinate axis), due to halo+eddy (yellow curve, refers to left ordinate axis) and Plasma current (purple curve, refers to the right ordinate axis).

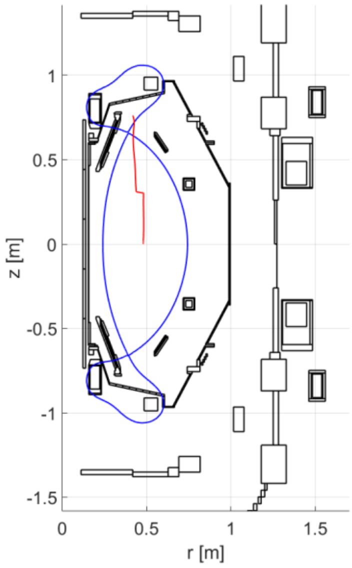

Figure 6.19: Initial plasma equilibrium and plasma centroid (rc-zc) movement during the UVDE fast.

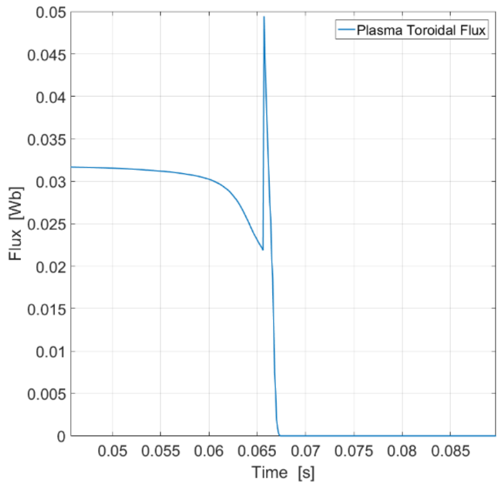

Figure 6.20: Plasma TFV evolution during the UVDE.

6.5.1.3 Full 3D analysis: PFV + TFV + HC

Downstream the MAXFEA simulation, 3D EM analyses have been carried out introducing the plasma evolution in the 3D model with the proposed methodology. Regarding the HC, the assumed in and out locations are shown in Figure 6.21. The HC is injected into the Divertor Case and flows towards the IVC2 through the Divertor support. Once in IVC2, the HC circulates in clock-wise direction from the Divertor to the Stabilizing Plate. Finally, it reconnects through the Stabilizing Plate supports and comes back to the plasma. Figure 6.22a shows the HC distribution in the Divertor and its supports at 0.0668s, when HC is a its maximum. Instead, in Figure 6.22b the HC distribution in IVC2 at the same time instant is presented, whilst Figure 6.22c shows the HC in the Stabilizing Plate and its supports.

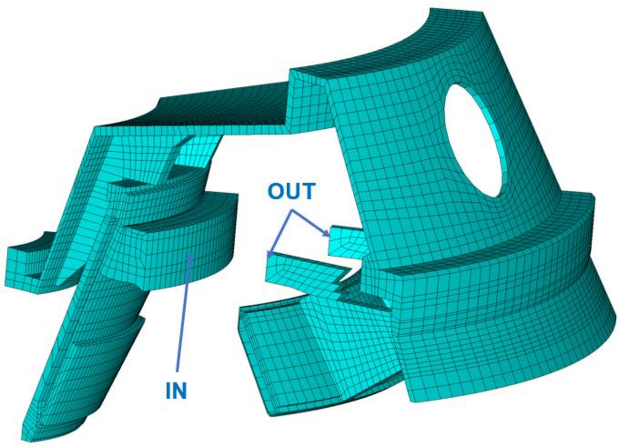

Figure 6.21: HC assumed in and out locations

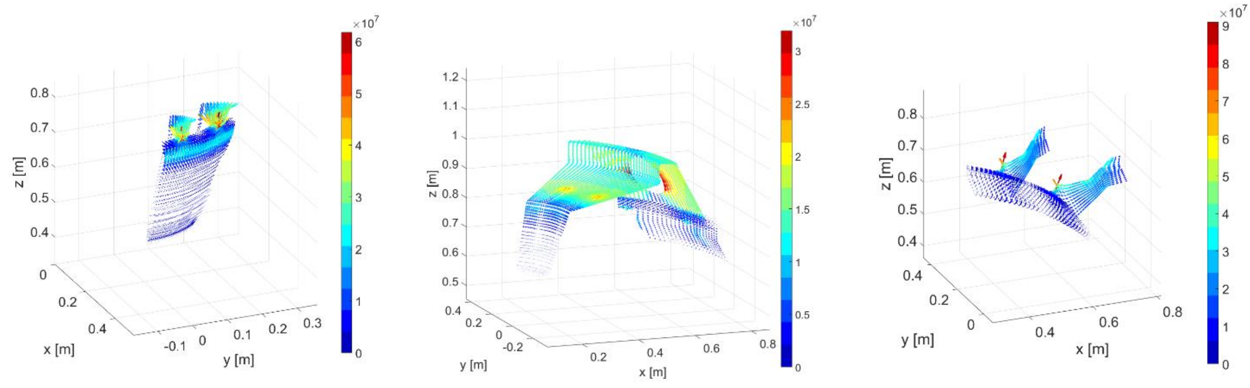

a) b) c)

Figure 6.22: HC distribution [A/m^2] at its peak (0.0668s) a) Divertor and supports b) IVC2 c) Stabilizing Plate and supports

As far as the PFV and TFV analysis are concerned, Figure 6.23 provides an overview of the eddy currents distribution in the IVC2 at the end of the CQ (0.0674s), when they reach a maximum. Instead, Figure 6.24 presents force density distributions on IVC2 at two different time: at the HC peak (Figure 6.24a), at 0.0668s, and at the eddy current peak (Figure 6.24b), at 0.0674s (end of CQ). These force distributions comprehend all the EM contributions (PFV+TFV+HC), including the toroidal field coming from the magnetostatic analysis. From Figure 6.24a, it emerges that in the upper part of the IVC2 (red circled zone) the force density is mainly oriented in vertical direction and it is dominated by the interaction between the HC and the TF, reaching a peak of about 80MN/m^3 in correspondence of the HC concentration in the Divertor supports connections. Another zone of high force density is in the central tube (blue circled zone). Here, instead, the force is mainly directed radially inboard and it is principally due to the interaction between the poloidal current coming from the TFV and the TF. In fact, the latter is intense in this zone since the close vicinity with the magnet central column. Similar but slightly more intense force distribution is found in the central tube at the end of the CQ, when the eddy current is higher. Conversely, the upper part of the IVC2 experiences a lower force concentration since the plasma is terminated and the HC approaches to zero.

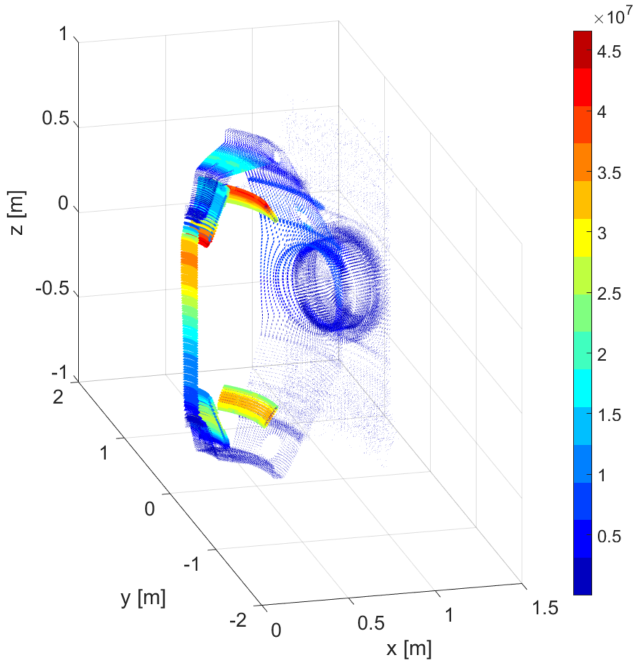

Figure 6.23: Eddy current distribution [A/m^2] at the end of the CQ (0.0674s)

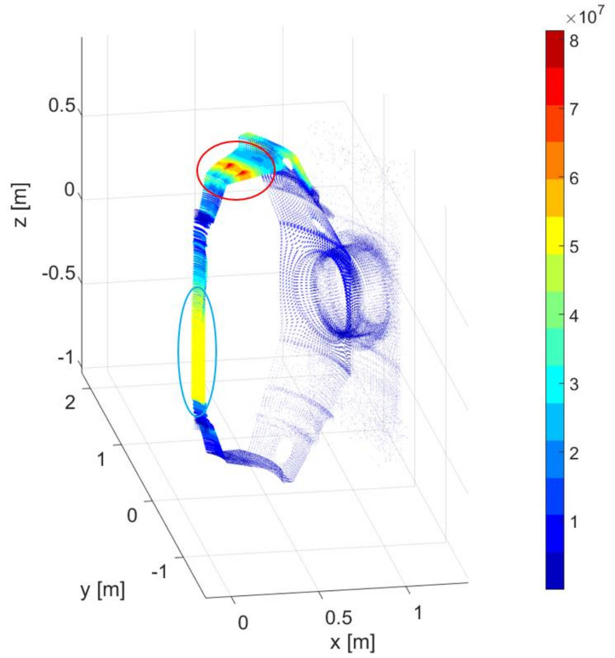

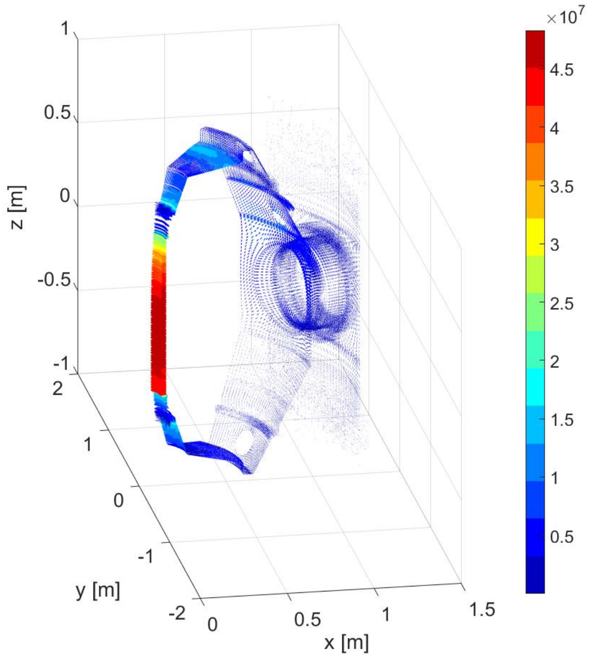

Figure 6.24: Force density distribution [N/m^3] a) HC peak (0.0668s) b) end of CQ (eddy current peak, 0.0674s)

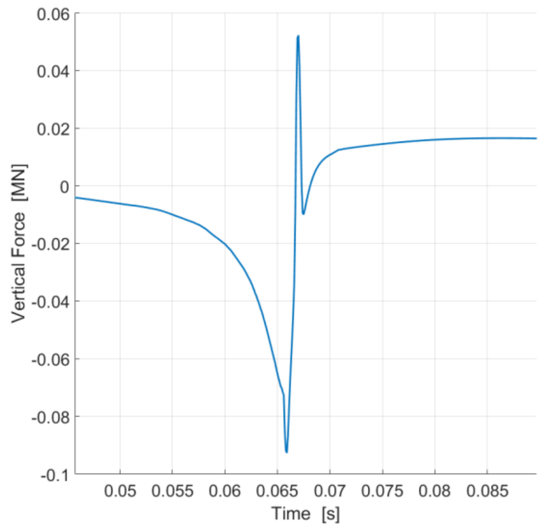

Figure 6.25: Total vertical force acting on IVC2

6.6 Structural analyses

The structural results, in terms of displacements and von Mises stress, are shown in the following sections.

6.6.1 Halo peak (0.0668s)

In this section the results, in terms of displacements and stresses, are illustrated for the UVDE fast at 0.0668ms (halo peak). This time instant corresponds to the maximum value of the halo current induced in the structures. The simulation considers also the gravity load.

First step was the interpolation of the EM loads from the EM to the Structural model. Figure 6.26 shows the interpolated force distribution on the IVC2. In Figure 6.27 the total displacement of the whole model is represented.

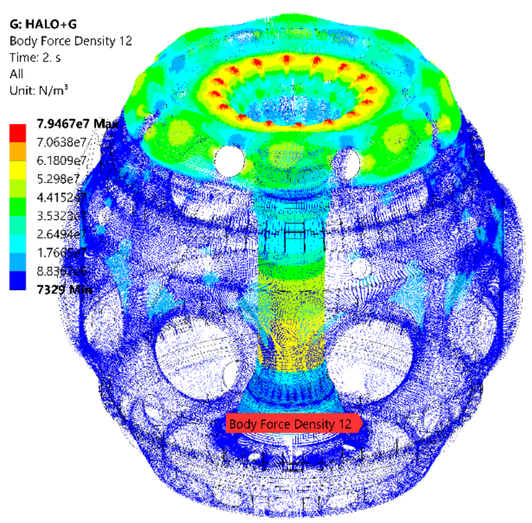

Figure 6.26: UVDE fast @0.0668ms: interpolated force distribution [N/m^3] on IVC2

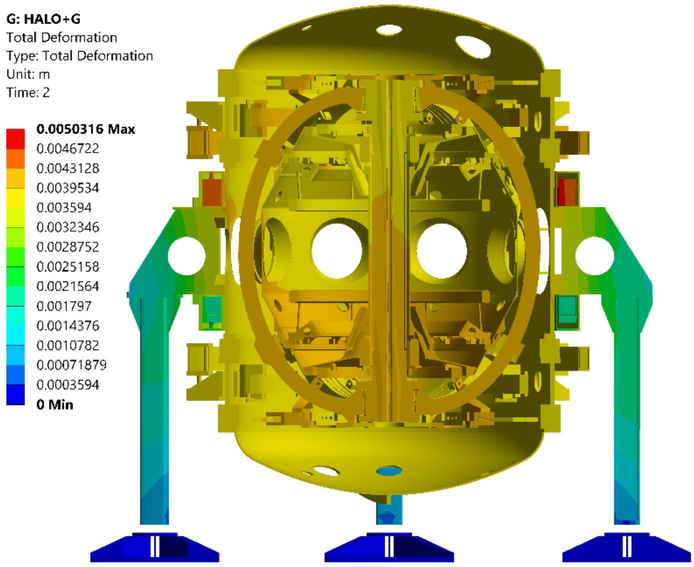

Figure 6.27: UVDE fast @0.0668ms: total displacement

An overview of the von Mises stress contour on the model is given in Figure 6.28. It is possible to observe how the stress level is well below the yielding level of materials (Inconel 718 ~1070MPa, SS ~350MPa), with no critical zones highlighted. In particular, Figure 6.29a shows the stress contour for in IVC2 and all the components mechanically connected with the it, namely the DIV, SX, PSH and MC coils, the Divertors and the Stabilizing Plates, while in Figure 6.29b the stress map in the magnet system is reported.

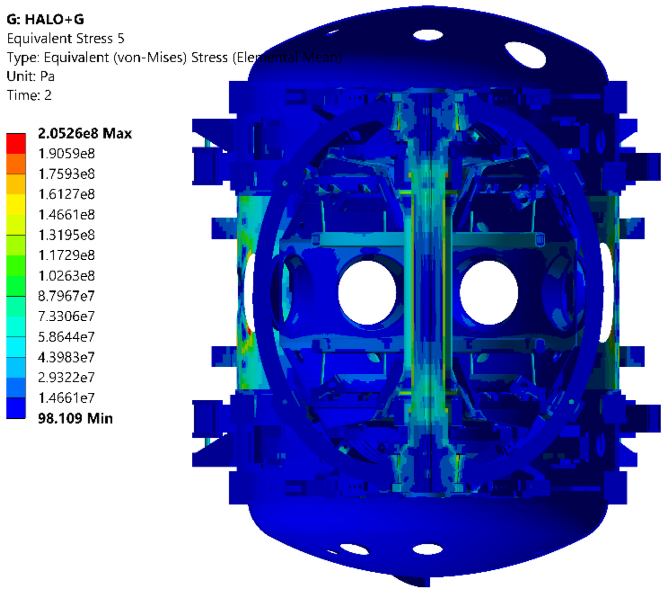

Figure 6.28: UVDE fast @0.0668ms: overview of von Mises stress contour

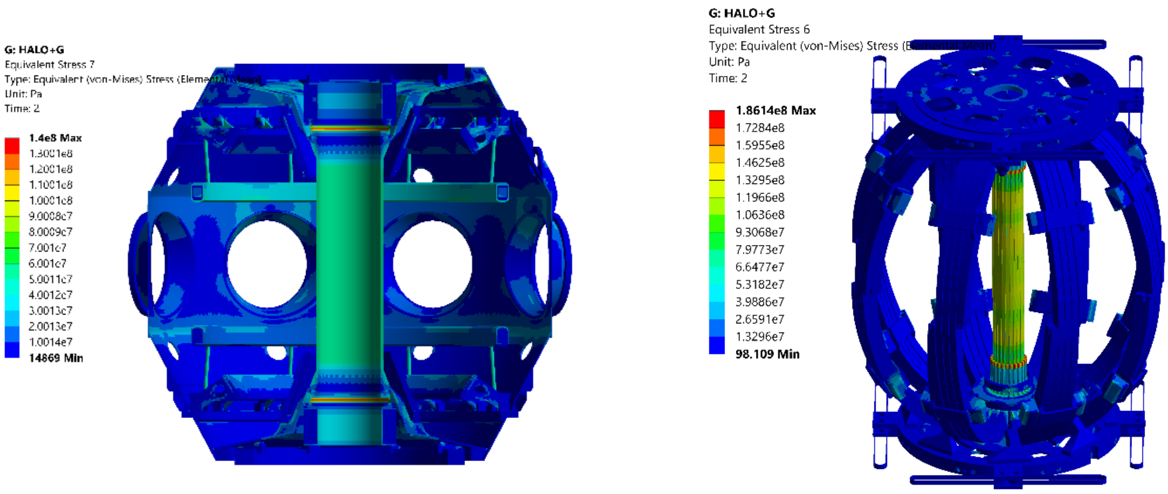

a) b)

Figure 6.29: UVDE fast @0.0668ms: overview of von Mises stress contour a) IVC2 + comps b) TF coils system

6.6.2 Eddy peak (0.0674s)

In this section the results, in terms of displacements and stresses, are illustrated for the UVDE fast at 0.0674ms (eddy peak). This time instant corresponds to the maximum value of the eddy current induced in the structures, occurring at the end of CQ. The simulation considers also the gravity load.

First step was the interpolation of the EM loads from the EM to the Structural model. Figure 6.30 shows the interpolated force distribution on the IVC2. In Figure 6.31 the total displacement of the whole model is represented.

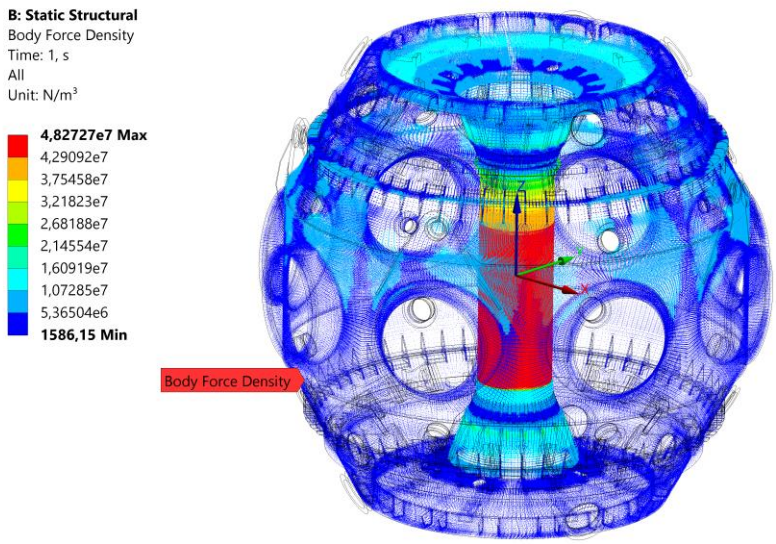

Figure 6.30: UVDE fast @0.0674ms: interpolated force distribution [N/m^3] on IVC2

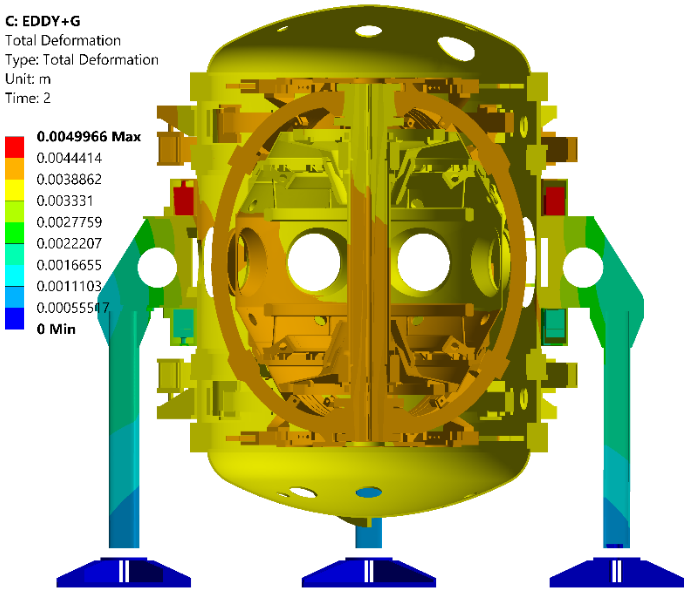

Figure 6.31: UVDE fast @0.0674ms: total displacement

An overview of the von Mises stress contour on the model is given in Figure 6.32. It is possible to observe how the stress level is well below the yielding level of materials (Inconel 718 ~1070MPa, SS ~350MPa), with no critical zones highlighted. In particular, Figure 6.33a shows the stress contour for in IVC2 and all the components mechanically connected with the it, namely the DIV, SX, PSH and MC coils, the Divertors and the Stabilizing Plates, while in Figure 6.33b the stress map in the magnet system is reported.

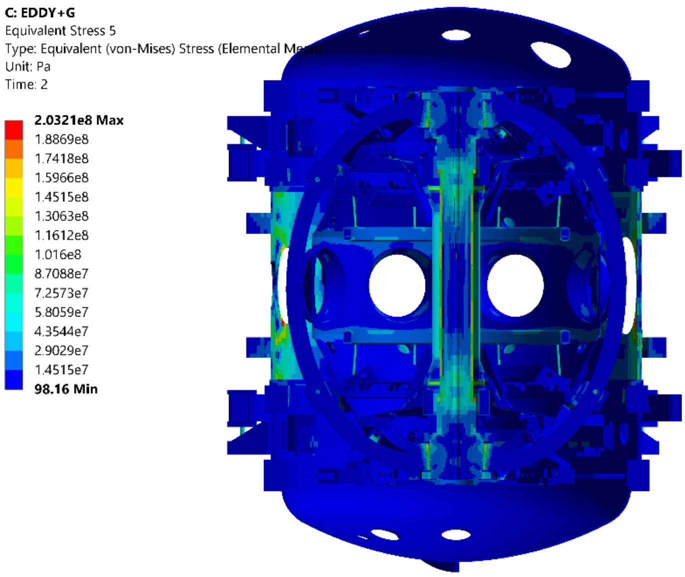

Figure 6.32: UVDE fast @0.0674ms: overview of von Mises stress contour

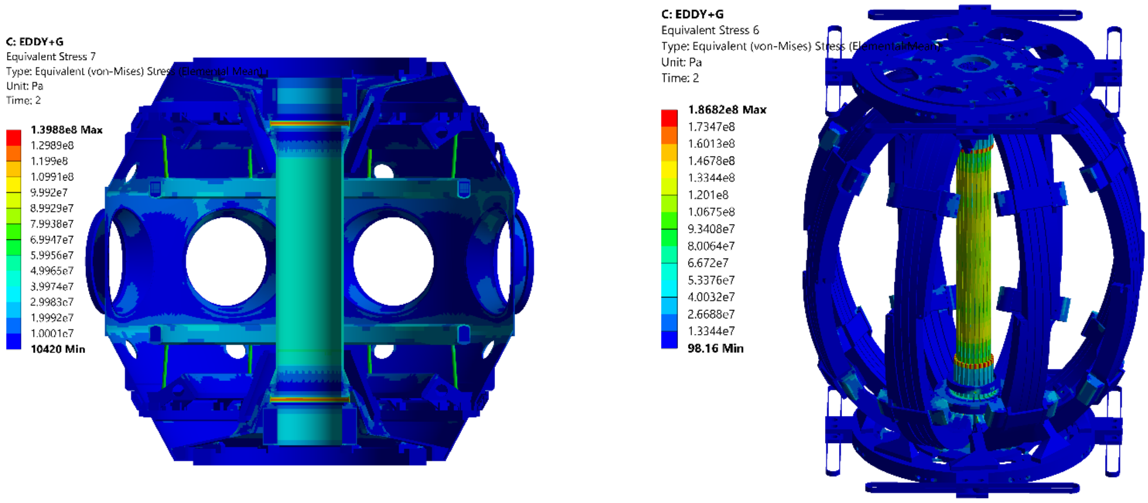

a) b)

Figure 6.33: UVDE fast @0.0674ms: overview of von Mises stress contour a) IVC2 + comps b) TF coils system

6.7 Conclusions

In this Section, the analysis of the EM and structural response of the new ST40 IVC2 during an UVDE fast has been presented. The proposed methodology based on the use of MAXFEA code in combination with ANSYS APDL has been applied, showing that its field of application can be extended to non-conventional low aspect ratio tokamaks like ST40. The results shows that a vertical force peak of around -90kN is reached in IVC2 during the CQ. This force is that experienced by the IVC2 supports and, beyond the one that directly loads the IVC2, it includes the forces acting on all the components mechanically connected with the IVC2, namely the DIV, SX, PSH and MC coils, the Divertors and the Stabilizing Plates. In terms of force density distribution, it has emerged that highest load in the IVC2 occurs at the halo current peak in correspondence of the Divertor support connections as the result of the interaction between HC and TF (~80MN/m^3 mainly directed vertically). Whereas, in the central tube the highest force peak is experienced at the end of CQ (eddy current peak) as the result of the interaction between eddy current coming from TFV and the TF (~50MN/m^3 mainly directed radially inboard).

Concerning the structural analysis, two different time instants have been analysed, namely the eddy peak and the halo peak instants. The stress level is found to be well below the yielding level of materials in both the simulations and no critical zone have been highlighted.

The studies herein presented led to journal publication [79].

7 Conclusions

In this Thesis, a novel multiphysics and multicode approach aimed at evaluation of the Electro-Magnetic (EM) loads experienced by tokamak structures both in normal (e.g. plasma ramp-up/down) and off-normal conditions (e.g. unforeseen plasma perturbations, disruptions, etc) has been developed and successfully applied in the context of DEMO, DTT and ST40 projects. In particular, the EM response of the main components of these devices, such as the Vacuum Vessel (VV) and the In-Vessel Components (IVCs), has been investigated during the so-called plasma disruptions. Based on the use of MAXFEA code, proved to be a reliable tool with the capability to reproduce experimental plasma transients [69], and APDL, that allows to overcome the limitations of 2D simulations, the methodology proposed in this Thesis demonstrated to be a valid engineering tool to support the design of such components both in conceptual (DEMO) and in detailed phase of the design (DTT, ST40), proving at the same time to have a wide range of applications: from present generation experimental devices to DEMO, from conventional to non-conventional aspect ratio tokamaks, from standard to advanced plasma configurations. In fact, regarding the latter, there were always a good agreement between MAXFEA and the various codes used in these different organizations. Moreover, in DTT and ST40 applications it was demonstrated how the outputs of these EM analyses can be subsequently used to carry out detailed mechanical analyses aimed to verify and/or support an optimal design of the components, therefore showing the possibility to study both 3D detailed EM and mechanical responses of the structures by means of different models and physics simulation environments, exploiting the functionality offered by MAXFEA code and ANSYS.

An extensive V&V activity was carried out to validate MAXFEA code and the proposed procedure against experimental data from different tokamaks (JET, ASDEX and ST40) and to verify the results with other analyses. In the context of DEMO, MAXFEA was extensively validated against experimental JET and ASDEX plasma perturbations and disruptions and benchmarked against other predictive analysis on DEMO (this study is reported in detail in [69]). A similar work was also in the context of ST40, as detailed presented in Section 6.2.

The proposed methodology was detailed exposed in Section 3. As discussed, the main sources of EM loads during disruptions, namely the plasma PFV, TFV and HC, are previously computed by means of MAXFEA code and then introduced in ANSYS 3D models in an equivalent way with certain techniques. In particular, PFV is simulated by means of a set of filaments, while TFV is reproduced via a thin torus onto which an equivalent poloidal current is applied. Instead, starting from the information of the global halo current expected during the evolution and assuming possible in and out locations according to MAXFEA simulations, the actual 3D HC distributions are evaluated injecting the HC through the considered locations in dedicated 3D ANSYS models. All the EM contributions are then combined in the post-processing phase with a linear superposition. In particular, since the models for the different analysis can be developed in a such way that they feature the same mesh, the various EM contributions can be easily added element by element, facilitating the post-processing operations. One of the main advantages of the proposed approach is that the analyses are completely modular: each EM contribution on each component can be isolated and deeply analysed if needed. This circumstance permits to divide non-trivial evolutions of the currents, fields and forces in more elementary sub-contributions, facilitating a deeper understanding of the phenomenon. Clearly, this modularity is possible until ferromagnetic materials are not present in the models, that is the case of all the applications reported in this Thesis. In fact, DTT and ST40 do not present ferromagnetic components and, as presented in Section 4, a simplified DEMO model has been considered for the development of the proposed procedure, neglecting the presence of ferromagnetic IVCs. This possibility allows to run separate analysis for each EM contribution, exploiting the Magnetic Vector Potential (MVP) formulation provided by ANSYS [64]. Nevertheless, this procedure can be extended also to the case in which ferromagnetic non-linearities have to be considered, in much similar fashion to what presented in [65], being careful to use the appropriate problem formulation in ANSYS, namely the Edge-Based formulation.

In Section 2, an overview of the disruptions phenomenology was provided, in particular focusing on their EM implications, especially under the modelling point of view.

The application of this procedure to DEMO was presented in Section 4. Indeed, DEMO was the testbed for the development of this methodology. In particular, DEMO PMI SN magnetic configuration was reproduced considering a simplified geometry (i.e. VV and ports, ferromagnetic IVCs such as the BBs and the Divertors are not included in the model) and a fast UVDE was chosen as disruption scenario. Once validated, its reliability has been recognized in EUROfusion and the proposed procedure has been included as part of the DEMO FW protection integrated design strategy [72], to be used in future more detailed studies in this context (e.g. increasing the complexity of the models by including IVCs and considering ferromagnetic non-linearities). These DEMO studies have led to the following journal publications [69], [72] and [73].

Once applicated in DEMO, the proposed methodology was also successfully applied in much more detailed analyses in the context of DTT and ST40 projects, as presented in Section 5 and Section 6, respectively. Concerning DTT, within the final design stage of the DTT VVP, a study to analyse the mechanical and EM behaviour of this component during plasma VDEs has been carried out through the use of this methodology. From this study, it has emerged that the VVP mechanical response is acceptable in all of the scenarios but, during a particular event, namely the DVDE slow scenario, a stress concentration in correspondence of the connection of the pedestal with the VV outer shell has emerged. As a consequence, mechanical reinforcement in this region has been introduced in order to obtain an optimal design of the VVP. In this Thesis, the EM and mechanical response of the DTT VVP during this DVDE slow event is presented, with the aim to show the successful application of this novel procedure in the context of the DTT project and its reliability and capability to support the final stage design of these kind of components. These DTT studies are presented in the journal publications [75] [76].

Similarly, within the final design stage of the new ST40 IVC2, the necessity to analyse in detail the EM behaviour of this component under the loads coming from plasma disruptions has recently emerged in order to verify the design or drive further modifications. In this context, a study to analyse the EM response of IVC2 during a plasma disruption has been carried out by means of this MAXFEA-ANSYS approach. In particular, an upward VDE fast disruption scenario has been considered. Downstream the EM analysis, the mechanical behaviour of ST40 has been also studied developing a global structural model of the system. The results showed the successful use of the proposed methodology even in this context, proving that its field of application can be extended also to such advanced non-conventional aspect ratio tokamaks. This study is the subject of the journal publication recently submitted to *Fusion Engineering and Design* and currently in the final stage of the review process [79].

8 Bibliography

[1] "IAEA, 'Energy, Electricity and Nuclear Power Estimates for the period up to 2050', 2019 Edition, ISBN 978-92-0-109319-6 (2019)."

[2] "ITER, Advantages of fusion. https://www.iter.org/sci/Fusion (accessed December 14, 2021)."

[3] J. Wesson and D. J. Campbell, *Tokamaks*, Fourth. Oxford university press, 2011.

[4] "https://www.euro-fusion.org/."

[5] F. Romanelli, *Fusion Electricity - A roadmap to the realisation of fusion energy*. 2012.

[6] T. Donné, *European Research Roadmap to the Realisation of Fusion Energy*. 2018.

[7] G. Federici *et al.*, "Overview of the design approach and prioritization of R&D activities towards an EU DEMO," *Fusion Eng. Des.*, vol. 109–111, no. 2016, pp. 1464–1474, 2016, doi: 10.1016/j.fusengdes.2015.11.050.

[8] G. Federici *et al.*, "Overview of the DEMO staged design approach in Europe," *Nucl. Fusion*, vol. 59, no. 6, 2019, doi: 10.1088/1741-4326/ab1178.

[9] H. Zohm *et al.*, "On the physics guidelines for a tokamak DEMO," *Nucl. Fusion*, vol. 53, no. 7, 2013, doi: 10.1088/0029-5515/53/7/073019.

[10] O. Motojima, "The ITER project construction status," 2015, doi: 10.1088/0029-5515/55/10/104023.

[11] A. Pizzuto, *Divertor Tokamak Test facility Project Proposal*. 2015.

[12] R. Albanese, F. Crisanti, P. Martin, R. Martone, and A. Pizzuto, *DTT - Divertor Tokamak Test Facility – Interim Design Report*. ENEA, 2019.

[13] G. Mazzitelli *et al.*, "Role of Italian DTT in the power exhaust implementation strategy," *Fusion Eng. Des.*, vol. 146, no. October 2018, pp. 932–936, 2019, doi: 10.1016/j.fusengdes.2019.01.117.

[14] R. Albanese, "DTT: a divertor tokamak test facility for the study of the power exhaust issues in view of DEMO," *Nucl. Fusion*, vol. 57, no. 1, p. 016010, Jan. 2017, doi: 10.1088/0029-5515/57/1/016010.

[15] R. Albanese *et al.*, "Design review for the Italian Divertor Tokamak Test facility," *Fusion Eng. Des.*, vol. 146, no. October 2018, pp. 194–197, Sep. 2019, doi: 10.1016/j.fusengdes.2018.12.016.

[16] R. Ambrosino, "DTT - Divertor Tokamak Test facility: A testbed for DEMO," *Fusion Eng. Des.*, vol. 167, no. February, 2021, doi: 10.1016/j.fusengdes.2021.112330.

[17] "https://www.dtt-project.it/."

[18] FIA, "The global fusion industry in 2021," 2021.

[19] A. Sykes *et al.*, "Compact fusion energy based on the spherical tokamak," *Nucl. Fusion*, vol. 58, no. 1, 2018, doi: 10.1088/1741-4326/aa8c8d.

[20] “McNamara, Steven, and Tokamak Energy Team. ‘Tokamak Energy and the high-field spherical tokamak route to fusion power.’ APS Division of Plasma Physics Meeting Abstracts. Vol. 2019. 2019.”

[21] “https://www.tokamakenergy.co.uk/ (accessed Feb 17, 2022).”

[22] M. Ono and R. Kaita, “Recent progress on spherical torus research,” *Phys. Plasmas*, vol. 22, no. 4, 2015, doi: 10.1063/1.4915073.

[23] Y. K. M. Peng and D. J. Strickler, “Features of spherical torus plasmas,” *Nucl. Fusion*, vol. 26, no. 6, pp. 769–777, 1986, doi: 10.1088/0029-5515/26/6/005.

[24] A. Sykes, “Spherical tokamak programme at Culham,” *Nucl. Fusion*, vol. 39, no. Special Issue, pp. 1271–1281, 1999, doi: 10.1088/0029-5515/39/9y/305.

[25] M. Gryaznevich and O. Asunta, “Overview and status of construction of ST40,” *Fusion Eng. Des.*, vol. 123, pp. 177–180, 2017, doi: 10.1016/j.fusengdes.2017.03.011.

[26] M. Gryaznevich, “Faster fusion: ST40, engineering, commissioning, first results,” *AIP Conf. Proc.*, vol. 2179, no. November, 2019, doi: 10.1063/1.5135481.

[27] H. R. Koslowski *et al.*, “Disruptions in ITER and strategies for their control and mitigation,” *J. Nucl. Mater.*, vol. 463, pp. 39–48, 2015, doi: 10.1016/j.jnucmat.2014.10.075.

[28] S. Entler, J. Horacek, T. Dlouhy, and V. Dostal, “Approximation of the economy of fusion energy,” *Energy*, vol. 152, pp. 489–497, 2018, doi: 10.1016/j.energy.2018.03.130.

[29] “ITER Physics Basis,” *Nucl. Fusion*, 1999.

[30] T. . Hender *et al.*, “Chapter 3: MHD stability, operational limits and disruptions,” *Nucl. Fusion*, vol. 47, no. 6, pp. S128–S202, Jun. 2007, doi: 10.1088/0029-5515/47/6/S03.

[31] F. C. Schuller, “Disruptions in tokamaks,” *Plasma Phys. Control. Fusion*, vol. 37, no. 11A, 1995, doi: 10.1088/0741-3335/37/11A/009.

[32] M. Sugihara *et al.*, “Disruption scenarios, their mitigation and operation window in ITER,” *Nucl. Fusion*, vol. 47, no. 4, pp. 337–352, 2007, doi: 10.1088/0029-5515/47/4/012.

[33] A. . Boozer, “Theory of tokamak disruptions,” *Phys. Plasmas*, vol. 19, no. 5, 2012, doi: 10.1063/1.3703327.

[34] “https://www.iter.org/org/team/fst/itpa/mhd.”

[35] N. W. Eidietis *et al.*, “The ITPA disruption database,” *Nucl. Fusion*, vol. 55, no. 6, p. 63030, 2015, doi: 10.1088/0029-5515/55/6/063030.

[36] D. Bora, “SST and ADITYA tokamak research in India,” *Brazilian J. Phys.*, vol. 32, no. 1, pp. 193–216, Mar. 2002, doi: 10.1590/S0103-97332002000100032.

[37] I. H. Hutchinson *et al.*, “First results from Alcator-C-MOD*,” *Phys. Plasmas*, vol. 1, no. 5, pp. 1511–

1518, May 1994, doi: 10.1063/1.870701.

[38] U. Stroth *et al.*, “Overview of ASDEX Upgrade results,” *Nucl. Fusion*, vol. 53, no. 10, p. 104003, Oct. 2013, doi: 10.1088/0029-5515/53/10/104003.

[39] J. L. Luxon, “A design retrospective of the DIII-D tokamak,” *Nucl. Fusion*, vol. 42, no. 5, pp. 614–633, 2002, doi: 10.1088/0029-5515/42/5/313.

[40] F. Romanelli, “Overview of the JET results with the ITER-like wall,” *Nucl. Fusion*, vol. 53, no. 10, p. 104002, Oct. 2013, doi: 10.1088/0029-5515/53/10/104002.

[41] A. Isayama, “Overview of JT-60U results towards the resolution of key physics and engineering issues in ITER and JT-60SA,” *Nucl. Fusion*, vol. 51, no. 9, p. 094010, Sep. 2011, doi: 10.1088/0029-5515/51/9/094010.

[42] S. Coda for the TCV Team, “Overview of recent and current research on the TCV tokamak,” *Nucl. Fusion*, vol. 53, no. 10, p. 104011, Oct. 2013, doi: 10.1088/0029-5515/53/10/104011.

[43] H. Meyer *et al.*, “Overview of physics results from MAST towards ITER/DEMO and the MAST Upgrade,” *Nucl. Fusion*, vol. 53, no. 10, p. 104008, Oct. 2013, doi: 10.1088/0029-5515/53/10/104008.

[44] M. Ono, M. G. Bell, R. E. Bell, T. Bigelow, M. Bitter, and W. Blanchard, “Overview of the initial NSTX experimental results,” *Nucl. Fusion*, vol. 41, 2001.

[45] D. A. Humphreys and A. G. Kellman, “Analytic modeling of axisymmetric disruption halo currents,” *Phys. Plasmas*, vol. 6, no. 7, pp. 2742–2756, Jul. 1999, doi: 10.1063/1.873231.

[46] V. Riccardo *et al.*, “Analysis of JET halo currents,” *Plasma Phys. Control. Fusion*, vol. 46, no. 6, pp. 925–934, Jun. 2004, doi: 10.1088/0741-3335/46/6/001.

[47] S. P. Gerhardt, J. Menard, S. Sabbagh, and F. Scotti, “Characterization of disruption halo currents in the National Spherical Torus,” *Nucl. Fusion*, 2012, doi: 10.1088/0029-5515/52/6/063005.

[48] Y. Neyatani, R. Yoshino, Y. Nakamura, and S. Sakurai, “Characteristics of halo currents in JT-60U,” *Nucl. Fusion*, 1999.

[49] V. Riccardo, A. Loarte, and the JET EFDA Contributors, “Timescale and magnitude of plasma thermal energy loss before and during disruptions in JET,” *Nucl. Fusion*, vol. 45, no. 11, pp. 1427–1438, Nov. 2005, doi: 10.1088/0029-5515/45/11/025.

[50] J. . C. Wesley *et al.*, “Disruption Characterization and Database Activities for ITER,” 2006.

[51] G. Ramogida *et al.*, “First disruption studies and simulations in view of the development of the DEMO Physics Basis,” *Fusion Eng. Des.*, vol. 96–97, pp. 348–352, 2015, doi: 10.1016/j.fusengdes.2015.06.172.

[52] R. Albanese and F. Villone, “The linearized CREATE-L plasma response model for the control of current, position and shape in tokamaks,” *Nucl. Fusion*, vol. 38, no. 5, pp. 723–738, 1998, doi:

10.1088/0029-5515/38/5/307.

[53] G. Ambrosino and R. Albanese, "Magnetic Control of Plasma Current, Position, and Shape in Tokamaks: A survey of modeling and control approaches," *IEEE Control Syst.*, vol. 25, no. 5, pp. 76–92, 2005, doi: 10.1109/MCS.2005.1512797.

[54] E. Rebhan, "Stability Boundaries of Tokamaks with Respect to Rigid Displacements," *Nucl. Fusion*, vol. 15, no. 2, pp. 277–285, 1975, doi: 10.1088/0029-5515/15/2/012.

[55] D. J. Ward and S. C. Jardin, "Effects of plasma deformability on the feedback stabilization of axisymmetric modes in tokamak plasmas," *Nucl. Fusion*, vol. 32, no. 6, pp. 973–994, 1992, doi: 10.1088/0029-5515/32/6/I07.

[56] I. Senda, T. Shoji, T. Tsunematsu, T. Nishino, and H. Fujieda, "Approximation of eddy currents in three dimensional structures by toroidally symmetric models, and plasma control issues," *Nucl. Fusion*, vol. 37, no. 8, pp. 1129–1145, 1997, doi: 10.1088/0029-5515/37/8/I08.

[57] R. Albanese, R. Fresa, G. Rubinacci, and F. Villone, "Time evolution of tokamak plasmas in the presence of 3D conducting structures," *IEEE Trans. Magn.*, vol. 36, no. 4 I, pp. 1804–1807, 2000, doi: 10.1109/20.877795.

[58] J. L. Luxon and B. B. Brown, "Magnetic analysis of non-circular cross section tokamaks," *Nucl. Fusion*, vol. 813, 1982.

[59] F. Villone, L. Barbato, S. Mastrostefano, and S. Ventre, "Coupling of nonlinear axisymmetric plasma evolution with three-dimensional volumetric conductors," *Plasma Phys. Control. Fusion*, 2013, doi: 10.1088/0741-3335/55/9/095008.

[60] S. Miyamoto *et al.*, "Inter-code comparison benchmark between DINA and TSC for ITER disruption modelling," *Nucl. Fusion*, vol. 54, no. 8, 2014, doi: 10.1088/0029-5515/54/8/083002.

[61] "P. Barabaschi, The MAXFEA code, Proc. Plasma Control, Technical Meeting (Naka, Japan, April 1993)."

[62] A. Beghi, M. Cavinato, and A. Cenedese, "Nonlinear dynamic modeling for control of fusion devices," in *2008 47th IEEE Conference on Decision and Control*, 2008, pp. 3133–3138, doi: 10.1109/CDC.2008.4739229.

[63] M. Roccella, A. Marin, F. Lucca, and M. Merola, "Detailed electromagnetic numerical evaluation of eddy currents induced by toroidal and poloidal magnetic field variation and halo currents," *Fusion Eng. Des.*, vol. 83, no. 10–12, pp. 1625–1630, 2008, doi: 10.1016/j.fusengdes.2008.07.013.

[64] ANSYS Inc., "ANSYS Low-Frequency Electromagnetic Analysis Guide." .

[65] I. A. Maione *et al.*, "Electromagnetic analysis activities in support of the Breeding Blanket during the DEMO Pre-Conceptual Design Phase: Methodology and main results," *Fusion Eng. Des.*, vol. 166, no.

February, 2021, doi: 10.1016/j.fusengdes.2021.112285.

[66] C. Bachmann *et al.*, "Key design integration issues addressed in the EU DEMO pre-concept design phase," *Fusion Eng. Des.*, vol. 156, no. September 2019, p. 111595, Jul. 2020, doi: 10.1016/j.fusengdes.2020.111595.

[67] F. Maviglia *et al.*, "Wall protection strategies for DEMO plasma transients," *Fusion Eng. Des.*, vol. 136, no. February, pp. 410–414, 2018, doi: 10.1016/j.fusengdes.2018.02.064.

[68] F. Maviglia *et al.*, "Impact of plasma thermal transients on the design of the EU DEMO first wall protection," *Fusion Eng. Des.*, vol. 158, no. April, p. 111713, Sep. 2020, doi: 10.1016/j.fusengdes.2020.111713.

[69] G. Sias *et al.*, "Inter-machine plasma perturbation studies in EU-DEMO relevant scenarios: lessons learnt for EM forces prediction during VDEs," *Nucl. Fusion*, Feb. 2022, doi: 10.1088/1741-4326/ac53c1.

[70] R. Albanese and G. Rubinacci, "Integral formulation for 3D eddy-current computation using edge elements," *IEE Proc. A Phys. Sci. Meas. Instrumentation, Manag. Educ. Rev.*, vol. 135, no. 7, p. 457, 1988, doi: 10.1049/ip-a-1.1988.0072.

[71] "https://www.ansys.com/."

[72] F. Maviglia *et al.*, "Integrated design strategy for EU-DEMO first wall protection from plasma transients," *Fusion Eng. Des.*, vol. 177, no. February, p. 113067, Apr. 2022, doi: 10.1016/j.fusengdes.2022.113067.

[73] R. Lombroni, F. Giorgetti, G. Calabrò, P. Fanelli, and G. Ramogida, "Using MAXFEA code in combination with ANSYS APDL for the simulation of plasma disruption events on EU DEMO," *Fusion Eng. Des.*, no. March, p. 112697, 2021, doi: 10.1016/j.fusengdes.2021.112697.

[74] R. Albanese, R. Ambrosino, and M. Mattei, "CREATE-NL+: A robust control-oriented free boundary dynamic plasma equilibrium solver," *Fusion Eng. Des.*, vol. 96–97, pp. 664–667, Oct. 2015, doi: 10.1016/j.fusengdes.2015.06.162.

[75] E. Martelli *et al.*, "Design status of the Vacuum Vessel of DTT facility," *Fusion Eng. Des.*, vol. 172, no. November 2020, p. 112760, Nov. 2021, doi: 10.1016/j.fusengdes.2021.112760.

[76] F. Giorgetti, "Vertical Displacement Events analysis using MAXFEA code in combination with ANSYS APDL in the final design stage of the DTT Vacuum Vessel," *Fusion Eng. Des.*

[77] G. W. Ma *et al.*, "In-vessel Components , SDC-IC," 2012.

[78] McNamara, Steven, et al. 'Overview of recent results from the ST40 high-field spherical tokamak.' Bulletin of the American Physical Society 66 (2021).

[79] R. Lombroni, "Use of MAXFEA code in combination with ANSYS APDL to study the Electro-

Magnetic behaviour of the new ST40 Inner Vacuum Chamber (IVC2) proposal during a plasma VDE,” *Fusion Eng. Des.*

[80] Romanelli, Michele, et al. ‘Integrated Modelling of Plasmas in the ST40 High-Field Spherical Tokamak.’ Bulletin of the American Physical Society 66 (2021).

[81] P. Buxton, et al., Merging Compression start-up in ST40, P1. 047, 29thSymposium on Fusion Technology (SOFT 2016) (2016).

[82] A. Sykes *et al.*, “First results from the START experiment,” *Nucl. Fusion*, vol. 32, no. 4, pp. 694–699, 1992, doi: 10.1088/0029-5515/32/4/I16.

[83] A. Sykes *et al.*, “First results from MAST,” *Nucl. Fusion*, vol. 41, no. 10, pp. 1423–1433, 2001, doi: 10.1088/0029-5515/41/10/310.

[84] P. F. Buxton *et al.*, “On the design and role of passive stabilisation within the ST40 spherical tokamak,” *Plasma Phys. Control. Fusion*, vol. 60, no. 6, 2018, doi: 10.1088/1361-6587/aabd01.